Czech Technical University in Prague
Faculty of Nuclear Sciences and Physical Engineering

Doctoral Thesis

2010 Zdeněk Hubáček

Czech Technical University in Prague
Faculty of Nuclear Sciences and Physical Engineering

Measurement of the Three-jet Mass Cross Section in $p\bar{p}$ Collisions at $\sqrt{s} = 1.96$ TeV

Zdeněk Hubáček

Department of Physics
Academical Year: 2009/2010
Advisor: Prof. RNDr. Vladislav Šimák, DrSc.

Sometimes,
it is not about the destination,
but about the journey.

Abstract

This thesis describes the measurement of the inclusive three-jet cross section in proton-antiproton collisions at $\sqrt{s} = 1.96\,\mathrm{TeV}$ measured at the DØ experiment at the Fermilab Tevatron Collider in the Fermi National Accelerator Laboratory, Batavia, Illinois, USA. The cross section as a function of three-jet invariant mass is provided in three regions of the third jet transverse momentum and three regions of jet rapidities. It utilizes a data sample collected in the so called Run IIa data taking period (2002–2006) corresponding to the integrated luminosity of about $0.7\,\mathrm{fb}^{-1}$. The results are used to test the next-to-leading order predictions of Quantum chromodynamics computed using the latest parton distribution functions.
Keywords
Quantum chromodynamics, jets, jet algorithms

Abstrakt

Tato dizertace popisuje měření účinného průřezu produkce tří jetů na experimentu DØ ve Fermiho Národní Laboratoři v Batavii, Illinois, USA. Účinný průřez je změřen jako funkce invariantní hmoty tříjetového systému ve třech intervalech rapidity a třech intervalech příčné hybnosti třetího jetu. Celková statistika dat nabraných v letech 2002–2006 odpovídá $0.7\,\mathrm{fb}^{-1}$. Výsledek je porovnán s výpočtem kvantové chromodynamiky v řádu NLO s použitím nejnovějších distribučních funkcí.
Klíčová slova
Kvantová chromodynamika, jety, jetové algoritmy

Declaration

This thesis is the result of my own work, except where explicit reference is made to the work of others and has not been submitted for another qualification to this or any other university.

Acknowledgment

This work would be impossible without the help and support from many people. I would like to start with my advisor, Prof. Vladislav Šimák. Without him, I would never come to Fermilab to work on such an interesting topic as high energy physics is. If not for anything else, I appreciate that the word "impossible" is not a word in his vocabulary.

I have spent three years during my PhD studies directly in Fermilab working with many people of the DØ collaboration. I would like to thank especially the following ones – Bernard Andrieu and Amnon Harel were the first who gave me a serious work within the JetID group which helped me to learn the basics of DØ and *cafe* software frameworks. Then Aurelio Juste and Christophe Royon chose me to participate in a two year effort to perfectly calibrate the jet energy scale (thanks to the rest of the group too: Mikko Voutilainen, Jeroen Hegeman and others). Finally, thanks to all the QCD group conveners (especially Dmitry Bandurin, Duncan Brown, Sabine Lammers, Don Lincoln and Markus Wobisch) and the rest of our small QCD jet subgroup (Kayle DeVaughan, Gennady Obrant and Mandy Rominsky) for helping me to finish the three-jet measurement. The life in Fermilab has been much more fun with friends, especially the Czech and Slovak groups (Kamil Augsten, Vlastislav Hynek, Miroslav Kopál, Jiří Kvita, Alexander Kupčo, Miloš Lokajíček, Roman Lysák, Roman Otec, Karel Soustružník, Marián Zvada and others). And of course, my friends in Prague who tolerate my constant traveling.

I am grateful to Jiří Hejbal, Jiří Kvita and Alexander Kupčo for the tedious task of proofreading this thesis at various stages. Of course, any remaining errors are my own.

Finally, I want to thank my parents for their support during my whole life.

A big thanks to all of you!

Děkuji,

Zdeněk Hubáček

Contents

List of Figures

List of Tables

1 Introduction

Particle physics tries to improve our understanding of the nature by studying the basic properties of matter. What is the matter in the first place, what does it consist of, how was it created, and what are the laws of physics that describe it are the fundamental questions particle physics is trying to answer.

Our knowledge about the matter has significantly improved from ancient theories of basic elements (water, fire, earth, wind) to the discovery of atoms (John Dalton[1]). These atoms were later found to be complicated systems of electrons and nucleons[2]. We managed to explore the structure of individual nucleons discovering quarks and gluons[3]. Every such discovery can be marked by a scale characterizing the size of the observed object. From the scale of water drops (of a size $\sim 10^{-3}$ m) we get to characteristic lengths currently studied $\sim 10^{-18}$ m. This is still far away from fundamental scales we can find in current physical theories (string theories, Planck scale $\sim 10^{-35}$ m). As the length scale decreases, a simple law of quantum physics requires the increase of energy so the observer is able to explore it. The progress is consequently marked with the increasing scale in manpower and (of course) money needed. Current accelerators and detectors, where this fundamental research is done, cost significant amounts of money and require hundreds of physicists and engineers to collaborate. New results are produced virtually every day. Yesterday discoveries serve today for calibrations and will be backgrounds in tomorrow's searches.

1.1 Motivation for the Three-jet Cross Section Measurement

Current knowledge of the particle physics is well described by the so called Standard Model (SM). It describes the theory of electromagnetic, weak and strong interactions among all known particles. While the success of this theory is remarkable, we already know that it is not complete and new theories improving it are being developed. This thesis is devoted to the study

of one part of the Standard Model, namely the theory of strong interaction, Quantum chromodynamics (QCD). QCD was born already more than 30 years ago, it describes the strong interaction among basic matter constituents (quarks) in terms of exchanging strong force carriers (gluons). It also attempts to describe why individual quarks and gluons cannot be observed (the so called confinement) and predicts that in high energy collisions only streams or sprays of highly collimated hadrons (bound states of quarks) will be observed as a result of quark and gluon high energy scattering. These sprays are called (hadronic) jets.

A significant fraction of inelastic collisions contains jets. Inclusive jet cross section $p\bar{p} \rightarrow \text{jet} + X$ measures the probability of producing a jet of some transverse momentum in some rapidity region of the detector. It is the most widely compared quantity between various center of mass energies (SPS@630 GeV $\rightarrow$ Tevatron@1.8 TeV $\rightarrow$ Tevatron@1.96 TeV), experiments (CDF vs DØ at the Fermilab Tevatron Collider) and different jet algorithms within an experiment (k_T vs cone). The theoretical prediction is available at the next-to-leading order and the measurement can serve to constrain parton (quark or gluon) distribution functions (PDFs), especially of gluons at high x (fraction of the proton longitudinal momentum carried by a parton) for which the current experimental conditions provide better constraints over previous hadron-hadron and lepton-hadron experiments (see Fig. 1.1).

The latest result from the DØ experiment[4] is shown in Fig. 1.2 in six bins of jet rapidity y ($y = 0.5 \ln \left[(E + p_z) / (E - p_z) \right]$, where E is the jet energy, p_z is the jet momentum along the beam axis) with jet transverse momentum reaching up to 600 GeV.

In the perturbative picture, in the lowest QCD order, two jets are expected in the collision (if they are within the geometrical acceptance of the detector). Therefore, dijet invariant mass cross section ($\frac{\mathrm{d}\sigma}{\mathrm{d}M_{\mathrm{jj}}}(p\bar{p} \rightarrow 2\,\text{jets} + X)$)[5] is another test of QCD predictions. With good dijet mass resolution, it can be used for new particle searches (like new interaction bosons ($p\bar{p} \rightarrow Z' \rightarrow 2\,\text{jets}$). Dijet angular distribution ($\frac{\mathrm{d}\sigma}{\mathrm{d}\chi}$, $\chi = \frac{1+\cos\theta^*}{1-\cos\theta^*}$ with θ^* being the angle between the dijet system and the beam)[6] can also be used to distinguish between QCD (which has almost Rutherford-like angular distribution) and new physics models. The difference between azimuthal angles ($\Delta\phi$)[7] of the two jets in a dijet system (expected to peak at $\Delta\phi \sim \pi$ for back-to-back dijets at LO) can serve for testing NLO predictions without actually measuring additional jets. It can also serve for tuning parton shower Monte Carlo generators.

Three-jet final state is the next interesting step in the line. Using the same picture, from the leading order dijet, additional hard jet (gluon) is ra-

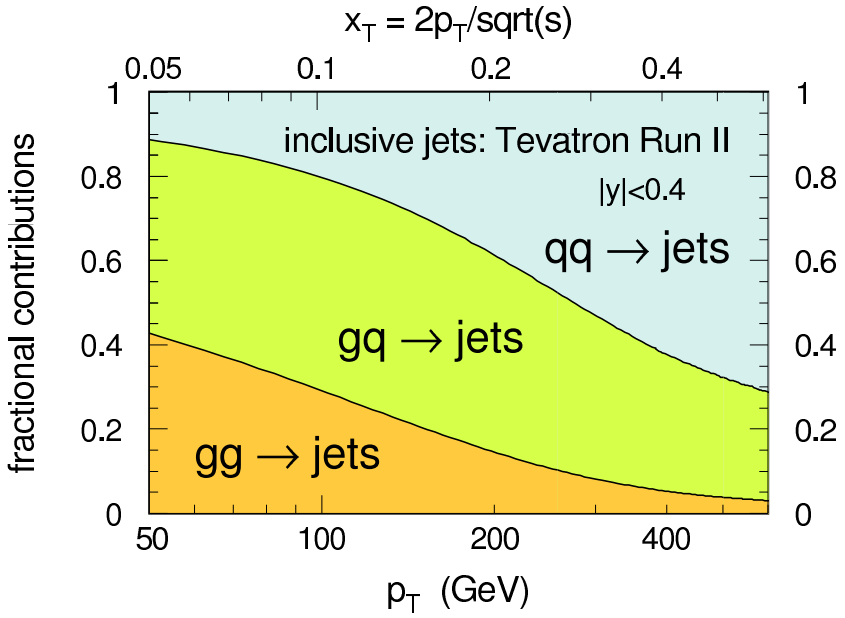

Figure 1.1: Gluon contribution to the inclusive jet cross section for central jets.

diated and its properties can be investigated. The total production cross section ($\frac{\mathrm{d}\sigma}{\mathrm{d}M_{3\mathrm{jet}}}(p\bar{p} \to 3\,\mathrm{jets} + X)$) in three-jet mass $M_{3\mathrm{jet}}$ presented in this thesis investigates the global properties of the three-jet system. As such, the total mass of the three-jet system in the TeV range represents the hardest objects produced at the Tevatron (large fraction of the initial energy is transferred into the three-jet final state). The cross section calculations are also available at NLO (combining $2 \to 4$ real and $2 \to 3 + 1\,\mathrm{loop}$ contributions). Comparing the rate of 3- to 2- jet events, the strong coupling constant α_S can potentially be determined. Additionally, the three-jet system needs to be described by more variables than the dijet system (Sec. 6.2) all of which can be also computed at NLO. Three-jet final state is the lowest final state where energy distribution of partons inside jets can be studied. For example, when two of the three jets are positively identified ("tagged") as originating from b-quarks, the third remaining jet should come from the gluon radiation (neglecting possible higher order contribution from quarks).

Historically, the three-jet final state was first observed by the TASSO collaboration at the PETRA e^+e^- accelerator in the late 1970s[8]. This observation was interpreted as the evidence for the gluon and for the Quantum chromodynamics as the underlying theory of the strong interaction. Three-

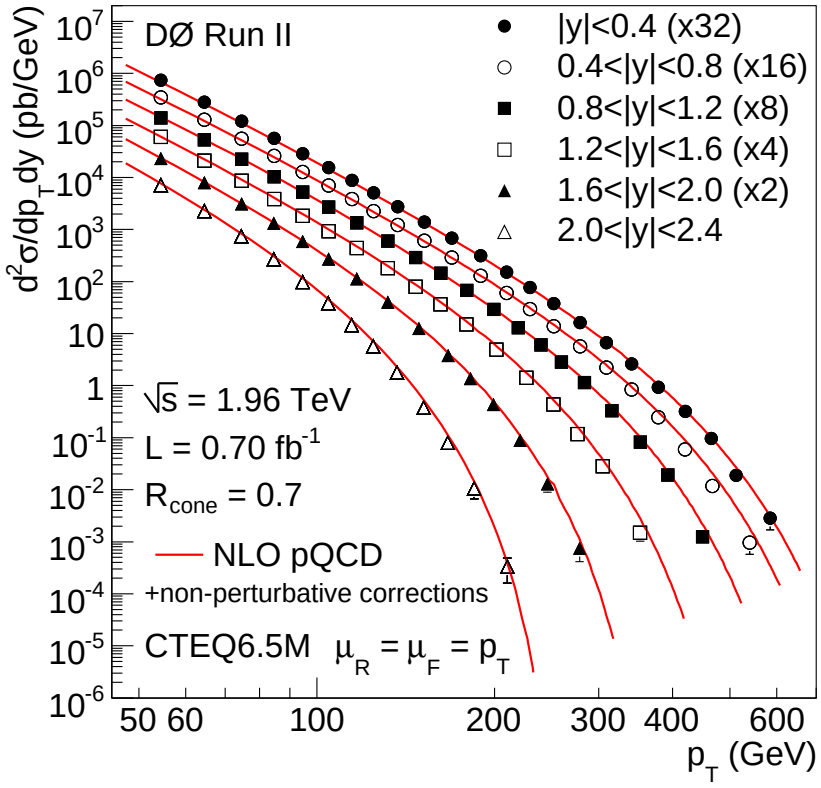

Figure 1.2: DØ inclusive jet cross section measurement in six bins of jet rapidity. Taken from [4].

jet final properties were further investigated for example by the MARK-J, JADE, TASSO[9] collaborations as well as the LEP e^+e^- collider experiments [10]. They were able to rule out scalar gluon theory in favor of spin-1 gluon predicted by QCD as well as to measure a difference in fragmentation between quarks and gluons.

At the hadron colliders, three-jet production was observed and studied by the UA1[11] and UA2[12] collaborations (in the 1980s) at the S$p\bar{p}$S Collider, by the CMOR collaboration[13] at the ISR and later by the DØ[14] and CDF[15] collaborations at the Tevatron accelerator during Run I (1990s). The first measurements were only compared to the tree level prediction of the QCD since the higher order predictions were not available at that time. In the recent past, the next-to-leading order calculations became available and tested with the Run I data[16]. Most of the measurements concentrated on the topological distributions of the three-jet final state.

The measurement in this thesis naturally extends the previous measure-

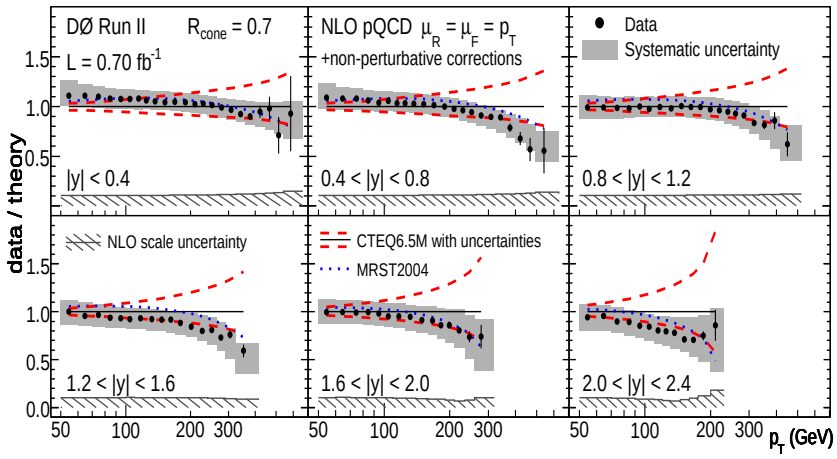

Figure 1.3: DØ inclusive jet cross section compared to next-to-leading order QCD predictions. Taken from [4].

ments. The higher center of mass energy available now at the Tevatron accelerator together with an order of magnitude higher luminosity offers a large sample of three-jet events not limited by statistics. The phase space cuts used in this analysis focus on high energy limits not available in the previous measurements. The theoretical calculations are available at the next-to-leading order with the latest knowledge of the proton structure functions.

1.2 Thesis Structure

This thesis is organized as follows: After this general introduction, Chapter 2 describes how the theoretical framework of QCD with quarks and gluons leads to a definition of jets. It compiles the theory information from various textbooks and lectures. Then the jet algorithm description (Chapter 3) is given as this is the connection between the theory and experiment. That chapter is based on my experience as a jet algorithm maintainer at DØ (I was responsible for jet code development within the DØ and *cafe* software frameworks). The only new information presented in this chapter is coming from my contribution to the TeV4LHC Workshop[17] which was also published in [18]. The next chapter contains the description of the DØ experiment in Fermi National Accelerator Laboratory (FNAL) in Batavia, Illinois, USA and is mostly taken from [19] since I did not directly participate on hardware work (except of serving 124 combined calorimeter and muon (CALMUO) shifts in the DØ Control Room). Chapter 5 describes the effort of Jet Energy Scale

Group (JES Group[20][21]) of which I was a member, to properly calibrate jet energies in Run IIa data taking period. The project, which took more than two years to complete, lead to the best achieved precision on jet energy scale determination at a hadron collider. The precision of 1–2% in most of the kinematic region results in reduced experimental uncertainties of jet measurements and will be challenging to be achieved at the LHC collider for many years. The results are documented in hundreds of presentations at internal meetings and in several DØ Notes[22], [23], [24] and on public web pages[25], [26]. The final version is also intended to be published in Nuclear Instruments and Methods. The final chapter of the thesis describes the measurement of the three-jet cross section. It is based on my own work partially using cited results of others.

2 Quantum Chromodynamics

2.1 Standard Model Overview

The Standard Model (SM) of particle physics is a theory which describes all particles that make up matter and the interaction among those particles. Out of four known types of interactions it unites electromagnetic, weak and strong interactions into a single theory. Gravitational interaction is not considered. According to the Standard Model, all matter is formed by three generations of particles (Table 2.1). The forces are mediated by gauge bosons as the force carriers. The mass of particles is generated by the interaction with the Higgs boson (currently yet to be confirmed).

Historically, the key points of the Standard Model, both theoretical and experimental are

- **Particle zoo** - Long list of newly discovered particles which needed some sort of organization (I. Rabi famous quote "Who ordered that?").
- **Local gauge invariance** - The success of Quantum electrodynamics and the extension towards non-abelian theories (Yang-Mills).
- **Deep inelastic scattering** - Scattering experiments at SLAC revealed the substructure of protons.

The Standard Model is a quantum field theory with local gauge invariance as one of the main principles. The gauge group is $SU(3) \times SU(2) \times U(1)$. It means that the Lagrangian of the theory is invariant under local symmetry transformations of this group. Currently, all matter particles are divided into three generations, all interactions are assigned mediating particles.

The key features of the Standard Model are

- **Electroweak interaction** - Unification of electromagnetic and weak interactions.
- **Higgs particle** - Spontaneous symmetry breaking and mass generation in the Standard Model.

- **QCD** - Theory of strong interaction describing the structure and dynamics of hadrons.

	1st generation	2nd generation	3rd generation
Quarks	u (up)	c (charm)	t (top)
	d (down)	s (strange)	b (bottom)
Leptons	e^- (electron)	μ^- (muon)	τ^- (tau lepton)
Neutrinos	ν_e	ν_μ	ν_τ
	Forces		
Force Carriers	Electromagnetic	Weak	Strong
	γ (photon)	$W^\pm, Z^0$	g (gluons)
Higgs boson	H		

Table 2.1: Standard Model particles.

The SM has a very successful history; except for the Higgs boson, all other predicted particles were eventually discovered and the theory parameters were tested to a great precision. However, it is not the ultimate theory because of gravity which is not incorporated and because of many free parameters which values it can not explain. Also on more fundamental grounds it can not explain the origin and the particle content of the universe, its matter-antimatter asymmetry, the hierarchy problem (the huge difference between strengths of electroweak and gravitational forces) and other related issues.

2.2 Quantum Chromodynamics

2.2.1 Non-abelian Gauge Theories

Quantum chromodynamics (QCD) describes the strong interaction between quarks where gluons are the exchanged particles. It emerged from uniting at first sight two completely different theories proposed in the 1960s. The additive quark model[27] proposed to explain the number of then known particles, stated that each baryon consists of three quarks and each meson of quark-antiquark pair. This, along with the underlying $SU(3)$ symmetry, allowed one to organize particles into multiplets with similar quantum numbers. To explain why a baryon can contain three quarks (fermions) of the same flavor which is forbidden by Pauli exclusion principle, a new quantum number was proposed. The number, called "color" was assigned to each quark, but the requirement was that observable particles must be color singlets. The

second theory[3] was formulated to explain the results of deep inelastic scattering experiments of electrons on protons made in SLAC laboratory. These experiments suggested that protons consist of smaller constituents (named partons) which in the high energy limit behave as free particles. Physicists were looking for a theory which could comprise both phenomena that quarks can behave as free particles in the high energy limit and at the same time were not observed as free particles. Most people hardly believed that such theory fulfilling this requirement existed, but Gross, Politzer and Wilczek[28] laid out the foundations of Quantum chromodynamics by showing that this can be satisfied within non-abelian gauge theories (while originally they tried to prove the exact opposite).

QCD is built on analogy with Quantum electrodynamics (QED) with $SU(3)$ gauge group replacing the $U(1)$ of QED. As $SU(3)$ in a non-abelian group, this introduces new concepts which are not seen in QED. Since $SU(3)$ has 8 generators, there are 8 different mediating fields called gluons. A new quantum number is introduced for quarks called "color". Because of the non-abelian nature of the QCD gauge group, gluons also carry color and can interact among each other directly (whereas photon in QED can interact with other photon only via higher order effects).

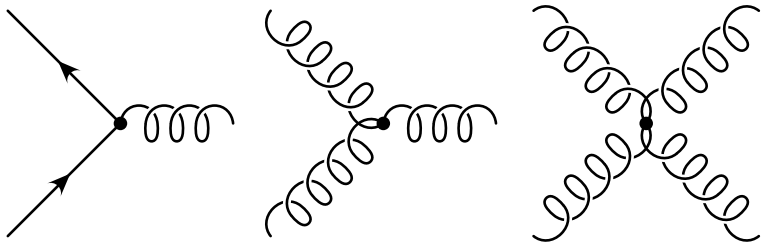

Figure 2.1: QCD interaction vertices.

The QCD Lagrangian can be constructed using the following line of thought. First, quarks are assumed to be fermions. Therefore, the (free) Lagrangian of all quark flavors is simply

$$\mathscr{L}_0 = \sum_f \bar{\psi}_f(\gamma^\mu \partial_\mu - m_f)\psi_f, \tag{2.1}$$

with ψ_f being the fermionic field of mass m_f, γ^μ are Dirac matrices and the sum can go over all considered flavors f. Then the interaction is added following the same way as in QED. The requirement of not changing physics using simple group transformation

$$\psi \to \psi' = U\psi \tag{2.2}$$

leads to an introduction of a field which interacts with the quark fields. Now the crucial thing is that the transformation in Eq. 2.2 does not have to be global (independent of space coordinates), but can be local (one can set his/her own coordinate system at each place) as

$$\psi' = U(x)\psi. \tag{2.3}$$

To keep the equation of motion the same, one needs to add more terms in the Lagrangian to satisfy the local gauge invariance. In the case of QCD and the gauge group $SU(3)$ this leads to

$$\mathscr{L} = -\frac{1}{4}F^a_{\mu\nu}F^{a\mu\nu} + \sum_f \overline{\psi}_f(\not{D} - m_f)\psi_f. \tag{2.4}$$

The first part then describes the kinetic term of the gluon field. The field strength tensor is

$$F^a_{\mu\nu} = \partial_\mu A^a_\nu - \partial_\nu A^a_\mu + g f^{abc} A^b_\mu A^c_\nu, \tag{2.5}$$

where the last term is coming from the local gauge invariance requirement ($a = 1, \ldots, 8$, f^{abc} are structure constants of $SU(3)$ and g is the coupling constant). This term is responsible for the gluon self-interaction (Fig. 2.1) and thus for the different behavior between QCD and QED.

$$D_\mu = \partial_\mu - igA^a_\mu T^a, \tag{2.6}$$

is the covariant derivative which replaces the standard derivative in the Lagrangian. T^a are the generators of the SU(3) group and $\not{D} = \gamma^\mu D_\mu$ is the standard notation.

The equations of motion can be derived from the Lagrangian, unfortunately they are too difficult to be solved directly. Instead, approximate methods of perturbation theory are used. In these methods, the complicated system is approximated in terms of a simpler one. The solution for free Lagrangian can be computed and then the interaction piece is taken as a small disturbance to the system. For each scattering vertex in Fig. 2.1 a Feynman rule can be derived from the QCD Lagrangian. Then for an arbitrary order, the scattering matrix element can be (in principle) constructed using the rules.

In the lowest order, the corresponding Feynman diagrams do not contain any loops. At higher orders, loops must be taken into account and their contribution must be added. The integrals in these loops are performed over all momenta of the particles in the loop, making the contribution infinite

as $p \to \infty$. The treatment of these so-called ultra-violet (UV) divergences involves a "regularization" procedure. For this procedure, either a simple momentum cut-off or a more complicated dimensional regularization can be used. In the end, the regularized divergences are absorbed into the redefined coupling constants, vertices and fields. This is done in a specific renormalization scheme (which can be arbitrary) and which introduces a renormalization scale μ_r. The renormalized strong coupling constant as well as the coefficients in the perturbative expansion of a cross section depend on the choice of renormalization scheme and scale. However, the requirement that the observable quantities should be independent on the scale constrains the μ dependence of the renormalized quantities. The renormalized strong coupling constant satisfies

$$\frac{\mathrm{d}\alpha_S(\mu/\Lambda)}{\mathrm{d}\ln(\mu/\Lambda)} = \beta(\alpha_S(\mu/\Lambda)). \tag{2.7}$$

In order to get the scale μ a dimension of energy, an additional parameter Λ has to be introduced with a dimension of energy as the α_S is a dimensionless quantity. The β function expanded in a series in powers of α_S in the lowest order for QCD gives

$$\beta(\alpha_S) = \frac{-\alpha_S^2}{2\pi}\left(\frac{11}{3}N_c - \frac{4}{3}\frac{N_f}{2}\right). \tag{2.8}$$

In the lowest order, one can easily solve the equation for $\alpha_S(\mu/\Lambda)$ to get

$$\alpha_S(\mu/\Lambda) = \frac{1}{b\ln(\mu/\Lambda)}, \tag{2.9}$$

where b corresponds to the numerical constants from Eq. 2.8. For a small number of flavors $N_f \leq 16$ (where SM has 3 generations = 6 flavors and $N_c = 3$ colors), the strong coupling constant decreases with increasing μ and vanishes for $\mu \to \infty$, or in other words, the particles behave as free (asymptotic freedom). On the other side, with very low energies (long distances) and μ approaching Λ, the coupling blows to infinity which might suggest the confinement phenomenon, but more accurately it tells that the perturbative predictions become unreliable. The typical scale of non-perturbative effects is of the order of 1 fm which corresponds to $\Lambda \sim 200\,\mathrm{MeV}$.

Other infinities are infra-red (IR) and mass singularities coming from configurations where two partons (quarks or gluons) become collinear or one of the partons has a vanishing energy. These are situations when it becomes impossible to distinguish such parton(s). The IR singularities will cancel if all physically indistinguishable initial and final states are correctly taken into account in the definition of the physics observables.

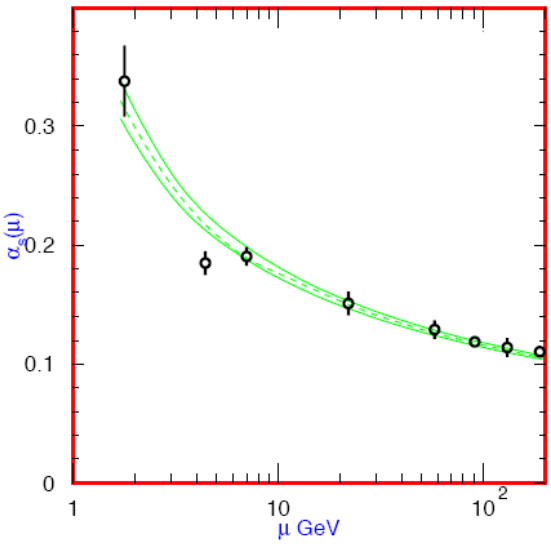

Figure 2.2: Demonstration of the running coupling from several independent measurements. Taken from [29].

The QCD splitting functions $P_{ab}(x)$ which describe the probability that parton b emits parton a with a given fraction of the original parton momentum x can indeed have singularities in some parts of the phase space. Leading order calculations are shown in Eqs. 2.10–2.13.

$$P_{qq}^{(0)}(x) = P_{\bar{q}\bar{q}}^{(0)}(x) = \frac{4}{3}\left[\frac{1+x^2}{1-x}\right]_+, \tag{2.10}$$

$$P_{gq}^{(0)}(x) = P_{g\bar{q}}^{(0)}(x) = \frac{4}{3}\left[\frac{1+(1-x)^2}{x}\right], \tag{2.11}$$

$$P_{qg}^{(0)}(x) = P_{\bar{q}g}^{(0)}(x) = \left[\frac{x^2+(1-x)^2}{2}\right], \tag{2.12}$$

$$P_{gg}^{(0)}(x) = 6\Big(\left[\frac{x}{1-x}\right]_+ + \frac{1-x}{x} + x(1-x) + \big(\frac{33-2N_f}{36} - 1\big)\delta(1-x)\Big), \tag{2.13}$$

with the +-distribution defined as

$$[f(x)]_+ = \lim_{\beta\to 0}\left(f(x)\theta(1-x-\beta) - \delta(1-x-\beta)\int_0^{1-\beta} f(y)\mathrm{d}y\right) \tag{2.14}$$

From the splitting functions, it can be derived that the probability for a quark to emit a very soft ($E \to 0$) or collinear gluon is infinite,

$$\mathrm{d}P \propto \alpha_\mathrm{S}\frac{\mathrm{d}\theta}{\theta}\frac{\mathrm{d}k_T}{k_T}, \tag{2.15}$$

where θ is the opening angle between the scattered quark and radiated gluon and k_T is the relative transverse momentum between the two. One can imagine that the quark is always surrounded by a cloud of gluons. It is impossible to compute any cross section with infinite number of particles but as well to observe these particles in a real detector. Instead one needs to define an object (jet) which contains all quarks and gluons which are near each other in some sense and physically indistinguishable and take only this jet as an observable quantity.

2.2.2 Proton Structure

Now, the deep inelastic scattering (DIS) experiments at SLAC can be explained in the following way. At low energy the electron scatters on the whole proton. As the incident energy increases, the electron is able to resolve the inner constituents of the proton. In the additive quark model, the proton consists of 3 quarks (uud). The cross section for the electron-proton scattering should contain a sum of the contributions of individual electron-quark scattering, each weighted by the probability of finding a quark of given flavor in the proton $f_i(x)$ (x being the fraction of the proton momentum carried by the quark). The parton distribution functions (PDFs) $f_i(x)$ can be actually measured in DIS experiments. Clearly, already the first DIS experiments showed that the distribution functions are not delta functions which would be the case of additive 3 quark model and QCD was able to offer an explanation. From momentum sum rules, the total momentum of quarks didn't add up to the total momentum of the proton. This is a sign of gluons which carry the remaining part. Second, it is the permanent interaction between quarks and gluons which smears the delta function behavior. This is controlled by the splitting functions and due to this, the distribution functions also depend on a factorization scale. The factorization scale determines the maximal virtuality of a parton which enters the scattering. Unfortunately, the proton structure cannot be computed in pQCD, only its dependence on the factorization scale M, which is governed by so called DGLAP (or evolution) equations (Eqs. 2.16–2.18), can be predicted.

$$\frac{\mathrm{d}q_i(x,M)}{\mathrm{d}\ln M} = \frac{\alpha_S(M)}{\pi}\left[\int_x^1 \frac{\mathrm{d}y}{y} P_{qq}\left(\frac{x}{y}\right) q_i(y,M) + \int_x^1 \frac{\mathrm{d}y}{y} P_{qg}\left(\frac{x}{y}\right) g(y,M)\right], \tag{2.16}$$

$$\frac{\mathrm{d}\bar{q}_i(x,M)}{\mathrm{d}\ln M} = \frac{\alpha_S(M)}{\pi}\left[\int_x^1 \frac{\mathrm{d}y}{y} P_{qq}\left(\frac{x}{y}\right) \bar{q}_i(y,M) + \int_x^1 \frac{\mathrm{d}y}{y} P_{qg}\left(\frac{x}{y}\right) g(y,M)\right], \tag{2.17}$$

$$\frac{\mathrm{d}g(x,M)}{\mathrm{d}\ln M} = \frac{\alpha_S(M)}{\pi}\left[\sum_{i=1}^{n_f}\int_x^1 \frac{\mathrm{d}y}{y} P_{gq}\left(\frac{x}{y}\right)\left(q_i(y,M)+\bar{q}_i(y,M)\right) + \right.$$
$$\left. + \int_x^1 \frac{\mathrm{d}y}{y} P_{gg}\left(\frac{x}{y}\right) g(y,M)\right]. \tag{2.18}$$

The structure functions have to be measured at some momentum scale in an experiment and then evolved to other scales. Their important property is the concept of universality which assumes that the structure functions measured in one process can be applied in another one.

The electron in DIS scatters on the proton incoherently. The total cross section is given by the sum of individual partonic cross sections weighted by the probabilities to find those partons in a proton (structure functions). The fact why the sum is incoherent (i.e no interference between two terms) comes from the picture in hadron's infinite momentum frame where the electron has time to interact only with a single parton.

Finally, the concept can be extended to the hadron-hadron scattering and the cross section for $p\bar{p} \to X$ is then written as

$$\sigma(p\bar{p} \to X) = \sum_{a,b}\int_{x_1,x_2} \mathrm{d}x_1 \mathrm{d}x_2 f_{a/A}(x_1,\mu_f^2) f_{b/B}(x_2,\mu_f^2)\sigma(a+b\to X,\mu_r^2,\mu_f^2), \tag{2.19}$$

where μ_f is the factorization scale and μ_r is the renormalization scale. The cross section is computed as a sum of all relevant parton-parton interactions, for which matrix elements can be computed in the perturbative theory, weighted by the PDFs.

Finally, the scattered partons need to hadronize since only hadrons are observed. There is no useful prescription given by the theory and only models are used in simulations of scatterings.

After defining the jet algorithm, the cross section for n-jet production can be computed if some general rules are satisfied (see Chapter 3 for details).

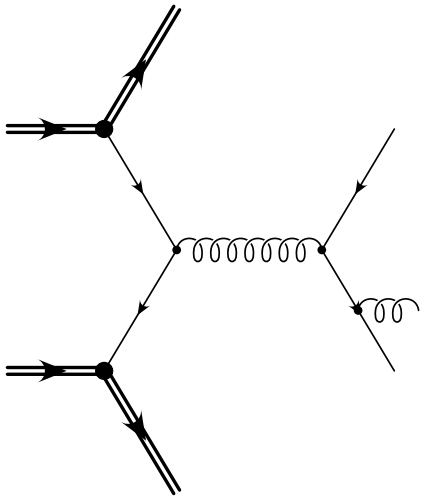

Figure 2.3: Schematic diagram of the three jet production.

In this thesis, the inclusive 3 jet production is investigated. From Eq. 2.19:

$$\sigma(p\bar{p} \to 3\text{jets}+X) = \sum_{a,b} \int_{x_1,x_2} \mathrm{d}x_1 \mathrm{d}x_2 f_{a/A}(x_1,\mu^2) f_{b/B}(x_2,\mu^2) \sigma(a+b \to 3\text{jets},\mu^2), \tag{2.20}$$

where for simplicity of notation the two different scales are shown as one (the renormalization scale is in principle independent of the factorization scale, but in the calculations in this thesis a single common scale will be used).

2.2.3 Leading Order Calculations

In the leading order, the partonic cross sections are generally quite simple. Monte Carlo generators are used to randomly generate events according to the cross section. Leading order (LO) generators can be separated into two classes. The most common generators PYTHIA[30] and HERWIG[31] are using LO matrix elements for $2 \to 2$ processes and the third jet is simulated according to a phenomenological model implemented in a given generator (so-called parton showering). The agreement with data can be poor unless the phenomenological model is fine-tuned. The second class, for example ALPGEN[32] and SHERPA[33] are using full LO $2 \to 3$ matrix elements which should improve the agreement by including additional Feynman diagrams.

At the DØ experiment, PYTHIA is the standard generator which is used for modeling the scattering processes. It is available in large samples together with detailed detector simulation (GEANT[34]) which helps to study system-

atical effects on the three-jet cross section. SHERPA is used in the procedure of unfolding the detector resolutions because the standard version of PYTHIA does not provide an accurate description of the three-jet final state.

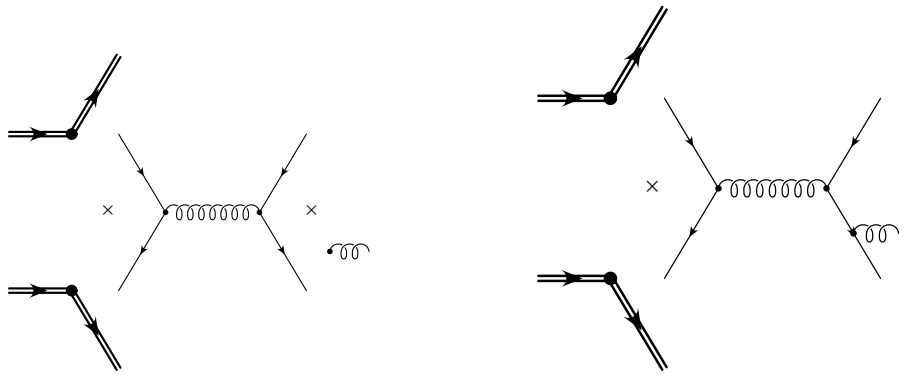

Figure 2.4: Schematic diagrams of the three jet production in leading order Monte Carlo generators. Actual matrix elements contain all allowed combinations of quarks and gluons in the diagram. Parton shower Monte Carlo is using $2 \to 2$ matrix elements and additional jets are simulated with a showering model (left). LO $2 \to 3$ generators include all allowed diagrams for 3 parton production (right).

2.2.4 Next-to-leading Order Computation

For some kind of processes (like two or three jet productions, vector boson+jet, ...) the next-to-leading order matrix elements are known and the cross section can be computed using specialized programs like NLOJET++[35]. In the schematic picture in Fig. 2.4 (right) all diagrams for $2 \to 4$ real production and diagrams $2 \to 3$ with 1 loop are included. The crucial problem is the presence of divergences present both in the real and virtual diagrams. For an infrared and collinear safe cross section these divergences should exactly cancel; however the exact numerical cancellations can be difficult to achieve.

$$\sigma = \sigma^{\mathrm{LO}} + \sigma^{\mathrm{NLO}} \tag{2.21}$$

$$\sigma^{\mathrm{NLO}} = \int \mathrm{d}\sigma^{\mathrm{NLO}} = \int_{m+1} \mathrm{d}\sigma^{\mathrm{real}} + \int_{m} \mathrm{d}\sigma^{\mathrm{virtual}} \tag{2.22}$$

In general there are two approaches to the numerical calculations, namely phase space slicing and subtraction methods. The phase space slicing is

based on approximating the matrix elements and the phase space integration measure in boundary regions of phase space so integration may be carried out analytically[36]. In subtraction methods, a counter term is added to Eq. 2.22 such as

$$\sigma^{\mathrm{NLO}} = \int \mathrm{d}\sigma^{\mathrm{NLO}} = \int_{m+1} \left[\mathrm{d}\sigma^{\mathrm{real}} - \mathrm{d}\sigma^{\mathrm{counter}}\right] + \int_{m+1} \mathrm{d}\sigma^{\mathrm{counter}} + \int_{m} \mathrm{d}\sigma^{\mathrm{virtual}}, \tag{2.23}$$

which has the same singular behavior as the real part. Now the first integral can be numerically integrated and the remaining step is to find a form of $\sigma^{\mathrm{counter}}$ that can be integrated over 1 parton subspace leading to poles which cancel with those in $\sigma^{\mathrm{virtual}}$ and the consequent integral can be integrated over the m parton space.

The next-to-leading order calculations in this thesis are provided using NLOJET++ program which uses a modified subtraction method of [37].

3 Jets and Jet Algorithms

One of the important discoveries of high energy physics in the late sixties and early seventies was the confirmation of production of jets[39]. The formation of jets from the theoretical point of view was explained in the previous chapter. This chapter provides a description of the so-called jet algorithms. Their purpose is to quantify topological features of hadronic energy flow in scattering processes. Jet algorithm is a tool which enables confrontation of experimental results (jets found in the detector) with theoretical predictions (jets in the theory of partons).

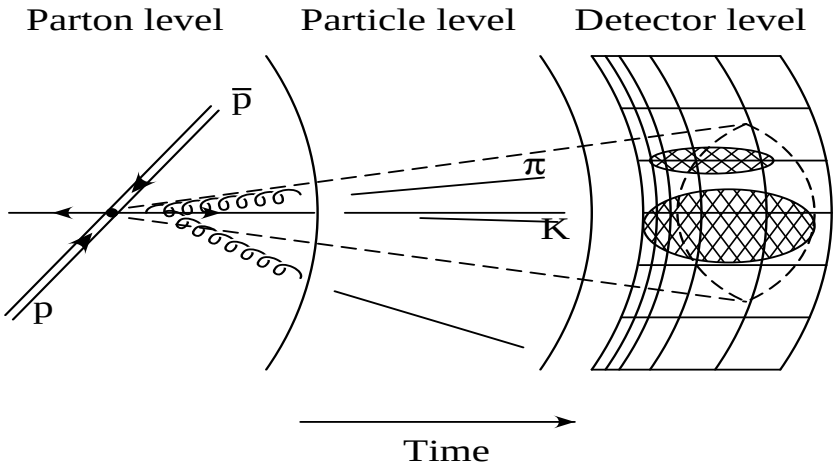

Figure 3.1: Evolution of the hadron-hadron scattering process showing different levels of jet definition.

The perturbative calculation of the hadron-hadron cross section has been described in the previous chapter. After the parton-parton interaction and after hadronization, the products of the collisions are detected in the experimental devices (Fig. 3.1 for a schematic view). According to the cartoon, three different jet levels can be defined; parton, particle (or hadron) and detector level jets. It also shows that only a consistent definition of a jet al-

gorithm on all of these levels makes sense in order to compare the calculations to the real data.

At the DØ experiment, the data and predictions are compared at the particle level. Parton calculations are corrected using a simulation of the hadronization to the particle level, while the detector effects are corrected from the detector jets back to the particle level. In this case, the results can be used in the future since all the detector effects which depend on the DØ settings are removed and detector effects are not mixed with theory model dependent parts.

3.1 Jet Algorithms

From an experimental point of view, inelastic high energy particle collisions lead to a high multiplicity of particles measured in the detector apparatus. In some of the events jets can be identified easily by looking at the energy depositions in the detector. On the other hand, the signal (jet with high transverse momentum with respect to the original beam axis) is usually buried in the detector noise and such visual detection becomes ambiguous (Fig. 3.2). With the large statistics of events produced by modern colliders, it is virtually impossible to scan every event visually and search for jets. For jet finding, a tool must be implemented which can find jets as efficiently as possible (given the constraints like time, noise present in the data, reconstruction efficiencies and others).

An excellent review of the general requirements on jet algorithms is given in [40]. It summarizes the improvements on the jet understanding up to the start of Run II of the Tevatron and served as a guideline for Run II jet algorithm implementations.

In the following subsections, the general properties which should be fulfilled by a good jet algorithm and then the description of two main classes of algorithms currently used at hadron colliders will be given with details particularly important to the DØ experiment (midpoint cone algorithm and its energy calibration).

3.1.1 General Algorithm Properties

Generally, it must be possible to run the same jet algorithm on both the theoretical predictions and experimental results. So the definition must be clear, fully specified and should not introduce additional procedures on either theoretical or experimental side.

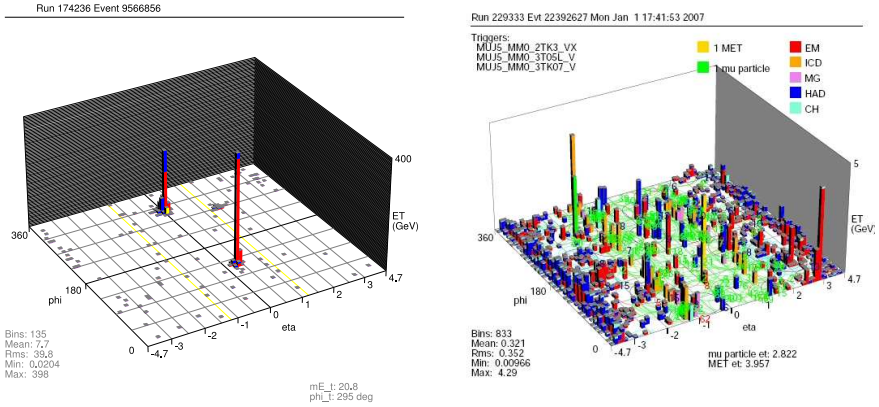

Figure 3.2: Example of two event displays from the DØ experiment. Clean high p_T dijet event on the left and typical muon triggered event on the right.

3.1.1.1 Experimental Properties

From the experimental point of view, the properties of a good jet algorithm can be easily summarized. The details of the algorithm should be clearly as much as possible independent of the structure of the detector. The algorithm must be as time and CPU efficient as possible and it must allow an easy and straightforward energy scale calibration.

3.1.1.2 Theoretical Properties

From the theoretical point of view, the most important property of the jet algorithm is the infrared and collinear safety. The QCD theory calculation diverges if either of the partons has a vanishing energy or any two partons are collinear. An algorithm is not infrared safe when the jet multiplicity can be changed by adding a soft parton somewhere in the event. In the same way, an algorithm is not collinear safe if the jet multiplicity changes by splitting one parton into two collinear ones.

Additionally, boost invariance is another requirement. In hadron collisions when only two partons from either hadron collide, the center of mass system of the two partons is generally boosted in the beam direction (neglecting a small intrinsic transverse momentum of partons within hadrons). Therefore, variables used in the jet definition should be boost invariant as jets are defined in the laboratory frame.

3.1.1.3 Algorithm Steps

Each algorithm consists at least of two important steps.

1. Clustering: In this step the description how the particles are clustered into a jet is given.

2. Physical quantities determination: This step describes how the physical properties (e.g., energy and momentum) are computed.

Additional steps can be added to the prescription. For example, the preclustering step might need to be added in order to significantly reduce the total amount of particles entering the algorithm. The preclustering must not compromise the general requirement on the algorithm (IR safety, ...). In the case when jets found by the clustering overlap, additional procedures (e.g splitting and merging) must be given.

3.2 k_T Algorithm

k_T algorithms are generally advanced over the cone algorithms. However, historically they were used mostly in e^+e^- collisions with only a few quite recent results from hadron colliders (for example [41], [42]). By definition (see below) they do not suffer from collinear or infra red instabilities. Also, by construction, k_T jets do not overlap so the additional splitting/merging step is not needed.

The disadvantages of the k_T algorithm are computer intensity, unknown behavior with respect to the soft underlying part of the interaction and the energy calibration issues. The usual implementations of the k_T algorithm usually behave as N^3 with N being the number of particles entering the algorithm. This has been proved very time consuming with $O(10000)$ towers in modern calorimeters, so heavy preclustering must be used (faster implementations are recently being studied). There was a common fear that k_T jets will function as a "vacuum cleaner" and suck inside parts of the underlying event (low p_T particles) and that this effect will be difficult to calibrate for in the jet energy scale correction.

Several implementations of k_T algorithm do exist. The brief description given here (and used by DØ reconstruction program) follows the Ellis & Soper type[43].

The algorithm starts with the list of particles (calorimeter towers, particles or partons). The algorithm recursively groups pairs of items from the list to form the jets. The idea is that items with nearly parallel momenta (small relative transverse momenta) should be joined to form a jet.

For each particle, define

$$d_i = p_{T,i}^2 \tag{3.1}$$

and for each pair of particles define

$$d_{ij} = \min(p_{T,i}^2, p_{T,j}^2)\frac{(y_i - y_j)^2 + (\phi_i - \phi_j)^2}{D^2}. \tag{3.2}$$

Then find the smallest value of all d_i and d_{ij} ($d_{\min}$). If $d_{\min}$ is a d_{ij}, merge items i and j into a new item $p_{\text{new}} = (E_{\text{new}}, \mathbf{p}_{\text{new}})$ using the E-scheme

$$E_{\text{new}} = E_i + E_j, \tag{3.3}$$

$$\mathbf{p}_{\text{new}} = \mathbf{p}_i + \mathbf{p}_j. \tag{3.4}$$

If $d_{\min}$ is a d_i, remove the corresponding item from the input list and add it to the list of final jets. Repeat until there are not any remaining items in the input list. D parameter controls the size of the jet, its typical values range from 0.4 to 1.

3.3 Cone Algorithm

Although the k_T algorithm is theoretically more favored the main jet algorithm used at DØ is a cone algorithm. The algorithm evolved from the original idea by Sterman and Weinberg[44]. The underlying idea is that when a parton showers, large angle emissions are suppressed and most of the shower stays within a cone around the original parton. The main parameter of the algorithm is the cone radius (or the cone opening angle) which determines which partons will be clustered in a single jet (cone). Many experiments in the 1980s used their own jet algorithm, so a common definition known as the Snowmass Accord was proposed before the start of Run I of the Tevatron. In the end, both CDF and DØ decided to use their own implementation and their algorithms were different. It was found that the Snowmass-type algorithms are not infrared safe and a midpoint solution was recommended[40].

3.3.1 DØ Run II Cone Algorithm Implementation

DØ implements the midpoint-type cone algorithm as described in [45]. From calorimeter cells, pseudoprojective towers are formed by adding the four-momenta of the calorimeter cells. Each cell is assumed to be massless and its momentum vector is defined by the direction between the primary vertex of the interaction and the center of the cell. Cells are only used if their signal is larger than 2.5 width of their pedestal values (width of the electronic noise,

2.5σ). Cells can be also removed if their signal is less than 4σ and no neighbor cell has a signal above 4σ. The momentum of each cell is defined with respect to the primary vertex found by the tracking system. Therefore tower consisting of at least two cells with non-collinear momenta will acquire mass in this procedure. Then calorimeter towers with $p_T \geq 500\,\mathrm{MeV}$ are used as seeds to form preclusters by a simple cone algorithm. Simple cone algorithm only adds all towers with $p_T > 1\,\mathrm{MeV}$ lying within $R_{\mathrm{cone}} = 0.3$ of the center. All towers added to a precluster are removed from the list. Therefore two preclusters cannot overlap and will not share any towers. Preclusters with $p_T < 1\,\mathrm{GeV}$ are removed from the list. Remaining preclusters serve as seeds for the main algorithm. The overall goal of preclustering is to reduce the number of starting seeds because of computing complexity.

Next, a cone of radius R_{cone} is formed around each precluster. The value of the cone radius is a compromise between the corrections for hadronization and underlying event. Generally, the underlying event correction increases with the cone area while the hadronization correction decreases. At DØ experiment the values of $R_{\mathrm{cone}} = 0.5$ and 0.7 are used. The smaller values are used for example in reconstruction of top quark decays where more resolved jets are preferred. The QCD-oriented measurements prefer larger value (0.7) to minimize the theoretical uncertainty of hadronization while the underlying event energy is not that important for very high p_T jets. The new jet candidate center is computed using the E-scheme

$$p_{\mathrm{jet}} = (E_{\mathrm{jet}}, \mathbf{p}_{\mathrm{jet}}) = \sum_i (E_{\mathrm{i}}, \mathbf{p}_{\mathrm{i}}), \tag{3.5}$$

$$y_{\mathrm{jet}} = \frac{1}{2} \ln \left(\frac{E_{\mathrm{jet}} + p_{z\mathrm{jet}}}{E_{\mathrm{jet}} - p_{z\mathrm{jet}}} \right), \tag{3.6}$$

$$\phi_{\mathrm{jet}} = \tan^{-1} \left(\frac{p_{y\mathrm{jet}}}{p_{x\mathrm{jet}}} \right), \tag{3.7}$$

$$p_{T\mathrm{jet}} = \sqrt{p_{x\mathrm{jet}}^2 + p_{y\mathrm{jet}}^2}, \tag{3.8}$$

where the sums are over all towers in the cone. When the new axis does not coincide with the original one, the procedure is reiterated with the new axis as the starting one, until a stable solution is found. Stable solutions are called protojets. The sensitivity to soft radiation is reduced by adding midpoints between pairs of protojets and repeating the iterative procedure for these midpoints. The difference between the original recommendation and the actual implementation is that midpoint are added only between protojets and not between seeds. They are only placed between pairs of protojets ignoring higher orders (triplets, *etc* ...) and only if the distance

between the two protojets ΔR satisfies

$$R_{\text{cone}} < \Delta R < 2R_{\text{cone}}. \tag{3.9}$$

The final step of the algorithm involves treating overlapping protojets (i.e. protojets which share at least one tower with at least one other protojet). Given the p_T ordered list of protojets, coming from the highest-p_T jet which shares a tower with other protojet, the two protojets can be either split or merged depending how much energy they share. If the fraction shared is more than 50% of the p_T of the lower p_T protojet, protojets are merged into one. Otherwise, the shared towers are assigned to the closest protojet in the ΔR measure. Jet four-momenta are recomputed again, list of overlapping protojets is reordered and the procedure is reiterated until there is no more overlap. Finally, to get rid of physically unmeaningful jets, those with p_T below 6 GeV are discarded.

3.4 Recent Improvements in Jet Algorithms

Early in Run II it was shown by the CDF collaboration that midpoint type algorithms have some unexpected features. The main concern is the so-called "dark towers" problem where some high p_T towers can remain unclustered to any jet and potentially cause problems to correct jet energy measurement. This has led CDF to modify their algorithm to include a "Search Cone" feature where stable protojets are searched only with a smaller cone radius (usually $R_{\text{cone}}/2$) and only after they are stable, the cone radius is extended to the full size. The consequence is more stable protojets and in turn more overlapping jets which need to be split or merged.

DØ studied the "dark towers" problem during a series of Tevatron for LHC Workshops (TeV4LHC). This feature was quickly confirmed also for the DØ implementation of the midpoint algorithm (see Fig. 3.3 or [17]). DØ studied the unclustered towers using a second pass of the jet algorithm. It means that after the first running of the jet algorithm, all towers clustered into any jet are removed from the list of towers and then the full algorithm is rerun on the remaining list. Relatively high p_T jets were found using this algorithm. Their properties were studied as a function of their p_T and their distance to the nearest first pass jet. It was shown that the effect of second pass jets on the inclusive jet cross section is negligible for jets with transverse momentum over 50 GeV (see Fig. 3.4).

The problem of dark towers comes when one identifies all stable cone solutions. In the events with dark towers, some solutions are found not to be stable and starting with a seed around unclustered towers, the cone always

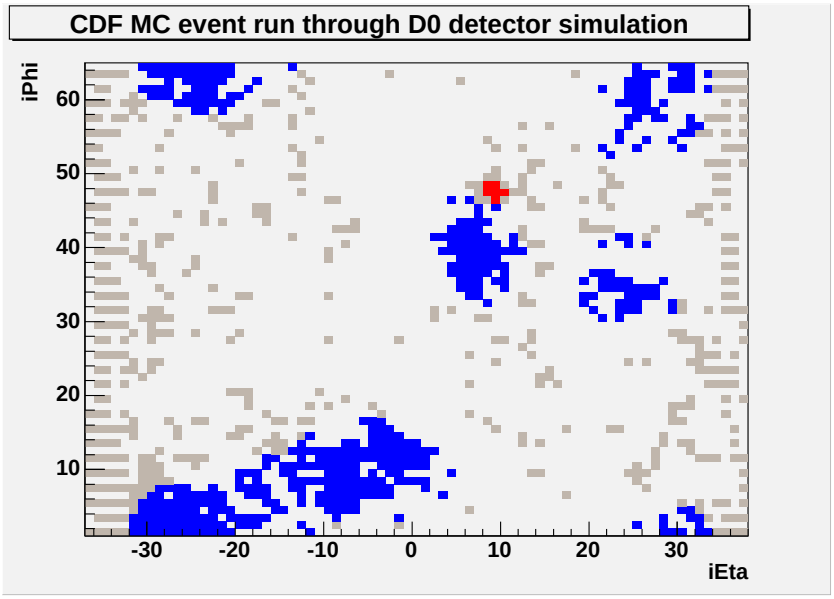

Figure 3.3: One of the Monte Carlo events supplied by the CDF experiment where DØ jet algorithm also leaves some high p_T towers unclustered. Blue squares correspond to towers clustered into jets. Red and gray squares are towers not clustered into any jet. Transverse momenta of red towers are larger than 2 GeV.

drifts away and finds a stable solution nearby. Only when the towers of this stable solution are removed, another stable cone can be found around the original seeds (the idea of a second pass of the jet algorithm). The solution to this problem is to avoid looking for stable solutions around seeds and use a seedless jet algorithm. This kind of algorithm is looking for all stable solutions and was already recommended before Run II in [40] but was never implemented because of computing complexity. Recently a new version was proposed, called Seedless Infrared Safe Cone algorithm (SISCone)[46] and its properties are being studied towards its potential use in the LHC experiments.

The k_T algorithm has also been improved. A faster implementation is now available where speed scales as $N^2 \log N$ instead of previous N^3 implemented in FastJet[47]. Another progress is the definition of the anti-k_T algorithm.

The k_T algorithm uses Eq. 3.2 as the distance measure

$$d_{ij} = \min(p_{T,i}^2, p_{T,j}^2) \frac{(y_i - y_j)^2 + (\phi_i - \phi_j)^2}{D^2}. \tag{3.10}$$

In the e^+e^- collisions, the so called Cambridge-Aachen algorithm was pro-

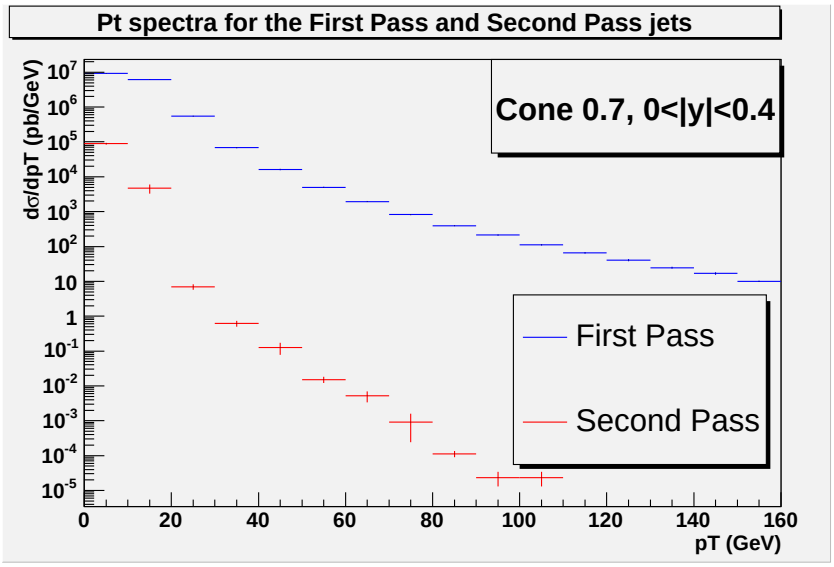

Figure 3.4: The inclusive jet spectra of first and second pass jets using DØ Monte Carlo simulation.

posed in [48] which clusters particles according to the distance between them:

$$d_{ij} = \frac{(y_i - y_j)^2 + (\phi_i - \phi_j)^2}{D^2}. \tag{3.11}$$

The Eqs. 3.4 and 3.4 can be generalized as

$$d_{ij} = \min(p_{T,i}^{2p}, p_{T,j}^{2p}) \frac{(y_i - y_j)^2 + (\phi_i - \phi_j)^2}{D^2}, \tag{3.12}$$

with a parameter p. The algorithm corresponding to $p = -1$ is called anti-k_T jet algorithm[49]. It combines the infrared and collinear safety features of the k_T algorithms with "preferred" regular shape of cone algorithms.

4 Experimental Setup

4.1 Accelerator Complex

The Fermilab accelerator complex consists of a chain of several accelerators where the well known accelerator – the Tevatron – is only the last piece in the chain (Fig. 4.1). In order to accelerate protons (and antiprotons) to almost 1 TeV, several machines have to be used due to technical limitations.

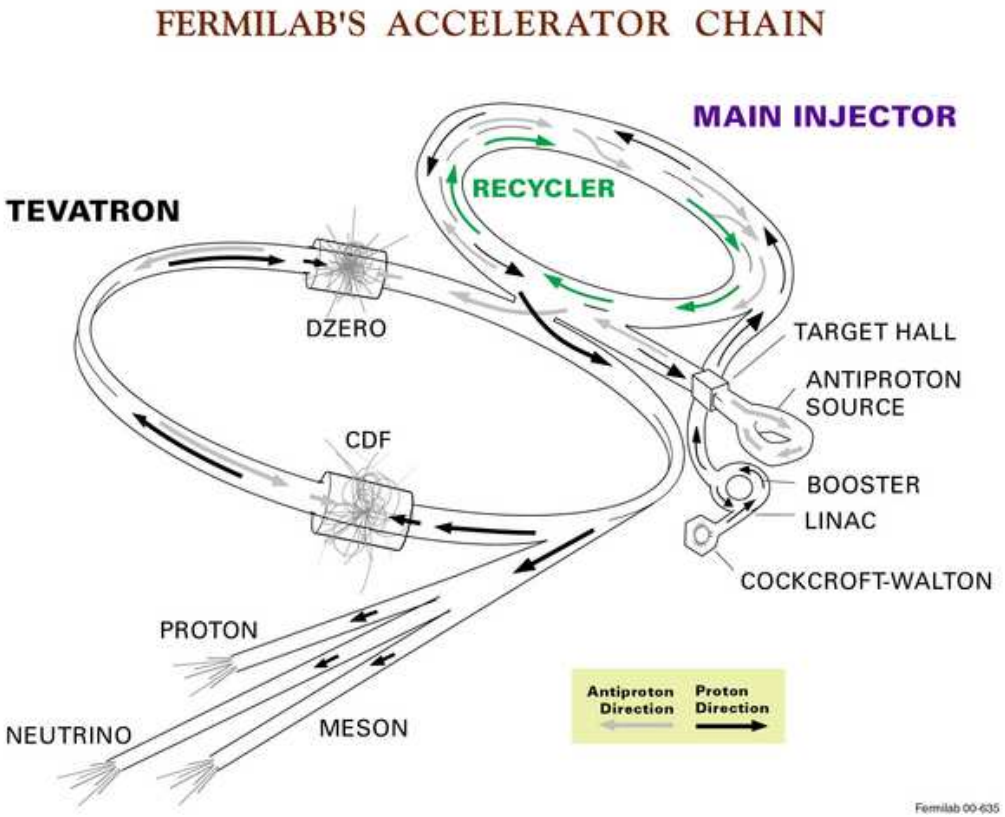

Figure 4.1: Schematic view of the accelerator complex.

The acceleration starts with a Cockroft-Walton pre-accelerator. Inside, the hydrogen gas is ionized to create negative ions (consisting of two electrons and one proton) and these ions are accelerated to reach an energy of 750 keV. The next step is a linear accelerator, Linac, where the ions energy reaches 400 MeV. Before the next step, the ions pass a carbon foil which strips the ions of both electrons and leaves only protons. The protons then enter the Booster where they are further accelerated to 8 GeV.

Afterwards, protons enter the Main Injector which serves several purposes. The Main Injector accelerates the protons to 150 GeV which is the starting energy for the final step, injection and acceleration in the Tevatron. The Main Injector also produces 120 GeV protons, which are used for antiproton production. It also receives the antiprotons from the Antiproton source and accelerates them to 150 GeV. Inside the Main Injector tunnel, the Antiproton Recycler is also located.

Antiprotons are produced in collisions of 120 GeV protons with a nickel target. The production efficiency is about twenty antiprotons out of 10^6 proton-target collisions. The antiprotons are picked up from produced particles by a magnet which selects only particles with the right charge and mass.

The last step in the chain is the Tevatron collider. It is a superconducting synchrotron accelerating protons and antiprotons from 150 GeV to 980 GeV. The period of acceleration lasts for about 40 seconds during which the beams circulate the accelerator about more than a million times. In each revolution, during passing the RF cavity, the beam increases its energy by a few hundred keV. Protons and antiprotons are kept at different trajectories but magnets at two places allow both beams to collide. At these two places two 5000-ton multipurpose detectors are located (CDF and DØ).

4.2 DØ Detector

The DØ detector is one of the two detectors operated on the Tevatron accelerator. Most of the detector details presented in the following sections are taken from the detector description published in [19].

The layout of the detector is similar to usual collider experiments. It has a central tracking detector for the reconstruction of tracks of charged particles and primary and secondary vertices. The tracker which is located in 2 T solenoidal magnetic field is followed by a liquid argon calorimeter where most particles deposit their energies. Muons are able to penetrate the whole calorimeter. Therefore, the outer layer of the detector is formed by three layers of muon systems. Neutrinos do not interact in the whole detector,

so their presence is determined indirectly by the asymmetry in the energy deposited in the calorimeter (by requiring the momentum conservation in the transverse plane). DØ detector uses right handed coordinate system with the $+z-$axis defined by the proton direction and $+y$ axis pointing upwards.

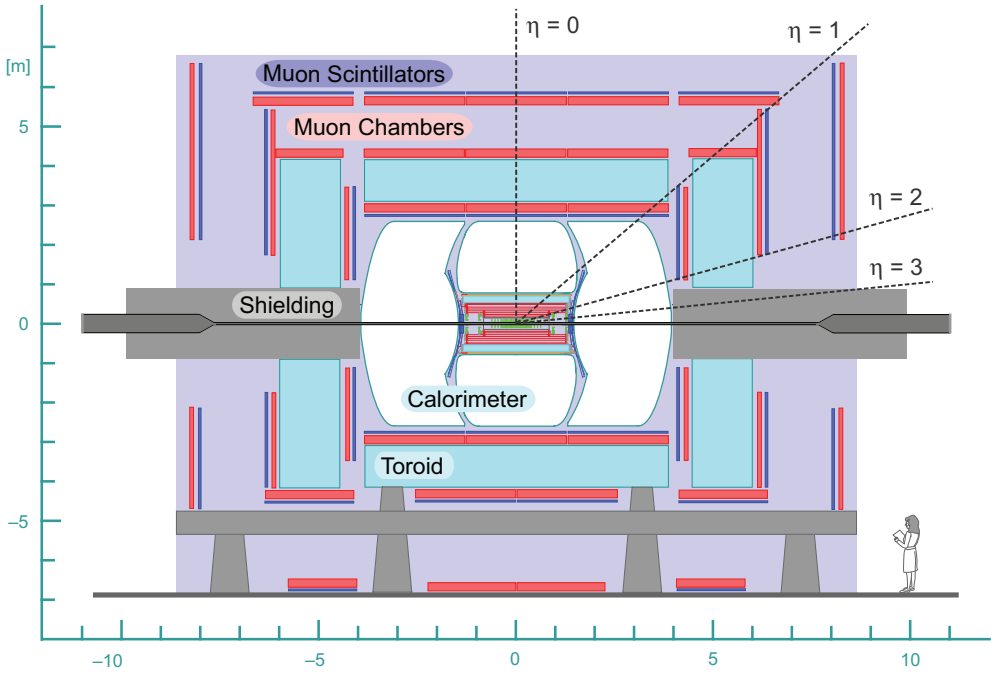

Figure 4.2: Schematic cross section of the DØ detector.

4.2.1 Tracking Detector

The tracking system is important to reconstruct the tracks of charged particles produced in the proton-antiproton interactions. It allows reconstruction of the primary vertex of the collision and also secondary vertices of decaying particles. For any jet measurement, correct primary vertex localization is crucial for the proper energy and momentum determination of jets.

The tracking system consists of two independent systems. The Silicon Microstrip Tracker (SMT) and Central Fiber Tracker (CFT). The SMT consists of 6 barrels, 12 F-disks and 4 H-disks of single or double sided silicon detectors.

The CFT detector consists of scintillating fibers mounted on 8 concentric cylinders. In total it has about 200 km of scintillating and 800 km clear fiber.

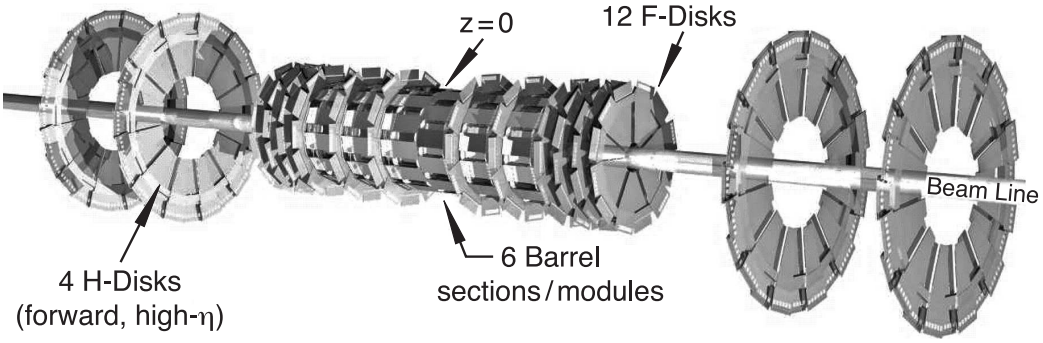

Figure 4.3: Isometric view of the silicon tracking detector.

Working together, both detectors contain more than 850000 channels (SMT 792576, CFT 76800) and are able to locate the primary interaction vertex with a resolution of about 35 μm along the beamline. As the tracking system is located in a magnetic field, the momenta of particles can be measured and thus the electromagnetic calorimeter can be calibrated using the E/p ratio of electrons.

4.2.2 Calorimeter

The calorimeter is the essential subdetector for jet measurements. It is placed so that most particles are stopped and deposit their energies inside it. DØ has a sampling calorimeter which uses liquid argon (LAr) as the ionization medium. The primary absorber material is depleted uranium, with copper and stainless steel used in the outer regions. The whole calorimeter is placed in three individual cryostats – the central cryostat with coverage of pseudorapidities up to ~ 1.0 and two endcaps which extend the whole calorimeter coverage up to ~ 4.0. The area between the central cryostat and the endcaps is instrumented with additional inter-cryostat detector to reduce potential dead space.

Calorimeter cryostats are divided into individual modules. Each module consists of a stack of interleaved absorber plates and signal boards. The absorber plates are separated from the signal boards by the LAr gap (Fig. 4.4). The absorber plates are grounded, while a positive voltage is applied to the resistive coating of the signal boards. Charged particles crossing the gap create a trail of ionization and liberated electrons are collected on the signal board and induce a mirror signal on the copper pad via capacitive coupling.

In order to correctly localize the showers, the modules are divided into smaller units called cells. Radially, the cells form layers in the calorimeter structure. The calorimeter is segmented into inner electromagnetic (EM)

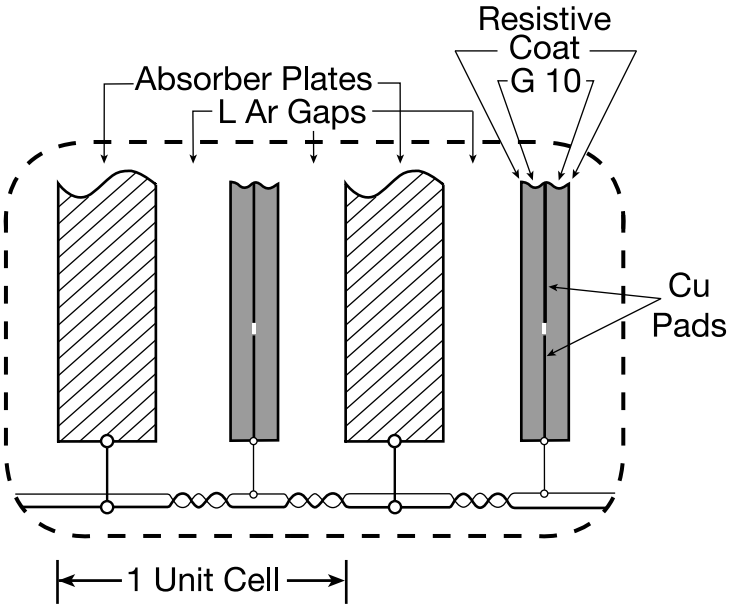

Figure 4.4: Schematic view of an individual calorimeter unit.

layers with depth of about 20 radiation lengths followed by hadronic (HAD) layers of depth of about 7 nuclear interaction lengths which is deep enough to contain about 98% of all the collision energy. The area covered by each cell is roughly 0.1×0.1 in $\eta \times \phi$ space. The exception to this segmentation is the third electromagnetic layer where the segmentation is 0.05×0.05 to better sample the maximum of energy deposition by electrons; and also cells located very forward (high $\eta = -\ln\tan(\theta/2)$), where the size is 0.2 in ϕ and also the η size varies. Cells are positioned in such a way that out of several cells in different layers a pseudoprojective calorimeter tower (i.e. with axis pointing roughly to the center of the detector) can be formed (Fig. 4.5).

4.2.3 Muon System

Particles which deposit only small or almost no energy in the calorimeter are muons and neutrinos. As neutrinos interact only very weakly, their presence is detected only by the energy imbalance seen in the calorimeter. As the initial proton and antiproton do not carry any transverse momentum with respect to the beam, the sum of the final state product transverse momenta must be zero too. Any imbalance is a sign of one (or more) neutrinos in that event. For the detection of muons, a specific detector is situated outside the calorimeter. Where possible by geometrical restrictions, the muon system

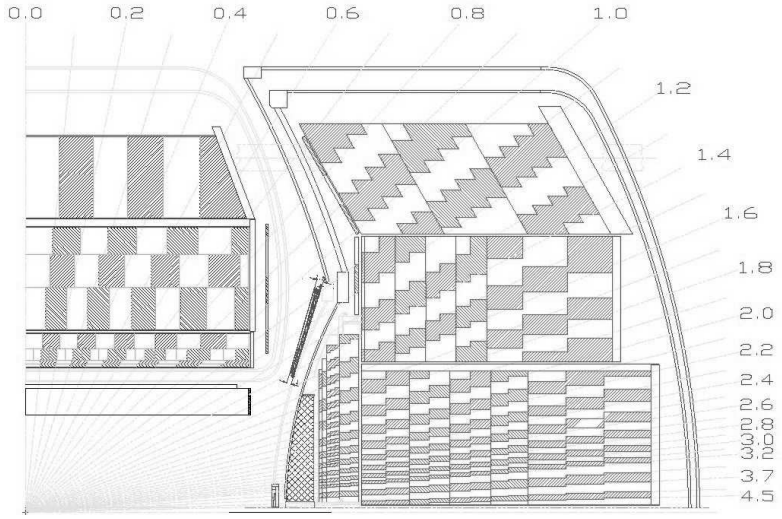

Figure 4.5: The 1/4 side view of the calorimeter showing the pseudoprojective towers.

consists of three layers of detectors within a toroidal magnetic field which allows muon momentum measurement.

For jet measurements, it is important to veto events coming from occasional high energetic cosmic muons passing through the detector which might mimic a fake high energy signal in the calorimeter. These events are not be balanced in the transverse plane, so they can be removed by a cut on missing transverse energy of the event.

4.2.4 Trigger System

The Tevatron operates with 36 bunches of protons and 36 bunches of antiprotons. The time separation between bunches is 396 ns and the frequency of collisions is about 1.7 MHz. It is not possible to record every single collision so a special trigger framework must be used to select only the most interesting collisions.

DØ uses a 3-level trigger system. On each level of the trigger system the number of selected events is significantly reduced while the complexity of the decision algorithms improves. The first level is a hardware-based trigger. It reduces the rate of interesting events to about 10 kHz. Second level is a specific programmable electronics with the rate reduced to 1 kHz. The third level is then a computer farm which selects the events to be saved on tapes with frequency about 50 event per second.

Each individual trigger can be prescaled (separately at each trigger level) by a prescale factor N, so only each N-th event satisfying the trigger condition is kept and therefore the prescale can directly limit the number of saved events.

4.2.5 Luminosity Measurement

In order to measure any cross section in proper units, the luminosity must be determined in order to normalize the data sample.

$$\sigma = \frac{N_{\text{evt}}}{\mathcal{L}} \tag{4.1}$$

The luminosity can be computed also with known structure of the beams[53] generally as

$$\mathcal{L} = f\frac{N_1 N_2}{\pi\sigma_x\sigma y} \tag{4.2}$$

where f is the frequency with which two bunches with N_1 and N_2 particles collide and σ_x and σ_y are transverse beam profiles. However the exact beam parameters are not precisely known at DØ . In order to determine the luminosity, DØ measures the rate of a process with a known cross section (from Eq. 4.1: $\mathcal{L} = N\sigma$). Dedicated subdetector (the luminosity monitor system), consisting of two arrays of 24 plastic scintillators located on both sides at 140 centimeters from the center of the detector, is used to measure the rate of inelastic proton collisions. The total inelastic scattering cross section $\sigma^{p\bar{p}}_{\text{inelastic}}(1.96\,\text{TeV}) = 60.7 \pm 2.4\,\text{mb}$ is corrected for detector acceptance and efficiency. The rate of inelastic collisions is measured by the coincidence of signals from both sides of the luminosity monitor system.

The total integrated luminosity collected during the Run IIa data taking period is $1315 \pm 80\,\text{pb}^{-1}$, the corresponding uncertainty is 6.1%[54]. Part of this sample is used for the three-jet cross section measurement.

4.2.6 Run IIb Upgrade

Particular detector details in this thesis correspond to the configuration for Run IIa, because this was the period when the data used in this thesis were collected. The Run IIb upgrade installed a new layer of silicon detectors (Layer 0) which improved the tracking capability of the experiment. Other significant improvements involved upgraded trigger framework to deal with the increased luminosity anticipated during Run IIb. The computing farm was also upgraded resulting into a larger rate of writing data to tapes of about 100 Hz.

4.3 From the Detector to an Analysis

After the trigger decision is made, the whole detector is read-out and the raw data is stored on tapes using SAM (Sequential Access through Metadata). Computer-intensive reconstruction program `d0reco` is run on a dedicated computer farm in order to reconstruct detector objects (hits in the detectors, tracks, reconstruction algorithms for calorimeter clusters – electrons, jets, photons, muon reconstruction algorithms, etc.). Two output formats can be created. DST (Data Summary Tape) is about $\sim 150\,\mathrm{kB}$/event in size and is no longer centrally produced. The TMB (Thumbnail) format contains most of the interesting information and its size is only $\sim 10\,\mathrm{kB}$/event. TMBs are also produced centrally by the Common Samples (CS) group. The data is divided into independent streams (called skims) which are available to the physics groups. Skims are generally divided according to triggered objects (but more conditions like cuts on energies, etc. are possible) leading for example to single lepton, dilepton skims, or QCD skim. The QCD skim contains all events which fired at least one of jet triggers. In order to streamline the physics analyses, a new framework `cafe` (common analysis format environment) was introduced. `TMBAnalyze` program is run on TMBs to produce CAF (Common Analysis Format) trees (based on the TTree class from ROOT[55], an object-oriented data analysis framework). This format is intended to store only physics objects (electrons, muons, jets, ...) and I/O operations are improved to allow processing large numbers of events in a single computer job. A set of general tools like event selection, efficiencies and corrections are available for all analyzers through the `cafe` framework.

The analysis described later in this thesis uses data collected during the Run IIa data taking period. The raw data was reconstructed using p17 releases of `d0reco` (p17.09.03 and p17.09.03). The CAF trees were produced using p18.05.00 release of `TMBAnalyze`. QCD data skim is used as it contains all jet events recorded by the DØ detector.

5 Jet Energy Scale Calibration

The goal of the jet energy scale calibration is to correct, on average, the jet energy measured in the detector $E_{\text{jet}}^{\text{cal}}$ to the energy of the final state jet on the particle level $E_{\text{jet}}^{\text{ptcl}}$. The master formula reads

$$E_{\text{jet}}^{\text{ptcl}} = \frac{E_{\text{jet}}^{\text{cal}} - O}{R \cdot S} \cdot k_{\text{bias}}\,, \tag{5.1}$$

where O is the offset energy correction which subtracts additional energy not associated with the original proton-antiproton collision (detector noise, pile-up from previous interactions and from multiple interactions within the same bunch crossing in the accelerator). Response R of the calorimeter to leptons and hadrons is usually the largest correction due to the hadronic character of the shower. It is measured using selected data samples. Showering S corrects for particle showering outside the jet cone and for energy which leaked into the jet cone from other showers. k_{bias} corrects additional biases introduced by methods used for estimating O, R and S, such as the physics sample dependence and zero suppression[61] effects of the calorimeter. All corrections are extensively studied for systematic effects and are parameterized in number of additional parameters (primary vertex multiplicity, instantaneous luminosity, detector coordinates and others).

5.1 Offset

The total energy read out by the detector as a result of hard particle scattering can be divided into two parts, soft and hard depending on a (in principle arbitrary) hard scale (e.g. transverse momentum of reconstructed objects with respect to the beam axis).

$$E_{\text{total}} = E_{\text{soft}} + E_{\text{hard}}. \tag{5.2}$$

The hard component E_{hard} is always accompanied with a soft part E_{soft} which has to be subtracted. Several components of the soft energy E_{soft} can be identified. It contains contributions from soft underlying event (proton remnants, E_{UE}), detector noise (either from electronics or from uranium decay) or pile-up (signal not completely readout from the detector coming from the previous bunch crossings) E_{NP} and energy associated with additional inelastic collisions within the same bunch crossing (due to the higher luminosity, the average number of inelastic collisions is larger than one) E_{MI}.

$$E_{\text{soft}} = E_{\text{UE}} + E_{\text{NP}} + E_{\text{MI}} \tag{5.3}$$

Offset energy includes contributions from noise in the calorimeter, pile-up from previous interactions and energy coming from additional (multiple) $p\bar{p}$ interactions in the same bunch crossing. Soft underlying event is considered to be part of the hard process and its energy is not subtracted in the offset since it could be model dependent and the soft underlying event modeling is not well understood.

$$O = E_{\text{NP}} + E_{\text{MI}} \tag{5.4}$$

Noise and pile-up energy (E_{NP}) are estimated using a zero bias trigger. This trigger has no requirement on the detector and triggers only at a time of bunch crossings. With the rate limited by a prescale to about 0.5 Hz, it represents an average energy flow no matter if an inelastic collision occurred or not. In order to eliminate the effects of a possible inelastic collision, a veto on luminosity counter (detectors which are situated at $\eta \sim 2.0 - 4.0$) hits (LMveto) as well as a veto on any primary vertex reconstructed is required (0 vtx). The average energy is measured for η_{det} strips in the calorimeter in bins of instantaneous luminosity (because the amount of pile-up generally depends on luminosity)

$$E_{\text{NP}} = E_{\text{ZB}}(0\,\text{vtx}, \text{LMveto}). \tag{5.5}$$

Each inelastic interaction deposits one unit of underlying energy E_{UE}. The energy is measured using a minimum bias trigger. The only requirement on this trigger is hits coincidence between the north and south luminosity counters. To limit contributions from additional collisions, events are required to have exactly one primary vertex. The underlying event energy is then the average energy in such event minus the contribution of noise and pile up

$$E_{\text{UE}} = E_{\text{MB}}(1\,\text{vtx}) - E_{\text{NP}}. \tag{5.6}$$

The energy of additional interactions is parameterized in the number of reconstructed primary vertices in the minimum bias events

$$E_{\text{MI}}(n) = E_{\text{MB}}(n + 1\,\text{vtx}) - E_{\text{MB}}(1\,\text{vtx}). \tag{5.7}$$

Both E_{UE} and E_{MI} are again measured in bins of instantaneous luminosity ($E_{\mathrm{NP}} = E_{\mathrm{NP}}(\mathcal{L}), E_{\mathrm{UE}} = E_{\mathrm{UE}}(\mathcal{L}), E_{\mathrm{MI}} = E_{\mathrm{MI}}(\mathcal{L})$). The average offset energy is then parameterized in the number of primary vertices and the instantaneous luminosity. The offset is computed by summing the average offset energy in the jet cone and is therefore a function of the jet η_{det} and cone size (R_{cone}). Individual shapes of the jets are not taken into account.

The offset energy is measured using large zero bias and minimum bias samples which leads to very small statistical uncertainties. Due to the parameterization in number of primary vertices and instantaneous luminosity, the potential systematic effects are also limited. The time dependence of the offset energy is checked and a conservative 5% systematic error is assigned. Potentially large systematical effects due to zero suppression in the calorimeter, which can be different in minimum bias and jet events, is treated in the k_{bias} correction.

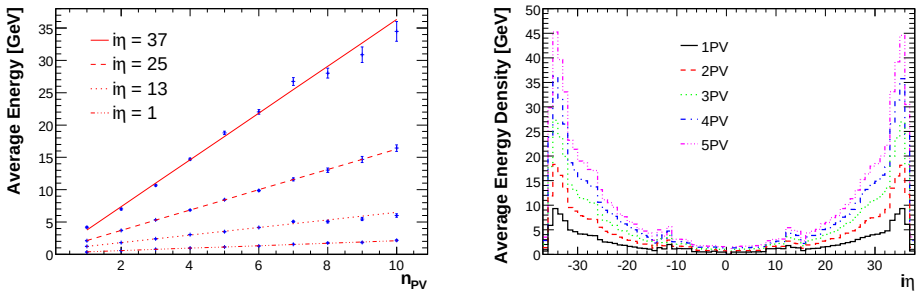

Figure 5.1: An average energy in minimum bias events as a function of primary vertex multiplicity for different $i\eta$ strips (left) and average energy density as a function of $i\eta$ for different primary vertex multiplicities (right).

5.2 Response

The response of the calorimeter to particles is generally smaller than one – the energy measured by the detector is somewhat lower due to various detector effects. The Missing E_T Projection Fraction (MPF) method can be used to measure the relative response of two objects in the detector. At the particle level (before the detector), the transverse momenta of one (tag) object $p_{T\,\mathrm{tag}}$ and the second (recoil) $p_{T\,\mathrm{recoil}}$ are balanced

$$\vec{p_{T}}_{\mathrm{tag}} + \vec{p_{T}}_{\mathrm{recoil}} = 0 \tag{5.8}$$

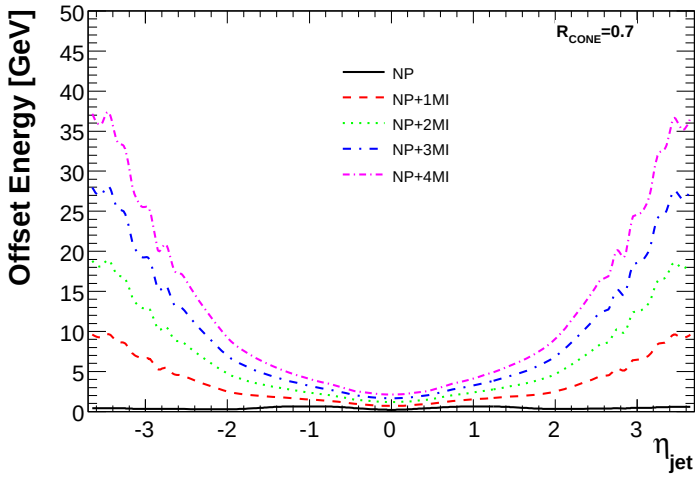

Figure 5.2: Estimated jet offset energy for jets with $R_{\text{cone}} = 0.7$.

The measured p_T will be affected by the response $\vec{p_T}^{\text{meas}} = R\vec{p_T}$ and the tag and recoil transverse momenta will not be balanced due to detector effects (resulting in a non-zero missing transverse energy $\not\!\!E_T$). This leads to the modification of Eq. 5.8 to

$$\vec{p_T}^{\text{meas}}_{\text{tag}} + \vec{p_T}^{\text{meas}}_{\text{recoil}} = -\not\!\!E_T, \tag{5.9}$$

from which the following expression can be derived

$$\frac{R_{\text{recoil}}}{R_{\text{tag}}} = 1 + \frac{\vec{\not\!\!E}_T \cdot \vec{n}_{T\text{tag}}}{p_T{}^{\text{meas}}_{\text{tag}}} \tag{5.10}$$

and the relative response of tag and recoil objects can be determined. If the absolute response for the tag object is known, the absolute response of the recoil can be then also determined.

The DØ experiment uses the following method to determine the jet response. First, the electromagnetic part of the calorimeter (inner layers) is calibrated using $Z \to e^+e^-$ events. The response to electrons and photons is almost the same. The difference (due to amount of material in front of the calorimeter which can lead to photon conversion) was determined using a Monte Carlo study and is taken into account. Then the response to hadrons is estimated using a sample of $\gamma +$jet events. The experiment collected a relatively large sample of clean events with a photon and jet reconstructed. In these events, the calibrated photon serves as a tag object. Additional criteria

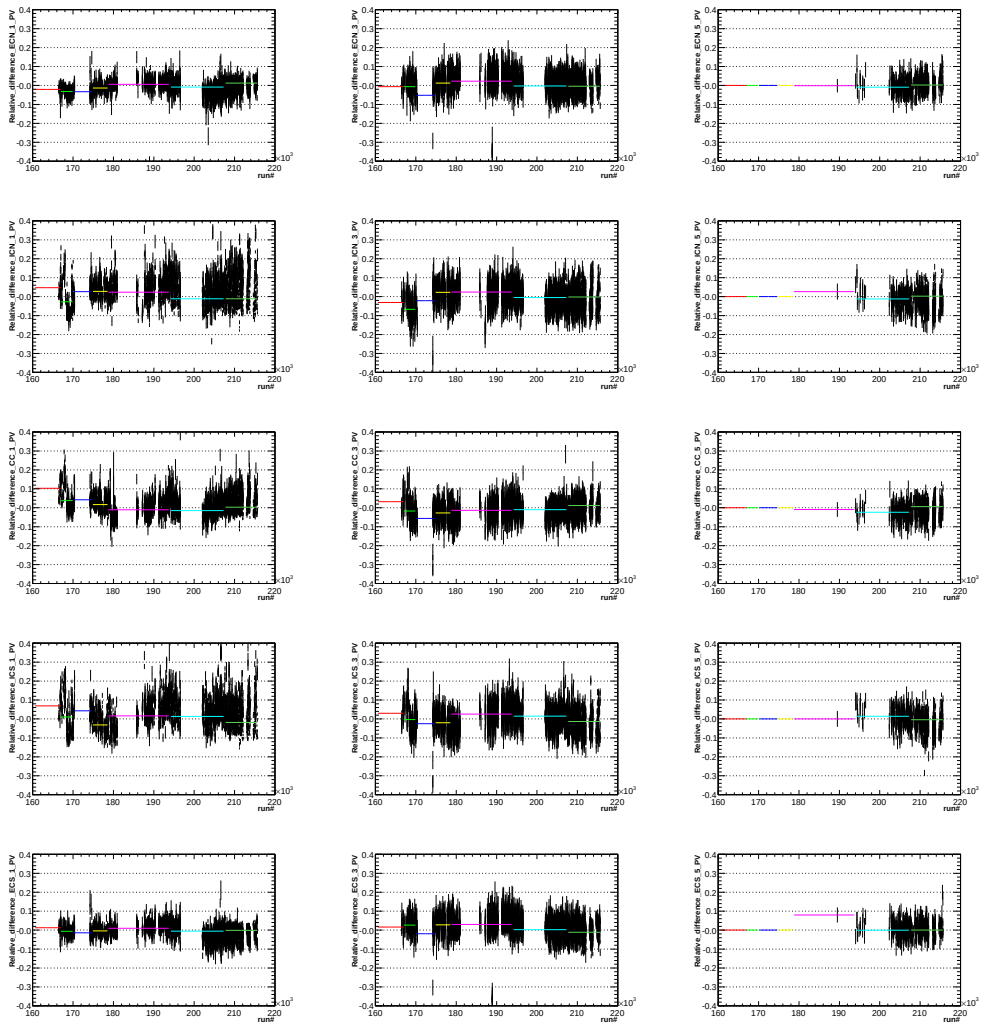

Figure 5.3: Time dependence of the average energy measured in 5 regions of the calorimeter. Calorimeter regions (rows) correspond to the following values of $i\eta$: ECN ($-37 \leq i\eta < -16$), ICN ($-16 \leq i\eta < -8$), CC ($-8 \leq i\eta \leq 8$), ICS ($8 < i\eta \leq 16$) and ECS ($16 < i\eta \leq 37$). Three columns correspond to primary vertex multiplicities of 1, 3 and 5. The horizontal axis corresponds to run number, showing that only later runs had luminosity high enough to produce higher number of multiple interactions. Color horizontal bars show the average calorimeter energies over different run periods.

on the event selection enable to use the jet as the recoil object. Exactly one primary vertex in the interaction is required, the photon candidate has to satisfy certain identification criteria and must be in the central calorimeter ($|y^{\gamma}_{\rm det}| < 1.0$, due to the coverage of electromagnetic calorimeter). In reality, the recoil can be a more complex object than a single jet. For the jet response, exactly one reconstructed jet is required in the central part of the calorimeter ($|y^{\rm jet}_{\rm det}| < 0.4$) and photon and jet are required to be back-to-back in the $r-\phi$ plane. The angle $\phi(\gamma, {\rm jet})$ is required to be larger than 3.0. (Note that the detector coordinates $y_{\rm det}$ or $\eta_{\rm det}$ are calculated with respect to the geometrical center of the detector and not to the primary vertex as is the case of physics y or η).

Poor jet energy resolution introduces a bias in the response determination. To minimize the effect, an energy estimator E' is used instead of binning the response in the poorly measured $E_{\rm jet}$

$$E' = p_{T_\gamma}^{\rm meas} \cosh(\eta_{\rm jet}). \tag{5.11}$$

The transverse momentum of the photon and jet angle are variables which are measured more precisely than the jet energy. The energy dependence of the response is well described by a quadratic logarithmic function:

$$R(E') = p_0 + p_1 \log(E'/E_0) + p_2 \log^2(E'/E_0), \tag{5.12}$$

where $E_0 = 100$GeV and p_i are free parameters to be determined. It should be noted that extrapolating this fit to higher energies would give a energy scale uncertainty larger than 2%, so a special procedure was carried out for $R_{\rm cone} = 0.7$ jets. The single pion response was parameterized, rather than the jet response directly. The parameters of single pion response were fitted by comparing the Monte Carlo predictions of jet response with the data. This procedure resulted in a 0.5% error on the high energy jet response and an additional 0.8% systematics due to uncertainties in the Monte Carlo modeling of jet fragmentation, which is still smaller than what the uncertainty would be in case of direct extrapolation of the response.

In the next step, the response is calibrated in η with respect to the central calorimeter ($R_{\rm CC}$).

$$R(\eta) = \mathcal{F}_\eta R_{\rm CC}. \tag{5.13}$$

A mixture of $\gamma +$ jet and dijet events is used to extend the measurement of the response to forward parts of the calorimeter. The mixed sample improves the statistical precision as well as extends the energy reach compared to what the $\gamma +$ jet sample can reach. In dijet events, the central (already calibrated jet) is balanced by a second jet in the forward calorimeter, response of which can be determined.

The estimated response for the data and Monte Carlo simulation is shown in Fig. 5.4 and fit parameters for Eq. 5.12 are shown in Table 5.1.

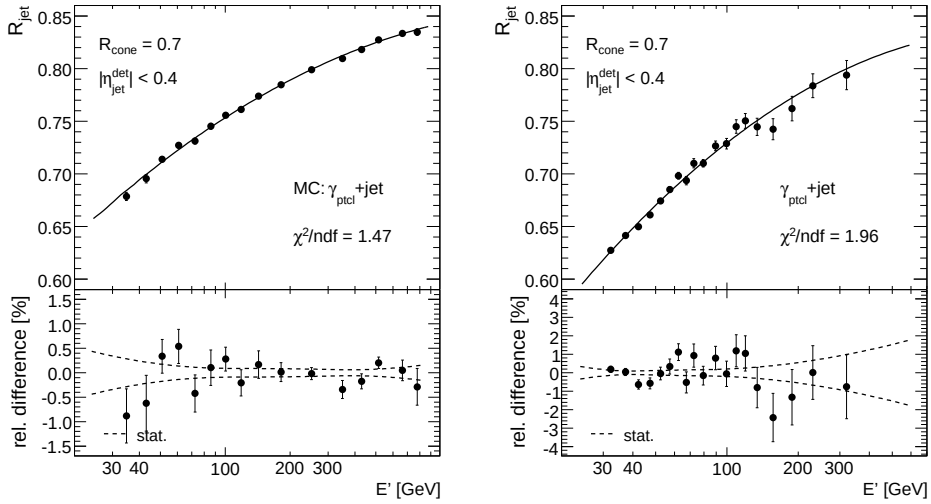

Figure 5.4: The absolute MPF response for $R_{\text{cone}} = 0.7$ jets in MC (left) and data (right) as a function of the energy estimator E' in the central part of the calorimeter.

Type	p_0	p_1	p_2
MC	0.75336 ± 0.00068	0.05688 ± 0.00106	-0.00781 ± 0.00070
data	0.7294 ± 0.0015	0.0761 ± 0.0033	-0.0134 ± 0.0027

Table 5.1: Fitted parameters for the MPF response energy dependence for $R_{\text{cone}} = 0.7$ jets.

The response suffers from the zero suppression effect in the calorimeter in a similar way as offset. The bias is thus merged into a single correction factor $k_{\text{bias}} = k_O/k_R$ and the two effects almost cancel. An example of this cancellation is shown in Fig. 5.6.

5.3 Showering

Showering corrects for energy of particles entering and leaving the jet cone due to the detector effects (like bending of particles in a magnetic field, detector segmentation, etc.) and for energy flow in and out of the jet cone due to shower development in the calorimeter.

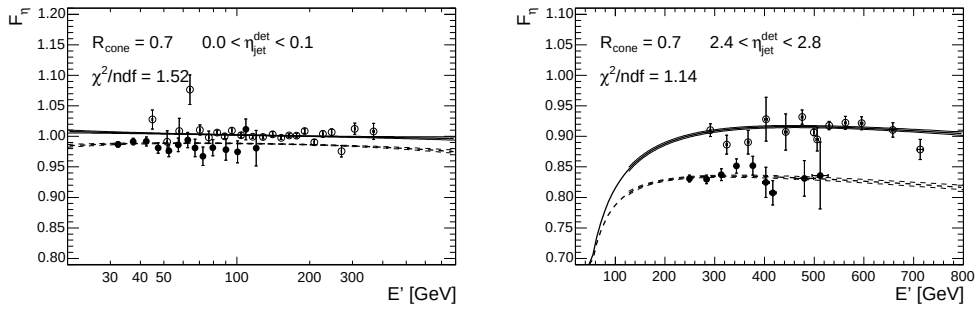

Figure 5.5: η dependent correction to the response for $R_{\rm cone} = 0.7$ jet in data as a function of E' and for two different $\eta_{\rm det}$ bins. The solid (open) circles represent the measurements in the γ + jet (dijet) sample.

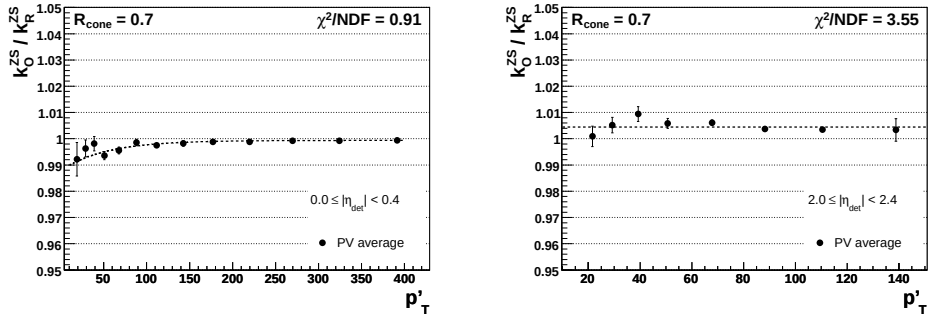

Figure 5.6: Example of an approximate cancellation of the zero suppression effects in offset and response determination in two different η bins.

The effect has been studied in Monte Carlo and compared to data. In fully simulated events, the energy of each particle can be tracked and templates characterizing the energy distribution around jets can be estimated. From this average energy template, offset contribution can be subtracted and the remaining profile is fitted to energy profiles from data in order to estimate the showering correction.

An example of the energy profile in γ + jet Monte Carlo simulation is shown in Fig. 5.7. Selected events are required to have a matched jet between the particle and detector levels, so all particles energies corresponding to the detector jet can be tracked. Two templates are measured, the *jet template* corresponding to energies of particles from the jet and the *not-jet template* for the remaining particles in the event. Particle jet energy deposited far away from the detector jet center corresponds to low momentum particles heavily bent in the magnetic field, while the bump of the energy not coming

from the particle jet at $\Delta R \gtrsim 3$ corresponds to the photon energy.

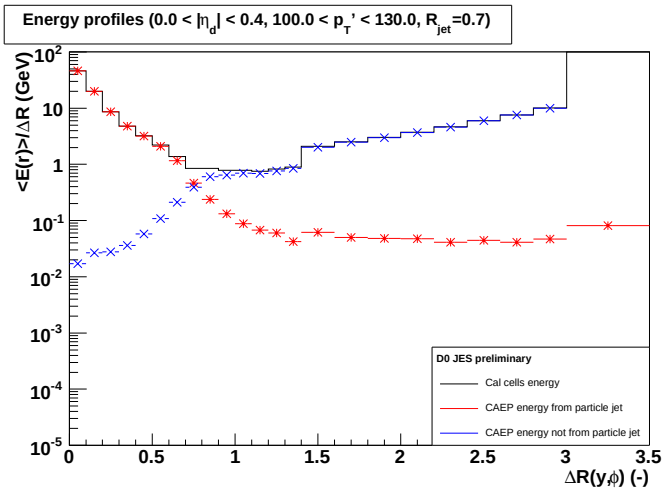

Figure 5.7: An example of the energy distribution as a function of radial distance from the jet center in Monte Carlo simulation of $\gamma+$jet events. The red histogram shows the energy deposited by particle jet, the blue histogram the remaining energy in the event (the bump at ΔR corresponds to the photon).

The true offset contribution is measured in the Monte Carlo using samples with and without the zero bias data overlay. The combination of jet, not-jet and offset templates is fitted to data, keeping the offset contribution fixed while allowing the scale of jet and not-jet templates to vary:

$$E^{\text{fit}}(r) = \alpha E^{\text{jet}}(r) + \beta E^{\text{not-jet}}(r) - E^{\text{offset}}(r). \tag{5.14}$$

The showering correction is defined as a ratio of the raw jet energy $E_{\text{jet}}^{\text{raw}}$ to the true jet energy estimated from the templates $E_{\text{jet}}^{\text{true}}$

$$S_{\text{template}} = \frac{E_{\text{jet}}^{\text{raw}}}{E_{\text{jet}}^{\text{true}}}, \tag{5.15}$$

where the raw jet energy

$$E_{\text{jet}}^{\text{true}} = \int_{r=0}^{r=R_{\text{cone}}} (E^{\text{det}} - E^{\text{offset}})\mathrm{d}r = \int_{r=0}^{r=R_{\text{cone}}} (\alpha E^{\text{jet}} + \beta E^{\text{not-jet}})\mathrm{d}r \tag{5.16}$$

and the true jet energy

$$E_{\text{jet}}^{\text{true}} = \int_{r=0}^{r=\text{inf}} \alpha E^{\text{jet}}\mathrm{d}r. \tag{5.17}$$

The showering correction is presented in Fig. 5.8.

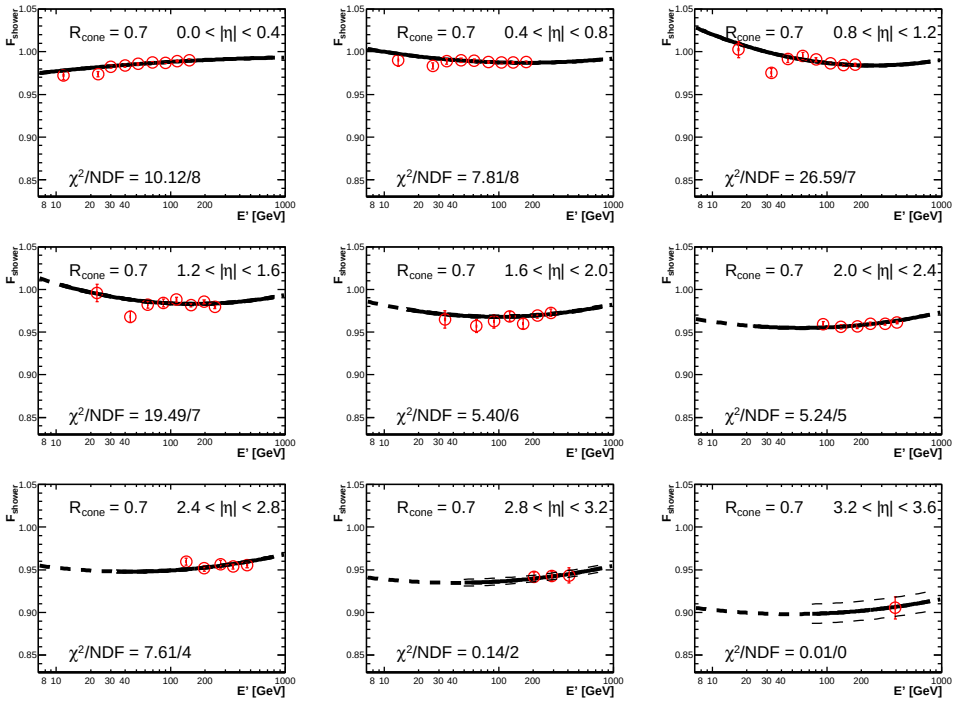

Figure 5.8: The showering correction for $R_{\text{cone}} = 0.7$ jets in data in different $\eta_{\text{jet}}^{\text{det}}$ bins.

5.4 Jet Energy Scale Uncertainty and Closure Tests

Closure tests are designed to show the validity of the jet energy scale correction within the assigned uncertainty. In Monte Carlo, where particle level jet energy is available, the direct closure variable

$$\mathcal{D} = \frac{\langle E_{\text{jet}}^{\text{corr}} \rangle}{\langle E_{\text{jet}}^{\text{ptcl}} \rangle}, \tag{5.18}$$

relates the calibrated reconstructed jet energy to the particle jet level and the level of agreement is shown in Fig. 5.9.

Since the particle level jet energy is not available in data, the closure test in data lies in the relative comparison between corrected jets in data and in Monte Carlo in a γ + jet sample. The relative closure together with the uncertainty is shown in Fig. 5.10.

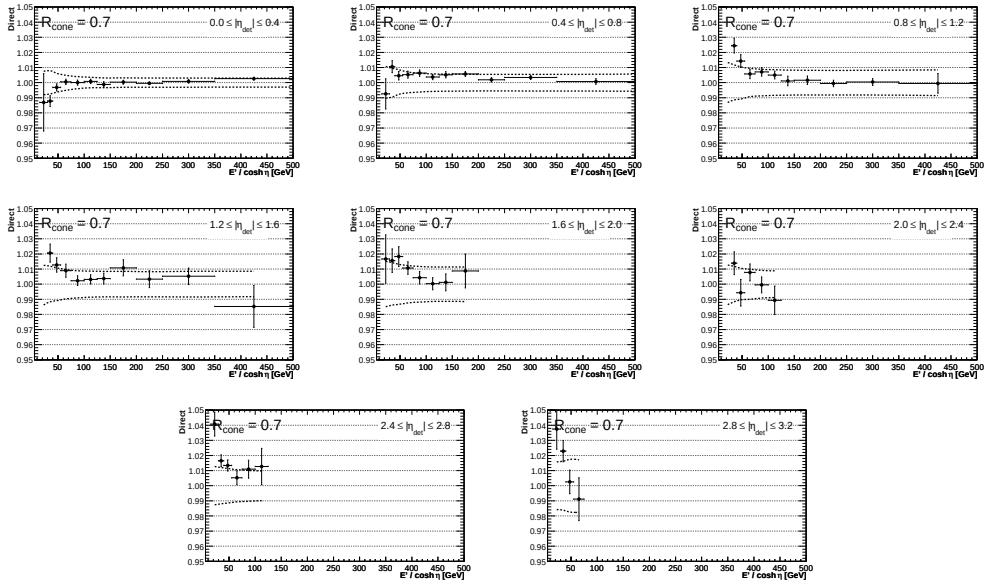

Figure 5.9: Direct closure test in Monte Carlo simulation for $R_{\mathrm{cone}} = 0.7$ jets in different $\eta_{\mathrm{jet}}^{\mathrm{det}}$ bins with dashed lines representing the total jet energy scale correction uncertainty.

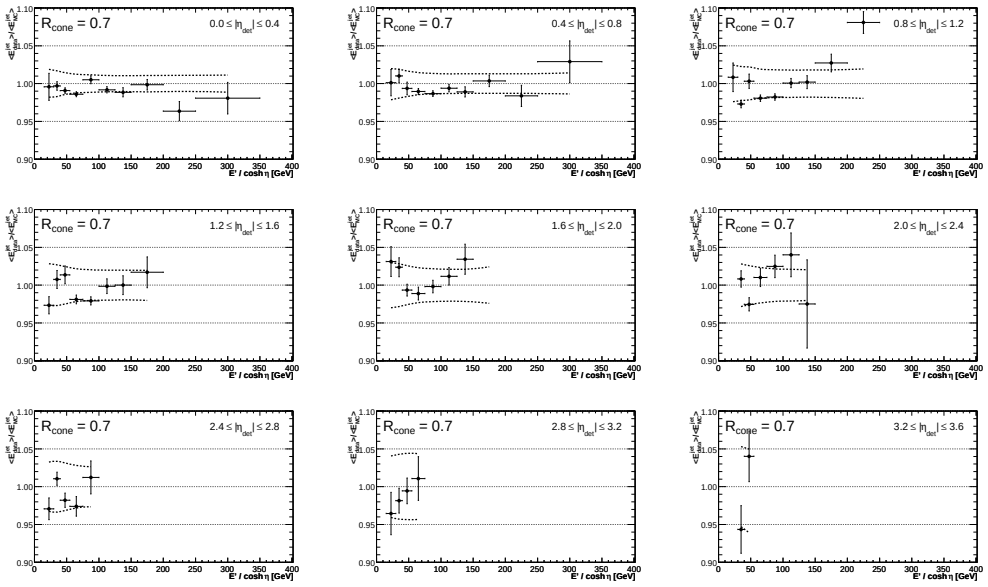

Figure 5.10: Relative data-to-MC closure test for $R_{\mathrm{cone}} = 0.7$ jets in different $\eta_{\mathrm{jet}}^{\mathrm{det}}$ bins. The dashed line represents the total jet energy scale uncertainty.

5.5 Dijet Jet Energy Scale

The correction factors and the unprecedented uncertainty (on the level of 1–2% in most of the kinematic range) presented in Figs 5.12 and 5.13 are strictly speaking valid only for the γ + jet sample. Additional corrections are needed to estimate the potential of physics bias. Dijet jet energy scale (denoted also as jet four-vector scale, J4S) was derived specifically for the QCD group using dijet sample[24]. Most of the individual subcorrections were redetermined using the dijet sample. The validity was tested on the inclusive jet sample [24] and separately on the three-jet inclusive sample used in this thesis (see Sec. 6.6).

The basic difference is coming from the different quark-gluon content in the γ + jet sample and QCD (inclusive jets) samples. At low energies, the dijet sample is dominated by gluon jets, opposite to the γ + jet. At high energies, the situation is opposite; the dijet sample is dominated by quark jets and γ + jet sample by gluon jets. The derived response for jets in γ + jet and gluon samples is shown for comparison in Fig. 5.11.

The correction factors and uncertainties for the J4S are presented in Figs 5.14 and 5.15.

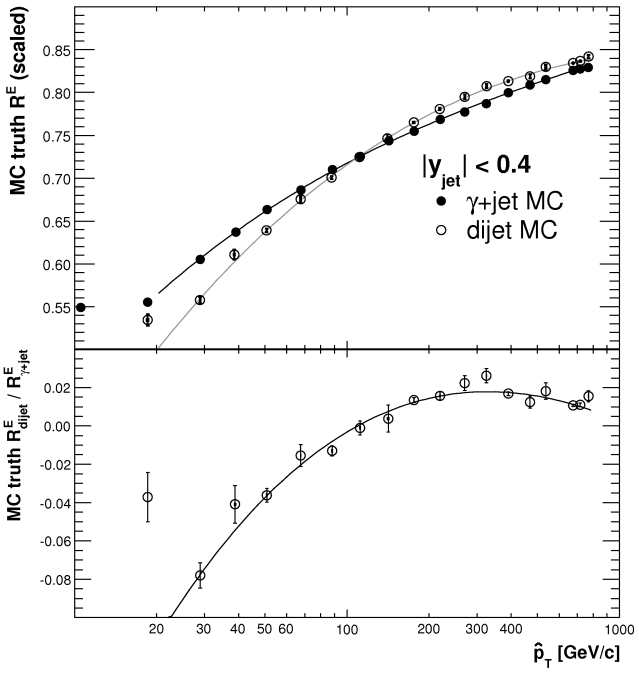

Figure 5.11: Difference in response for jets from γ + jet dijet samples using Monte Carlo with tuned single pion response.

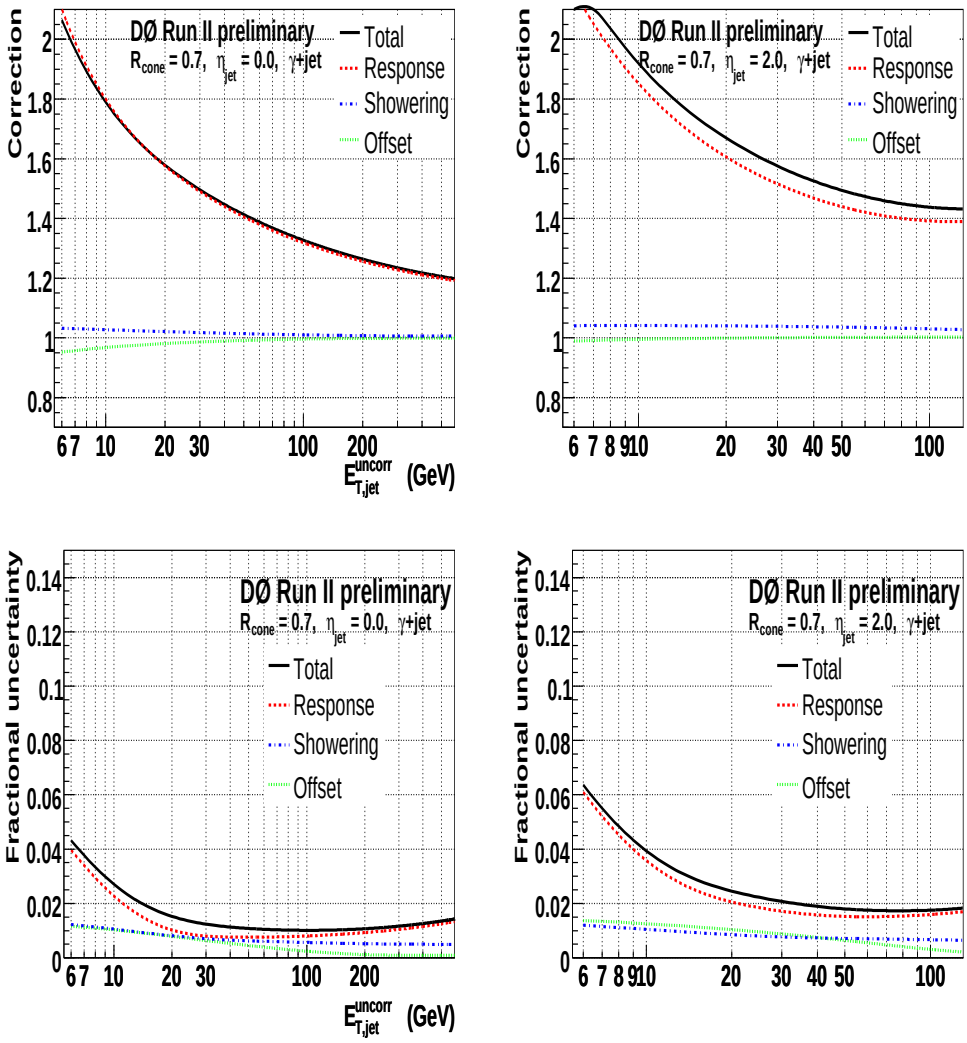

Figure 5.12: Jet Energy Scale correction factor (top row) and uncertainty (bottom row) as a function of the jet transverse momentum in central (left) and forward (right) part of the detector.

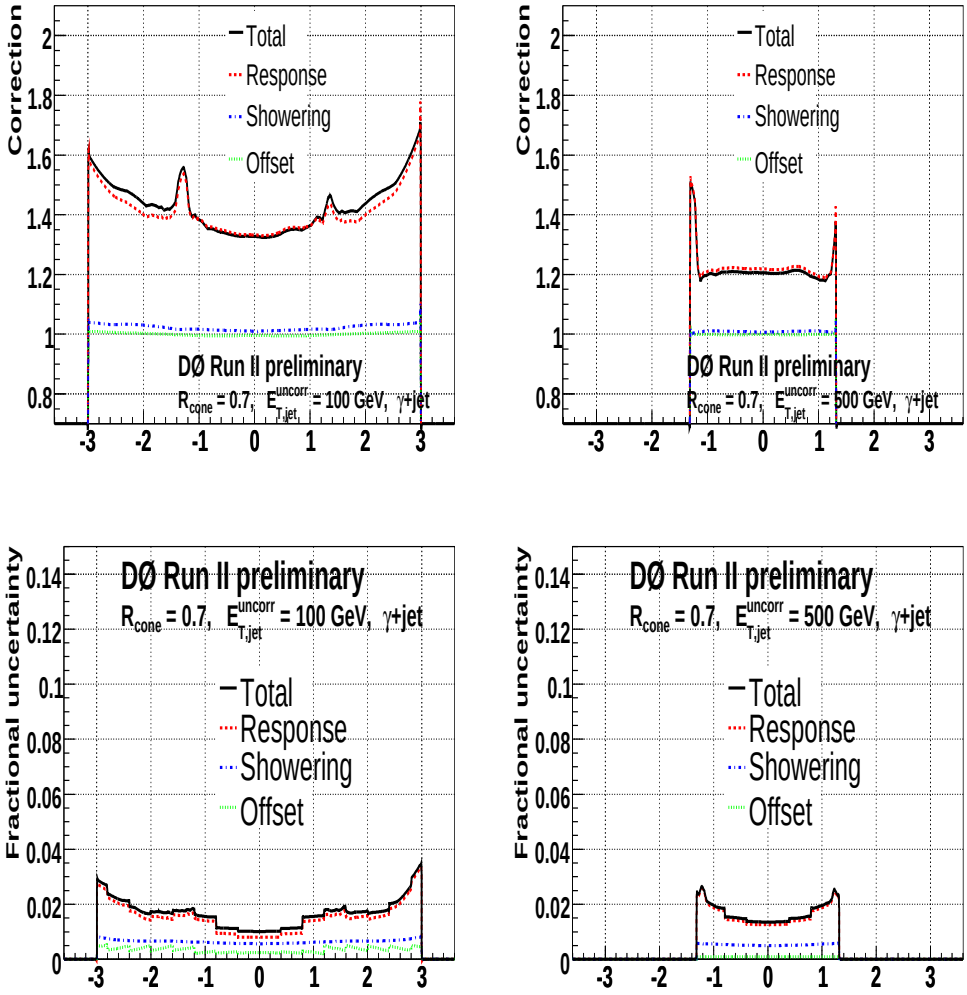

Figure 5.13: Jet Energy Scale correction factor (top row) and uncertainty (bottom row) for $E_T = 100,\mathrm{GeV}$ jet (left) and $E_T = 500\,\mathrm{GeV}$ jet (right).

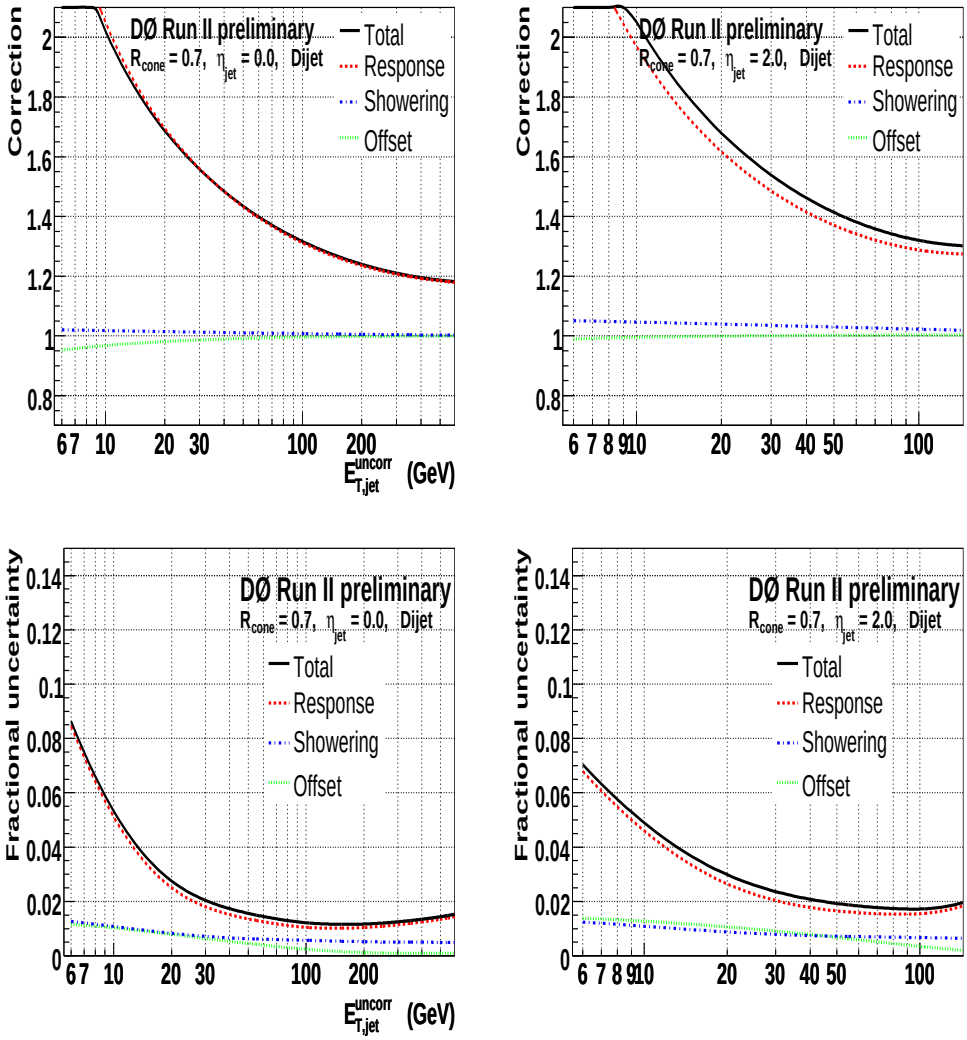

Figure 5.14: Dijet Energy Scale correction factor (top row) and uncertainty (bottom row) as a function of the jet transverse momentum in central (left) and forward (right) part of the detector.

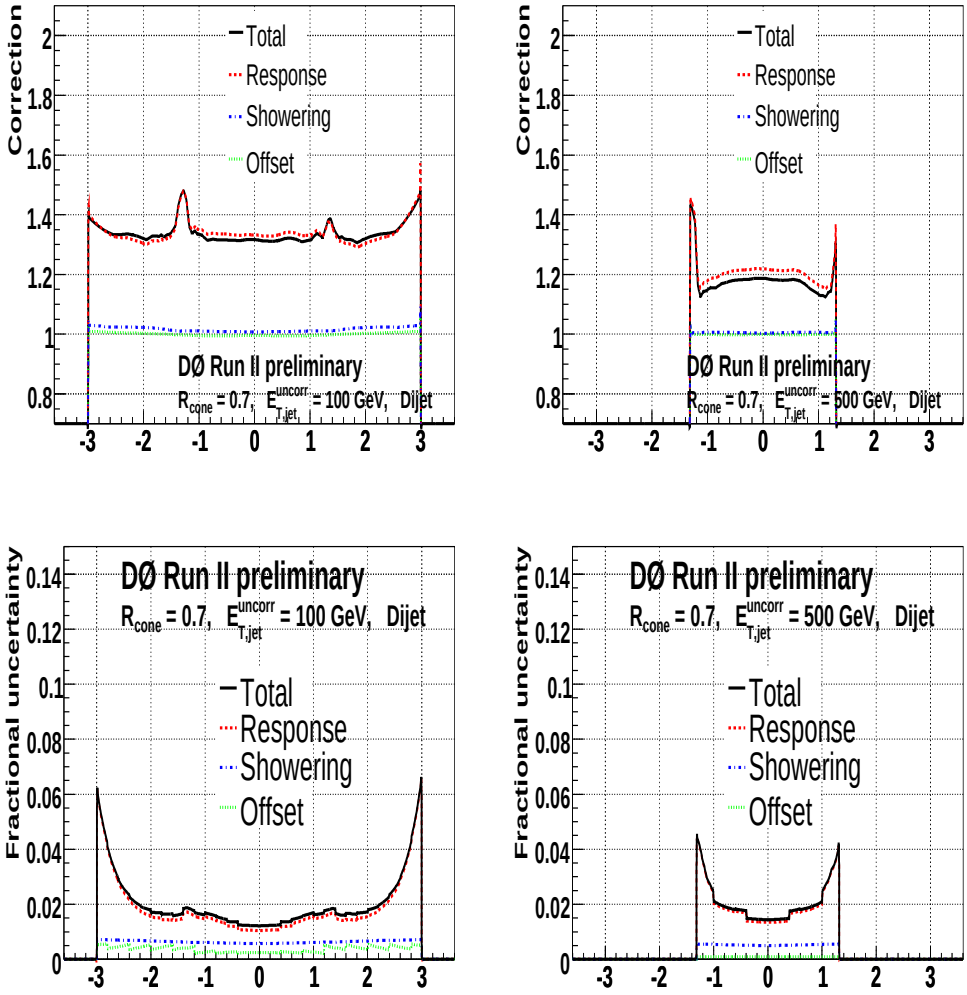

Figure 5.15: Dijet Energy Scale correction factor for $E_T = 100\,\text{GeV}$ jet (left) and $E_T = 500\,\text{GeV}$ jet (right).

6 Three-jet Final State

6.1 Introduction and Motivation

Jet production has one of the highest cross sections of any processes in high energy hadron-hadron collisions. Quantum chromodynamics describes the scattering of quarks and gluons and provides a possible explanation for jet production. In the perturbative picture, in the simplest case of lowest order, two jets are produced — for example, in the s-channel, a quark and an anti-quark annihilate into a gluon which then splits into another quark-antiquark pair. This pair will then form a pair of jets. Additional quarks or gluons can be radiated at higher orders, leading to three or more jets in the final state.

Properties of the three-jet final state will be investigated in this measurement. The three-jet cross section measurement is a stringent test of NLO QCD similar to the inclusive jet and dijet cross section measurements. The three-jet final state is more complicated and therefore more difficult as more variables can be studied.

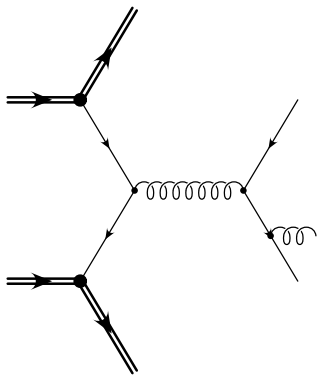

Figure 6.1: Example of "Feynman"-like diagram showing the three jet production.

6.2 Three-jet System

The three-jet system requires several variables to completely describe the observed final state. There are 3 four-vectors giving 12 variables in total. The choice is somewhat arbitrary, one can use the energies and momenta of the three jets but a more physically motivated set is used. One can decompose the system of coordinates in the following way. First, the beams at the Tevatron are not polarized, therefore there is an overall angle which can be integrated over (ϕ symmetry). Then the three-jet system is described in its center of mass (CMS) coordinate system. There are three variables which describe the Lorentz boost to the CMS. The center of mass system of the interacting partons is usually boosted (mostly along the original beam direction as the partons inside proton have negligible transverse momenta with respect to the proton) with respect to the center of mass of the proton-antiproton system.

In the CMS, 8 variables remain. The most commonly used variables are that of the standard convention by [62], which has a property that it can be directly generalized to higher jet multiplicities. The numbering convention of [62] is to label the initial partons as 1 and 2. Then the three final state partons are numbered 3, 4 and 5 according to their energy in their center of mass system (with 3 being the leading one, 4 the subleading, ...).

First on the list of the 8 remaining variables, there is the mass of the three-jet system $M_{3\text{jet}}$ which characterizes the total energy of the system. In the three-jet CMS, it can be computed directly as

$$M_{3\text{jet}} = E_3 + E_4 + E_5. \tag{6.1}$$

It can be also thought as the amount of the total proton-antiproton collision energy carried away by the three-jet system (the rest taken away by softer jets and proton-antiproton remnants).

Then the energy distribution is described by the X_3 and X_4 (sometimes called Dalitz) variables. In the CMS system, they are defined as

$$X_3 = \frac{2E_3}{M_{3\text{jet}}}, \tag{6.2}$$

$$X_4 = \frac{2E_4}{M_{3\text{jet}}}. \tag{6.3}$$

One can also define the X_5 variable in the same way, but one can directly see that it is not an independent variable because of the simple $X_3 + X_4 + X_5 = 2$ relation between them. In the case of massless partons (jets) the allowed ranges are $2/3 \leq X_3 \leq 1$ and $1/2 \leq X_4 \leq 2/3$. However, this is not true

in the case of massive jets where X_3 might be larger than 1 and still the conservation laws can be satisfied. An example cartoon of the allowed phase space and typical three-jet configurations are shown in Fig. 6.2.

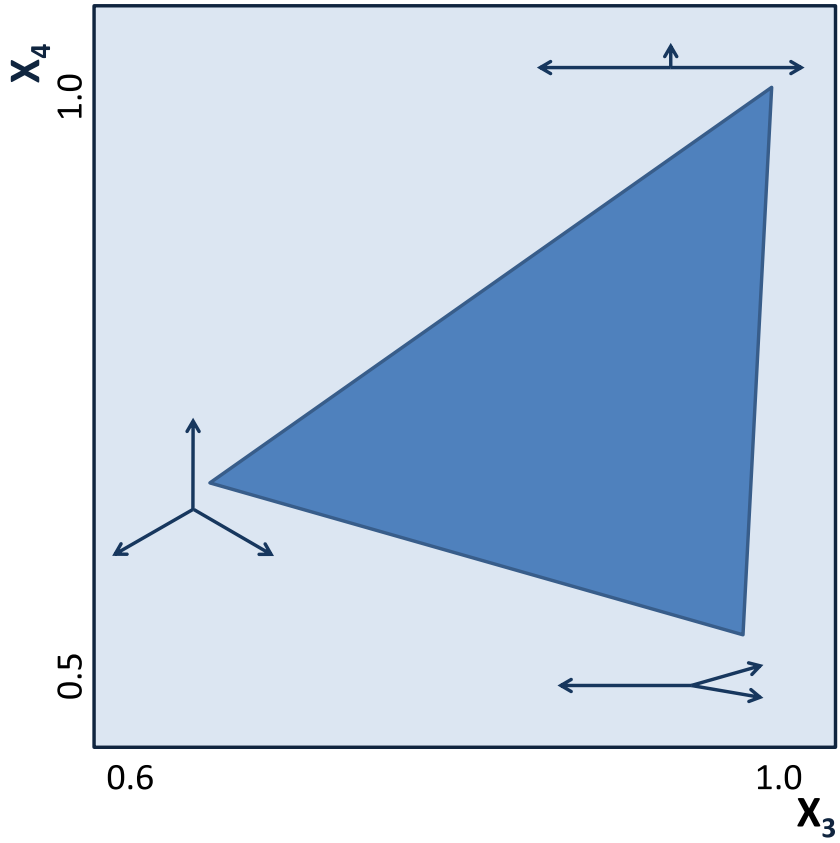

Figure 6.2: A cartoon showing a typical allowed phase space (depends on an analysis cuts) for X_3 and X_4 variables. Three arrows in corners of the phase space show typical configuration of the jets in that region. With $X_3 \to 1$ and $X_4 \to 0.5$ the leading jet is balanced by two jets with similar energies. When $X_3 \to 1$ and $X_4 \to 1$ only the small remaining energy is left for the third jet which will look like a small radiation to a balanced dijet system. When $X_3 \to 2/3$ and $X_4 \to 2/3$ then all three jets carry the same energies and the configuration could look like the "Mercedes" sign (see Appendix C for an example of a real event display).

There are two angles which help with the description of the system. The cosine of an angle θ^* between the parton 3 and the beam direction and ψ_3, the angle between two planes, one formed by the beam direction and the parton 3, the second by the partons 4 and 5. If one defines the (average)

beam direction as

$$\vec{p}_{\rm AV} = \vec{p}_1 - \vec{p}_2 \tag{6.4}$$

then the angles are

$$\cos\theta^* = \frac{\vec{p}_{\rm AV}\cdot\vec{p}_3}{|\vec{p}_{\rm AV}||\vec{p}_3|}, \tag{6.5}$$

$$\cos\psi_3 = \frac{(\vec{p}_3\times\vec{p}_{\rm AV})\cdot(\vec{p}_4\times\vec{p}_5)}{|\vec{p}_3\times\vec{p}_{\rm AV}|\cdot|\vec{p}_4\times\vec{p}_5|}. \tag{6.6}$$

$\cos\theta^*$ has the same role as in in the Rutherford scattering.

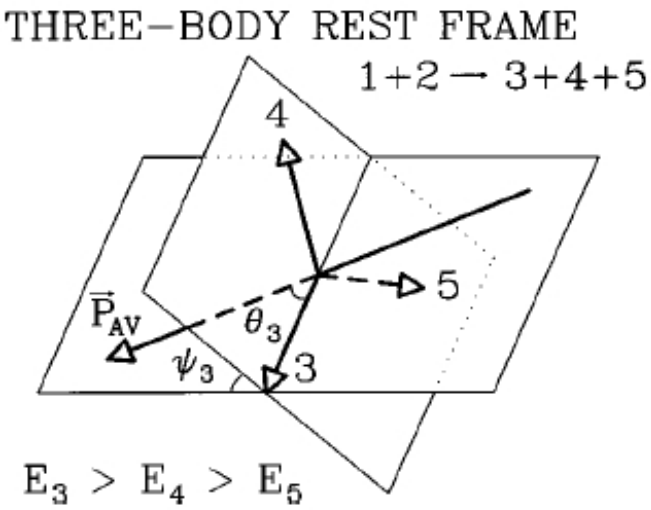

Figure 6.3: Definition of three-jet angles (taken from [62]).

The remaining variables describe the distribution of mass in the three-jet system. In the case of massless partons or jets these are not variables but rather constraints which reduce the number of required variables. It is convenient to define the mass variables as dimensionless.

$$f_3 = \frac{m_3}{M_{\rm 3jet}}, \tag{6.7}$$

$$f_4 = \frac{m_4}{M_{\rm 3jet}}, \tag{6.8}$$

$$f_5 = \frac{m_5}{M_{\rm 3jet}}. \tag{6.9}$$

The three-jet system is then completely described in its CMS by ($M_{3\text{jet}}$, X_3, X_4, $\cos\theta^*$, ψ, $f_3.f_4, f_5$).

The jet numbering convention in this thesis will label the leading jet transverse momentum as p_{T1}, the second leading jet rapidity y_2 and the third leading jet azimuthal angle ϕ_3.

6.3 Analysis Bin Selection

This thesis describes the measurement of the differential inclusive three-jet cross section as a function of the three-jet invariant mass[63] (similar to the dijet mass) in different regions of jet rapidities and jet transverse momentum. The three-jet mass measures the total production rate of three jets while other variables can describe the inner structure of the three-jet system.

The following rapidity regions were chosen for the measurement of the dependence of the cross section on jet rapidity: the selected three-jets are required to be either in the central calorimeter only (named CC, $|y_{\text{jet}}| < 0.8$), up to the intercryostat region (named IC, $|y_{\text{jet}}| < 1.6$) or up to the endcap calorimeter (named EC, $|y_{\text{jet}}| < 2.4$). The regions are defined inclusively, EC region contains events from CC and IC regions. The rapidity requirement applies to all three leading jets. The transverse momentum requirement is set to 40 GeV of the softest (third jet) to study only hard jets with good transverse momentum resolution and limit the uncertainty from the jet energy scale.

For the measurement of the cross section dependence on the jet transverse momentum, the widest rapidity region (EC, $|y_{\text{jet}}| < 2.4$) is used. The regions of transverse momentum studied are $p_{T3} > 40, 70, 100\,\text{GeV}$, the analysis regions are labeled 40, 70 and 100 for simplicity. Again, the binning is inclusive, the 100 region is a subsample of 70 region, etc. The region selection is based on jet transverse momentum resolution (lowest p_T region) and overall event statistics (highest p_T region).

6.4 Data Selection

The measurement uses the Run IIa QCD dataset collected by the DØ experiment between 2002 and 2006. The integrated luminosity is about $1\,\text{fb}^{-1}$. The dataset is reduced to the run range 191000–213064 where the jet energy scale (JES) and dijet jet energy scale (J4S) were measured. Older data is removed because of instabilities in the ICR detector. Newer data is not used because the JES/J4S corrections are not yet available. The integrated luminosity of

the selected dataset is about $0.7\,\mathrm{fb}^{-1}$ for the JT_125TT trigger (Tab. 6.1). The analysis uses the p17.09.03, p17.09.06 and p17.09.06b datasets, converted to CAF files using the p18.05.00 release. The data is then corrected using the inclusive jet energy scale (J4S version **jetcorr** v07-02-78). The data quality is checked using **dq_defs** version v2007-10-10 which removes bad events using data quality information from all subdetectors and also from calorimeter quality flags. The luminosity is determined using v2007-10-10 **dq_defs** using the common tools.

6.5 Event Selection

Events are selected for the analysis when the conditions described in the following subsections are met.

6.5.1 Trigger Requirement

Single jet triggers are used in this analysis. To simplify the description, they select events when (at least) one jet is found by the Level 3 of the trigger system above a selected threshold as specified in the trigger name. The complete jet trigger requirements on each level of the trigger system is shown in Table 6.1. The highest jet trigger is usually left unprescaled so it fires every time such event occurs, however lower triggers must be prescaled by some factor N, so they fire only every N-th event having such jet in order to limit the bandwidth for data recording. The majority of the events used in this analysis are triggered by the JT_95TT trigger, which means at least one jet with an uncorrected p_T above 95 GeV is present. Due to the energy resolution and the difference between the jet algorithms on the trigger and reconstruction levels, the trigger turn-on function is not a step function at 95 GeV but rather a convolution of a step-function with a resolution function. After the requirement on the leading jet transverse momentum, the trigger should be fully efficient which we cross-check by using the final $M_{3\mathrm{jet}}$ variable, where indeed a very steep turn-on is observed. We add a cut on the three-jet mass above this turn-on to ensure that the trigger is fully efficient (the precise leading p_T cut is rapidity dependent[64, 65] while we chose a single cut for all analysis regions).

At high mass, the JT_95TT data is replaced with JT_125TT in some bins to reduce statistical uncertainties. For more details about the trigger efficiency determination see Sec. 6.7.

Trigger name	Level 1	Level 2	Level 3	Luminosity (pb^{-1})
JT_125TT	CJT(4,5)	JET(60)	SCJET(125)	707.4
JT_95TT	CJT(3,5)	JET(50)	SCJET(95)	508.5
JT_65TT	CJT(3,5)	JET(20)	SCJET(65)	73.6
JT_45TT	CJT(2,5)	none	SCJET(45)	17.3

Table 6.1: Inclusive jet triggers in p17 data. Trigger requirements correspond to trigger list version v14.82 used in the latest runs considered in this analysis. Level 1 term CJT(x, y) requires x L1 calorimeter trigger towers above y GeV. Level 2 filter JET(x) passes events with jet candidates with $E_T > x\,\mathrm{GeV}$. Finally, Level 3 SCJET(x) term is satisfied and trigger fired if a jet candidate with $E_T > x\,\mathrm{GeV}$ was found using a simple cone algorithm.

6.5.2 Primary Vertex

The event is required to have at least one primary vertex found by the tracking system. When more vertices are found, the one most likely coming from the hard scattering has to be selected. Each vertex is assigned a probability that it comes from a minimum bias interaction based on the $\log_{10} p_T$ distribution of the tracks with $p_T > 0.5\,\mathrm{GeV}$. Vertices are ordered in the minimum bias probability, and the one with the lowest minimum bias probability is selected as the primary vertex. This ≥ 1 vertex requirement is to ensure that the jet energy and angles are properly measured. The vertex must have at least three tracks associated to it to remove fake vertices made by two tracks (this should not be a problem for QCD events where many charged particles are expected). The z position of the vertex must be within 50 cm of the center of the detector also to ensure that the properties of jets as well as jet energy scale calibration are properly determined.

The way to calculate the vertex efficiency is presented in a study of the luminous region in the detector[66]. The efficiency (mostly coming from the z position cut) is corrected by weights on an event-by-event basis because it depends on the instantaneous luminosity. The average vertex efficiency is about 92%.

6.5.3 Jets

The event must have at least three JCCA jets (Run IIa Midpoint cone jets of radius $R_{\mathrm{cone}} = 0.7$). The three leading jets in the event must be marked as good in terms of jet identification (jetID) quality requirements and confirmed at Level 1 of the trigger framework (jet.isGood() and jet.isL1Conf() flags

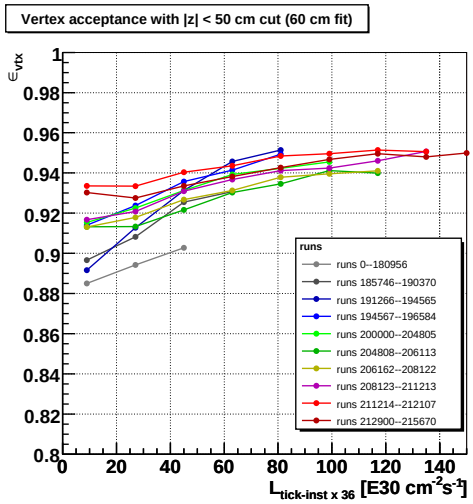

Figure 6.4: Vertex acceptance from minimum bias events[67].

using the standard p17 jetID). JetID quality requirements are completely described in [68]. Basically, two optimized cuts on fraction of jet energy deposited in electromagnetic (inner) layers of the calorimeter (EMF) and fraction of jet energy deposited in coarse hadronic layers of the calorimeter (CHF) are used. The EMF cut removes mostly overlap between jets and photons or electrons (high EMF) and also removes events jets formed by noise coarse hadronic calorimeter cells (low EMF cut). The CHF cut removes noisy jets potentially formed by noise in the coarse hadronic layer calorimeter cells which have poorer energy resolution. All three jets are required to have $|y|$ less than 0.8, 1.6 or 2.4 for the measurement of the dependence of the cross section on the rapidity and less than 2.4 for the measurement of the cross section dependence on jet transverse momenta.

A jet passes the EMF cut if:

- EMF < 0.95 or
- EMF > 0.05 or
- $0.13 > |\eta_{\text{det}} - 1.25| + \max(0, 40 \times (\sigma_\eta - 0.1))$ or
- EMF > 0.03 and $1.1 < |\eta_{\text{det}}| < 1.25$ or
- EMF > 0.04 and $2.5 < |\eta_{\text{det}}|$.

The EMF cut is optimized and depends on the jet width σ_η in the part of the detector called No EM Gap (no electromagnetic layers of calorimeter in the path of jets).

A jet passes the CHF cut if:

- CHF < 0.4 or
- CHF < 0.6 and $0.85 < |\eta_{\mathrm{det}}| < 1.25$ and $n90 < 20$ or
- CHF < 0.44 and $|\eta_{\mathrm{det}}| < 0.8$ or
- CHF < 0.46 and $1.5 < |\eta_{\mathrm{det}}| < 2.5$.

The cut uses the $n90$ variable which is a number of cells in a jet which contain 90% of jet scalar transverse energy ($\sum_{\mathrm{items}} |p_{Ti}|$). Noisy jets can be expected to have only one or a few cells.

A jet passes $\mathrm{L1}_{\mathrm{ratio}} = \mathrm{L1}\, p_T / \mathrm{precision}\, p_T$ cut if:

- $\mathrm{L1}_{\mathrm{energy}} > 55\,\mathrm{GeV}$ or
- $\mathrm{L1}_{\mathrm{ratio}} > 0.5$ or
- $\mathrm{L1}_{\mathrm{ratio}} > 0.35$ and $p_T < 15\,\mathrm{GeV}$ and $1.4 < |\eta_{\mathrm{det}}|$ or
- $\mathrm{L1}_{\mathrm{ratio}} > 0.1$ and $p_T < 15\,\mathrm{GeV}$ and $3.0 < |\eta_{\mathrm{det}}|$ or
- $\mathrm{L1}_{\mathrm{ratio}} > 0.2$ and $p_T \geq 15\,\mathrm{GeV}$ and $3.0 < |\eta_{\mathrm{det}}|$.

The precision p_T in the $\mathrm{L1}_{\mathrm{ratio}}$ is computed from the precision readout using uncorrected p_T and excluding coarse hadronic cells. The ratio is not used if the energy on Level 1 is large enough because of saturation of the L1 readout. The p_T dependent cuts are not important for the three jet analysis since the cuts are out of the phase space selected. Again, note that η_{det} is calculated with respect to the geometrical center of the detector and not to the primary vertex as for the physics η.

Efficiency of the jet identification requirements has been measured, but it is not directly applied to data. Instead the effect is taken into account when unsmearing the detector result back to the particle level in Section 6.18.

The p_T requirement on jet transverse momentum is 40 GeV (except when the cross section vs. p_T is measured where the requirement is also 70 and 100 GeV in the corresponding analysis regions). Another requirement is placed on the leading jet p_T to ensure that the trigger is 100% efficient (again see Section 6.7). These values correspond to jet energy scale corrected four-momenta. The requirement on the separation between jets i and j ($\Delta R_{ij} = \sqrt{(\Delta y_{ij})^2 + (\Delta \phi_{ij})^2}$) is set to 1.4 (twice the cone radius) to reduce the possibility of jets overlap. This avoids potential problems arising from the jet algorithm definition (IR/collinear sensitivity due to splitting/merging). Such hard cuts also limit the amount of initial and final state radiation testing directly the hard matrix element for the production of three jets.

6.5.4 Missing Transverse Energy

The missing transverse energy intends to remove fake jets produced by cosmic ray showers. The cosmic showers come from outside of the detector and typically deposit most of their energy on one side of the calorimeter leading to the missing transverse energy of an event ($\not\!\!E_T$) to be of comparable with the leading (in this case fake) jet transverse momentum. The cut on $\not\!\!E_T$ discards events if $\not\!\!E_T > 0.7$ jet p_T if $p_T < 100$GeV and $\not\!\!E_T > 0.5$ jet p_T if $p_T > 100$GeV using uncorrected leading jet p_T. Due to the cut on the leading jet p_T of 150 GeV (corrected, due to the trigger efficiency) this is effectively the latter only. This cut is designed to remove cosmic muons and also events where part of the calorimeter did not work correctly. Efficiency of this cut was found to be close to 100% on the inclusive sample and is not corrected for.

6.6 Dijet Jet Energy Scale

The analysis uses a specific version of jet energy scale derived originally for the inclusive jet sample (mainly dijets) where different responses to quarks and to gluons were implemented to match the composition of the QCD jet sample. Monte Carlo studies using the PYTHIA generator and the DØ detector simulation were done to check that this jet energy scale is applicable (within errors) to the three-jet sample. In the study, the detector level jets were corrected for J4S and the corrected p_T was compared with a p_T of a particle level jet matched with $\Delta R = R_{\rm cone}/2 = 0.35$. The mean value of variable $p_T^{\rm det}/p_T^{\rm ptcl} - 1$ is sensitive to the residual jet energy scale error while its RMS is the true Monte Carlo resolution. The matched jets were binned in bins of p_T(50 GeV width) and y (0.4 width from -2.4 to 2.4). The Monte Carlo p_T resolution and uncertainty was obtained from the **qcd_jet_caf** package. The same cuts as in Sec. 6.5.3 are used in the study. Figure 6.5 shows that while the resolution of the third jet is generally larger than the leading two jets (as expected if the third jet is mostly a gluon jet), it stays within the quoted uncertainties of the p_T resolution measurement and the third jet is not treated differently in the unsmearing procedure, where the resolutions are used (Sec. 6.9).

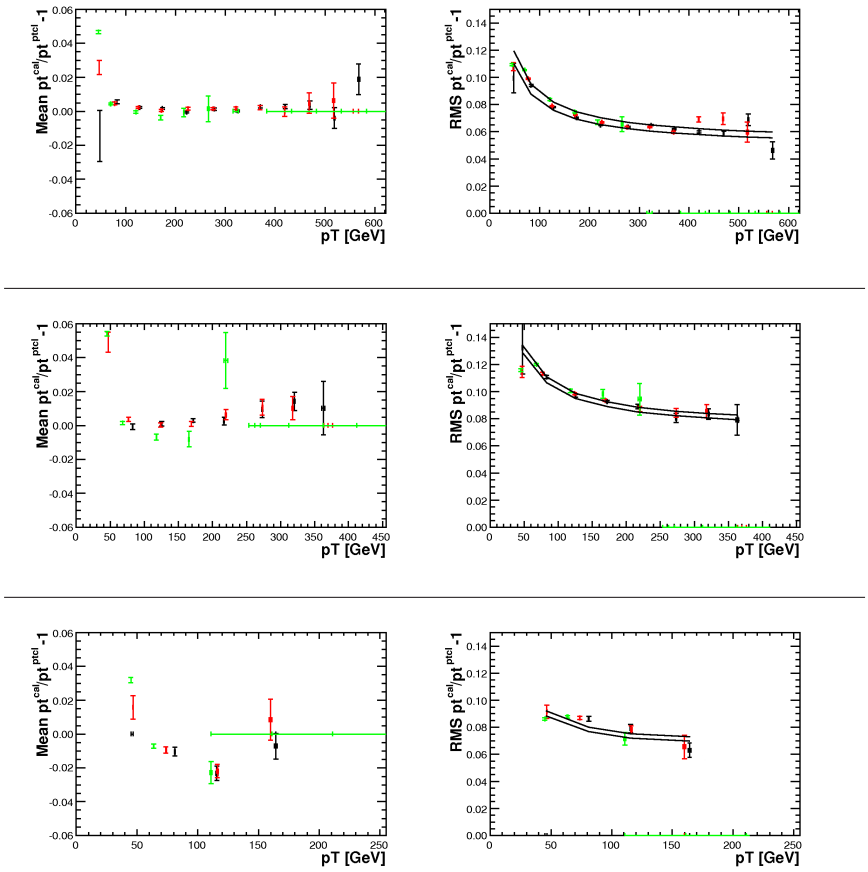

Figure 6.5: Third jet transverse momentum resolution study. Left plots show the residual jet energy scale calibration error for the leading jet (black), second jet (red) and third jet (green). The plots on the right show the truth MC p_T resolution for the leading, second and third jets together with the error band given by the qcd_jet_caf package (black line). The top plots correspond to jet rapidity in the region $-0.4 < y < 0.0$ (central det.), the middle plot to rapidity region $-1.6 < y < -1.2$ (intercryostat region) and the bottom one to rapidity $2.0 < y < 2.4$ (forward det.). The rapidity bins are chosen as examples, the remaining bins are included in [63].

6.7 Trigger Efficiency Studies

The relative trigger efficiency (turn-on curves) for the single jet triggers are determined in two steps – first by comparing the leading jet spectra between two triggers and setting high enough cuts on the leading jet p_T. Then the final turn-ons are cross-checked using the final state variable ($M_{3\text{jet}}$). If the lower $p_T$jet trigger is absolutely efficient then with the relative trigger efficiency, the absolute trigger efficiency of the higher trigger can be checked.

The relative trigger turn-on is done by comparing the JT_95TT spectra with JT_65TT and JT_125TT with JT_95TT. The absolute trigger turn-on for inclusive jet triggers cross-check was done in the inclusive jets analysis[64] using unbiased (no trigger requirement on the calorimeter) muon+jet sample.

All turn-on curves are fitted using the formula from Eq. 6.10.

$$F(x) = p_2 \cdot \mathrm{Erf}\left(\frac{x - p_1}{p_0}\right) \tag{6.10}$$

The parameter p_2 can depend on the range of the fit. A conservative overall trigger efficiency systematics of 2% is assigned due to this. The cut is always chosen to be above 99% of the fitted turn-on function (p_2 parameter). The phase space of the analysis is limited to the leading jet transverse momentum $p_T^1 > 150\,\mathrm{GeV}$ and three-jet mass $M_{3\text{jet}} > 400\,\mathrm{GeV}$ in all analysis regions. These cuts can be avoided (loosen) by using lower p_T triggers but this analysis concentrated on the high mass region (JT_65TT trigger could be used to reduce the leading jet p_T and $M_{3\text{jet}}$ cuts. Another reason for not using data with $M_{3\text{jet}} < 400\,\mathrm{GeV}$ is the steep rise of the cross section and potentially difficult unfolding in that region. The trigger JT_125TT is used to replace data from JT_95TT in the CC region (for $M_{3\text{jet}} > 670\,\mathrm{GeV}$) and in the IC region (for $M_{3\text{jet}} > 1100\,\mathrm{TeV}$). The leading jet p_T cut for JT_125TT trigger is 190 GeV. All three-jet events selected by the JT_95TT trigger which have $M_{3\text{jet}} > 670\,\mathrm{TeV}$ also have a leading jet $p_T > 190\,\mathrm{GeV}$. The same values are used for the rescaled three-jet mass introduced in Sec. 6.8.

There are 6 regions in the analysis. For the rapidity dependence, the regions are CC, IC, EC; for the p_{T3} dependence, the regions are 40, 70, 100. As the EC region selection is the same as the 40 region, there are 5 distinct distributions, the structure how the trigger curves are presented in Figs. 6.6–6.9 is shown in Table 6.2.

The following turn-on curves are presented:

- Fig. 6.6 - JT_95TT, leading jet p_T
- Fig. 6.7 - JT_95TT, final $M_{3\text{jet}}$ after cut of 150 GeV on leading jet p_T

- Fig. 6.8 - JT_125TT, leading jet p_T
- Fig. 6.9 - JT_125TT, final $M_{3\text{jet}}$ after cut of 190 GeV on leading jet p_T

Each figure lists $p_T/M_{3\text{jet}}$ values corresponding to 90, 95 and 99% of the turn-on plateau as well as the value of the plateau of the fit (parameter p_2).

1	2
3	4
5	

1. Three-jets in CC region ($|y| < 0.8$ and $p_{T3} > 40\,\text{GeV}$)
2. Three-jets in IC region ($|y| < 1.6$ and $p_{T3} > 40\,\text{GeV}$)
3. Three-jets in EC region ($|y| < 2.4$ and $p_{T3} > 40\,\text{GeV}$)
4. Three-jets above 70 ($|y| < 2.4$ and $p_{T3} > 70\,\text{GeV}$)
5. Three-jets above 100 ($|y| < 2.4$ and $p_{T3} > 100\,\text{GeV}$)

Table 6.2: Legend on how each region is placed in Figures 6.6–6.9.

CC

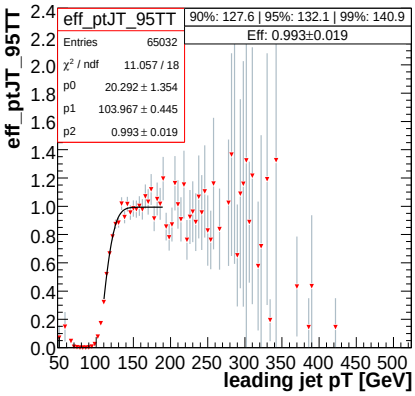

IC

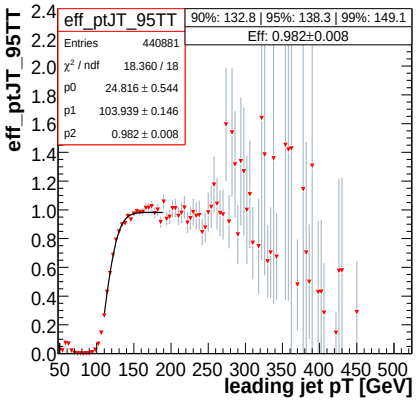

EC

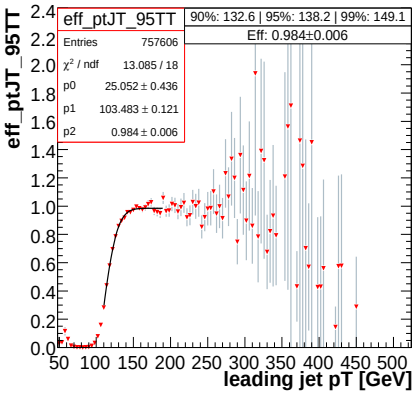

70

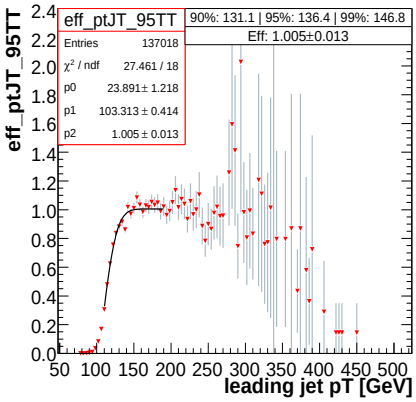

100

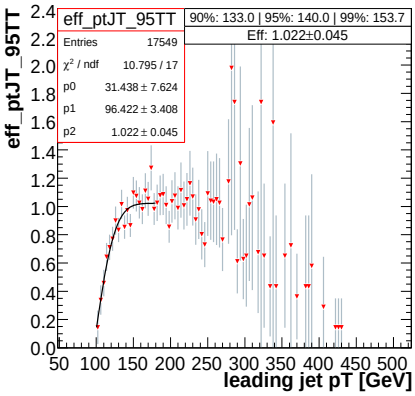

Figure 6.6: Trigger turn-on for leading jet spectra, JT_95TT trigger.

CC

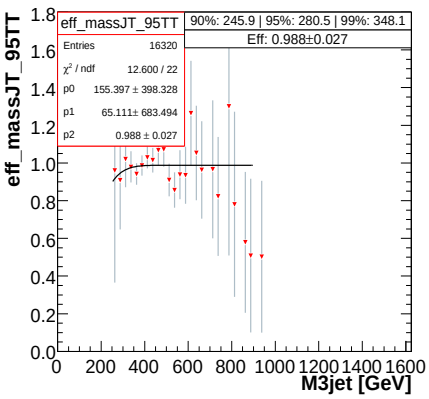

IC

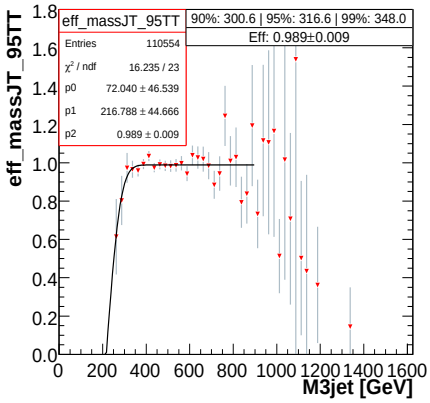

EC

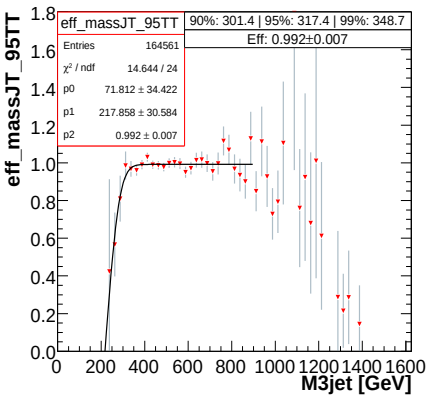

70

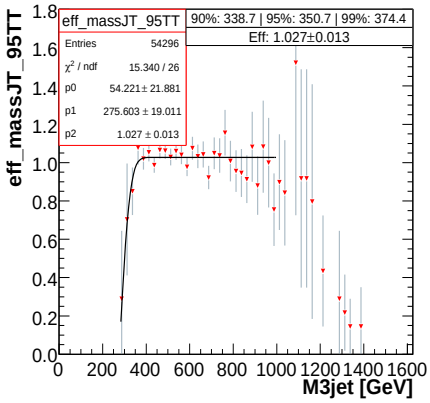

100

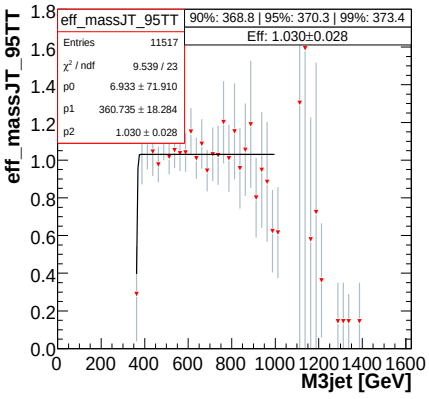

Figure 6.7: Trigger turn-on for three-jet mass, JT_95TT trigger, leading jet cut 150 GeV.

CC

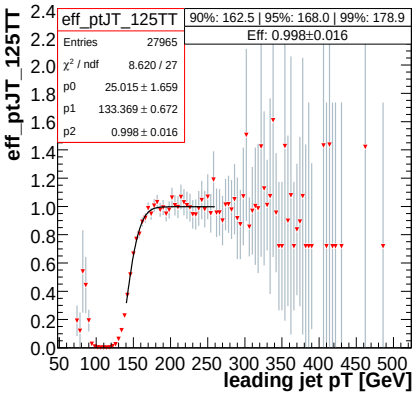

IC

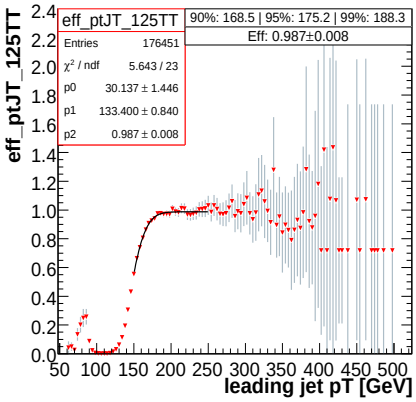

EC

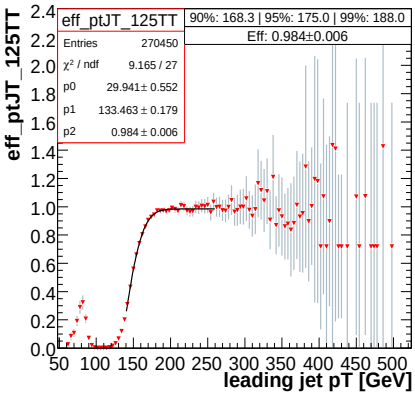

Figure 6.8: Trigger turn-on for leading jet spectra, JT_125TT trigger.

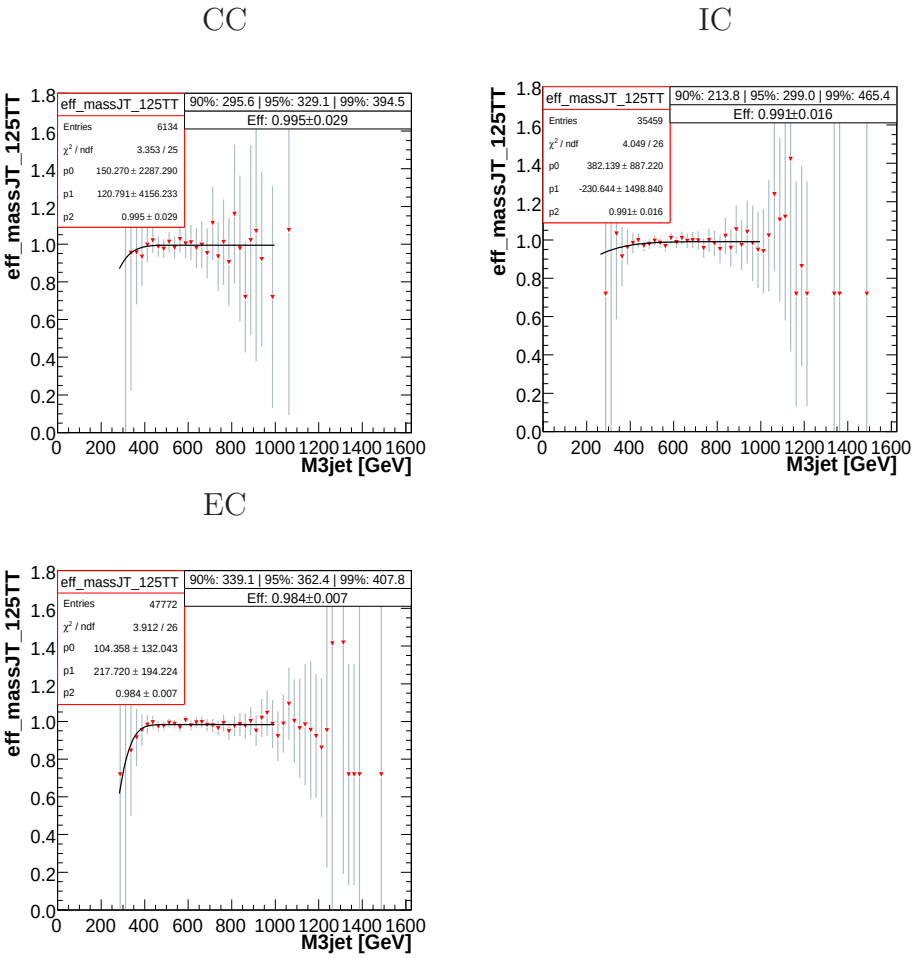

Figure 6.9: Trigger turn-on for three-jet mass, JT_125TT trigger, leading jet cut 190 GeV.

6.8 Three-jet Mass Bin Width Selection

Bins in the three-jet mass $M_{3\text{jet}}$ were selected following these conditions:

- The $M_{3\text{jet}}$ resolution was estimated by matching the three-jets at particle and detector levels using p17 PYTHIA QCD sample. In this simple study, to each of the leading three particle jets, a calorimeter jet was searched within a distance $\Delta R = R_{\text{cone}}/2 = 0.35$ and if all three leading particle jets were matched to detector level jets, the ratio between $M_{3\text{jet}}$ at particle and detector levels was determined. The bin width ($\sim 10\%$) is selected to be roughly twice the RMS of the distribution.

- The highest mass bins are limited by statistics. The choice of binning is so that each analysis bin has enough statistics and that $M_{3\text{jet}}$ bins are the same in every analysis region.

- Efficiencies and purities are checked to be at reasonable level using a parameterized detector simulation d0jetsim[69] (for details about the simulation, see Sec.6.9). The efficiency e_i in a given mass bin is defined as the number of events generated and reconstructed in that bin divided by a number of all events generated in that bin. The purity p_i in some mass bin is defined as the number of events generated and reconstructed in that bin divided by a number of all events which were reconstructed in that bin:

$$e_i = \frac{N_{ii}}{\sum_j N_{ij}}, \tag{6.11}$$

$$p_i = \frac{N_{ii}}{\sum_j N_{ji}}, \tag{6.12}$$

  where N_{ij} is the number of events which were generated in i-th bin and after smearing ended in the j-th bin. Mass rescaling similar to those used in the dijet-χ[70] and dijet mass[71] measurements was used to improve the efficiencies and purities. The rescaling formula is given in Eq. 6.13 (masses in TeV). The parameters in the rescaling are the same as in dijet-χ measurement except that the parameter in the exponent in Eq. 6.13 was optimized for three jet PYTHIA sample[72].

$$RM_{3\text{jet}} = M_{3\text{jet}}^{\text{rescaled}} = M_{3\text{jet}}^{\text{reco}} - 0.0005 \cdot (M_{3\text{jet}}^{\text{reco}}/0.25)^{2.5} \tag{6.13}$$

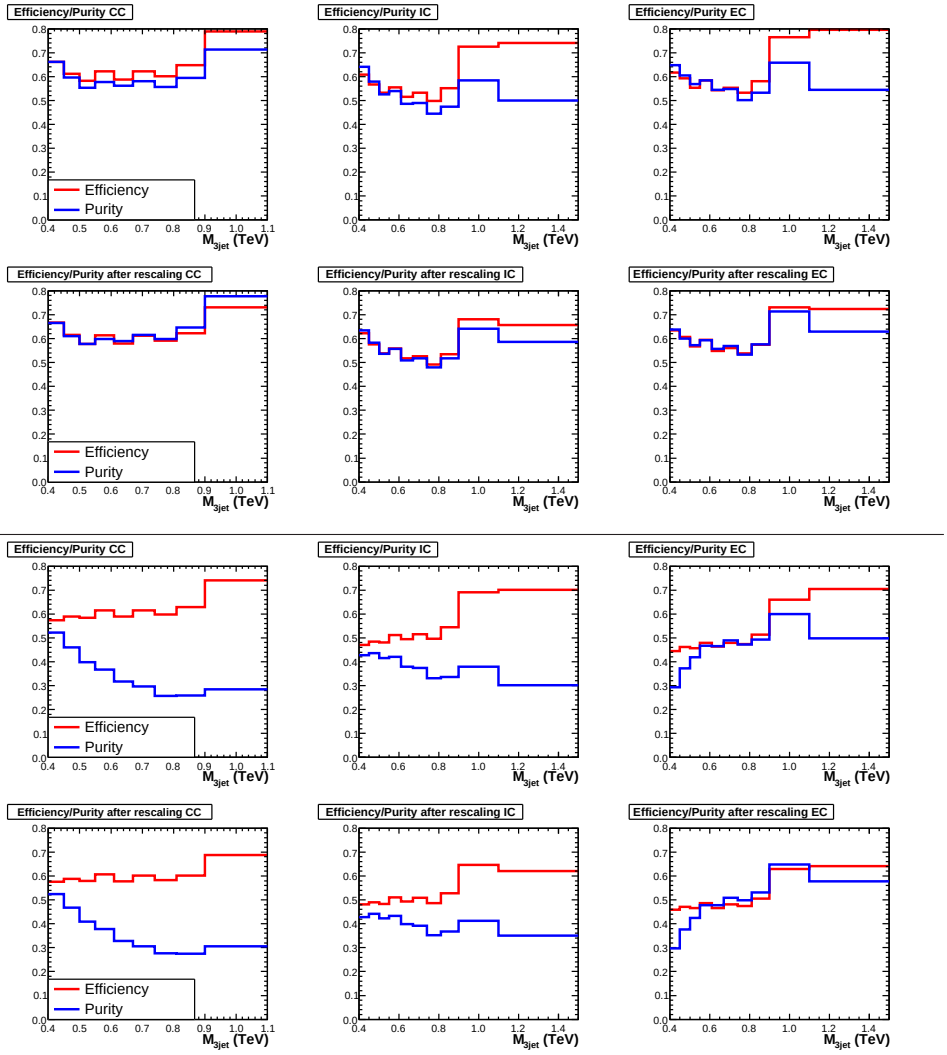

Figure 6.10: Efficiencies and purities in CC, IC and EC regions before and after the three-jet mass rescaling. Note that the top six plots consider only smearing across $M_{3\text{jet}}$ mass bins and not events which were smeared inside or outside of the particular analysis region. In that case, the purities can drop down by a factor of 2 (bottom six plots).

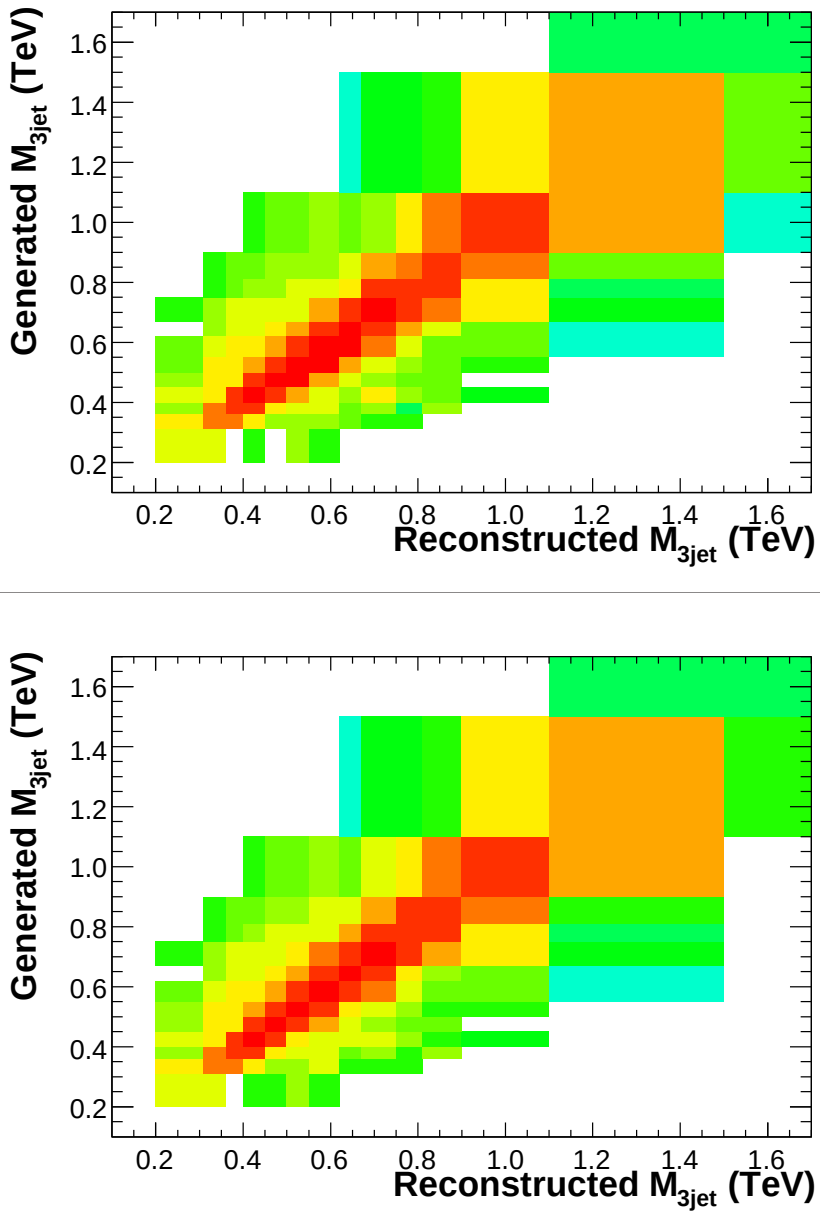

Figure 6.11: The reconstructed mass vs the generated mass without (top) and with mass rescaling (bottom) in EC region of the analysis. Events which migrated in or out of the analysis regions are not shown.

6.9 Unsmearing

All measured properties are intrinsically connected to the DØ detector. In order to present a measurement at the particle level (Fig. 3.1), the detector effects have to be deconvoluted from it. The procedure for it is called unsmearing (or unfolding). In a steeply falling, such as the three-jet mass, events tend to migrate preferentially from a lower mass bin to a higher mass bin. The cartoon of this effect is shown in Fig. 6.12.

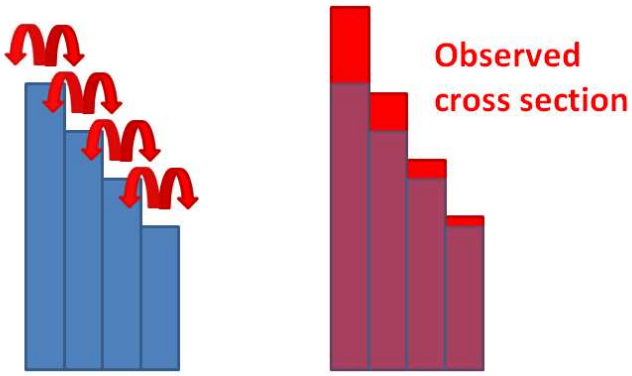

Figure 6.12: Migration of events due to resolution on a steeply falling spectrum

There are several methods to unsmear the data. An ansatz method has been used in an inclusive jet measurement at DØ[67]. An ansatz function with several free parameters based on a priori knowledge about the truth particle spectrum is chosen and the parameters are fitted to the data distribution in several iterations. The complications arise when the studied distribution is smeared by several variables and the procedure would become too difficult. In this analysis, a Monte Carlo simulation method (d0jetsim[69]) developed by M. Wobisch is used instead. Instead of an ansatz, a set of generated Monte Carlo events is used. The package then smears the generated jets using experimental resolutions determined predominantly from data in order to obtain unsmearing correction factors. The advantage is that the a priori knowledge is not needed in a functional form, the disadvantage is that the Monte Carlo needs to correctly model the data at least to a level from where it can be fine-tuned. The effects which are modeled in the simulation include:

- jet p_T resolutions;
- jet angular resolutions – η, ϕ;

- jet angular biases – η;
- jetID efficiency;
- vertex efficiency;
- jet energy scale.

6.9.1 Transverse Momentum Resolution

Since the three-jet mass depends directly on each jet (transverse) momentum and because of the steeply falling transverse momentum spectrum, the jet transverse momentum resolution is the single most dominant resolution effect. The jet transverse momentum was studied in detail first by M. Voutilainen[73] and then adapted by M. Rominsky[74] for use in d0jetsim. A brief description of its measurement together with the results is presented below.

The jet transverse momentum can be measured directly using p_T imbalance in back-to-back ($\Delta\phi > 3.0$) dijet events. The asymmetry distribution A between the two highest transverse momentum jets defined as

$$A = \frac{p_T^{(1)} - p_T^{(2)}}{p_T^{(1)} + p_T^{(2)}} \tag{6.14}$$

is used for the resolution determination (the p_T order between the two jets is randomized). The mean value of the asymmetry distribution is sensitive to the relative jet energy scale between the two jets. Its width serves as a raw value of the transverse momentum resolution which is corrected for additional effects studied in Monte Carlo. The distribution is binned in bins of $(p_T^{(1)} + p_T^{(2)})/2$ and jet rapidities.

The truth Monte Carlo resolution is defined as the RMS of the reconstructed p_T jet vs particle p_T jet defined in Eq. 6.15.

$$\left(\frac{\sigma p_T}{p_T}\right)_{\text{truth}} = RMS\left(\frac{p_T^{\text{reco}} - p_T^{\text{ptcl}}}{p_T^{\text{ptcl}}}\right) \tag{6.15}$$

When both jets are in the same central rapidity bin, the resolution σ_{p_T}/p_T is directly to the truth resolution

$$\frac{\sigma_{p_T}}{p_T} = \sqrt{2}\sigma_A. \tag{6.16}$$

The central detector region with $|y| \leq 0.8$ is used as a reference bin. The resolution in forward detector bins is measured with dijets where one jet is in the central region and the second one in the probed forward region.

$$\frac{\sigma}{p_T^{\text{probe}}} = \sqrt{4\sigma_A^2 - 2\sigma_{A\text{ref}}^2}, \tag{6.17}$$

where σ_{Aref} is the asymmetry width when both jets are in the reference region.

The resolutions derived according to Eqs. 6.14-6.17 correspond to the true resolution only in an ideal case where only the dijet and nothing else is produced in an event. The additional energy is coming from two sources. First is the jet reconstruction threshold - even when additional jets produced in the event are vetoed in the event selection for the resolution measurement, additional jets can be produced in the event and spoil the dijet balance but then not reconstructed because of the minimum reconstruction p_T cut of 6 GeV. The resolutions are measured with a p_T cut veto on an additional jet present. Several p_T thresholds are used and the using linear interpolation is used to determine $(\sigma_{p_T}/p_T)_{p_T^{\text{cut}}} \to 0\,\text{GeV}$. The soft radiation correction k_{soft} is then determined as

$$k_{\text{soft}} = \frac{\left(\frac{\sigma_{p_T}}{pt}\right)_{p_T^{\text{cut}} \to 0\,\text{GeV}}}{\left(\frac{\sigma_{p_T}}{p_T}\right)_{p_T^{\text{cut}} \to 6\,\text{GeV}}}. \tag{6.18}$$

Particle level imbalance is caused by proton remnants and in terms of underlying event energy contributes additionally to the total dijet imbalance. This term is studied using Monte Carlo simulation.

The corrected resolution can be expressed as

$$\sigma_{p_T} = \sqrt{(k_{\text{soft}}\sigma_{\text{raw}})^2 - \sigma_{\text{MC}}^2}. \tag{6.19}$$

Additional corrections are used to describe non-gaussian tails in the resolutions coming both from detector sources (punchthrough, where not all jet energy is detected due to small depth of the calorimeter) and particle level imbalance (caused by neutrinos and muons inside jets which are not considered in the DØ jet algorithm/ jet energy scale determination). Due to this effects, the final resolution is best described by two gaussians and an exponential tail. The jet transverse momentum resolutions were rederived in terms of jet detector pseudorapidity which is more suited for the parameterized detector simulation. The final transverse momentum resolutions for each detector pseudorapidity bin are shown in Fig. 6.13. The resolution is the best in the central and forward regions while the intercryostat region is slightly worse as expected.

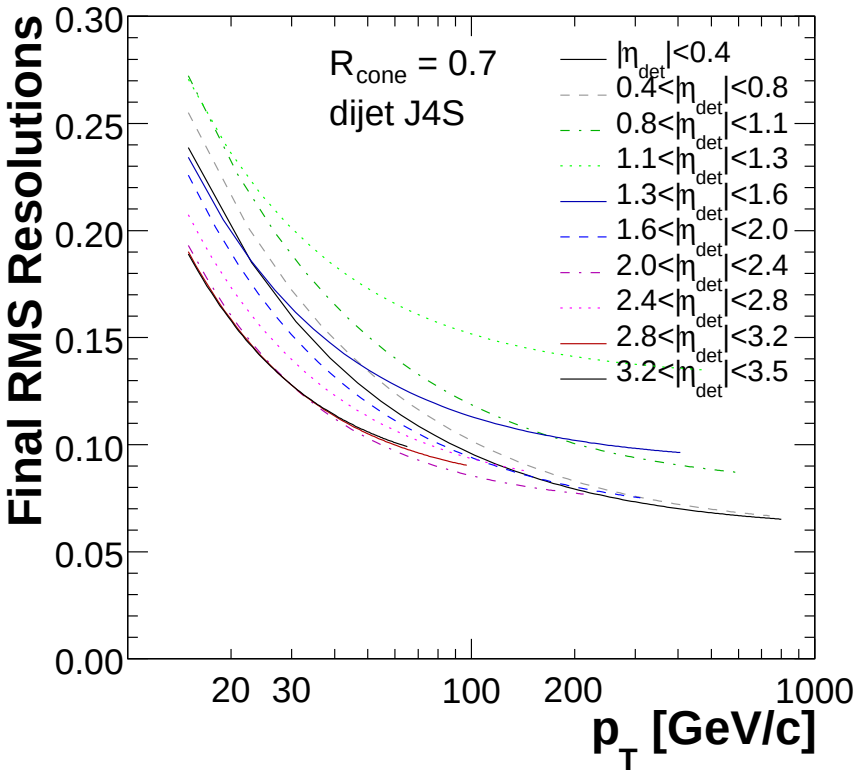

Figure 6.13: Jet transverse momentum resolution as a function of η_{det}. Taken from [74].

6.9.2 Angular Resolutions

Since the angular resolutions can not be measured directly in data, the Monte Carlo with full detector simulation is used in order to measure them. In the simulation, selected jets are matched between particle and detector (calorimeter) level and the difference in the η and ϕ on the two levels serve as the estimate of the angular resolutions. The angular resolutions are affected both by detector effects due to angular smearing during the shower evolution and also by jet algorithm effects (namely splitting and merging).

After selecting good events in terms of data quality, nearby all particle level jets, detector jets are searched in $\Delta R = \sqrt{(\eta_{\text{ptcl}} - \eta_{\text{cal}})^2 + (\phi_{\text{ptcl}} - \phi_{\text{cal}})^2}$. When both jets are matched within $\Delta R \leq R_{\text{cone}}/2 = 0.35$, they are selected

for measuring the resolutions. The difference

$$\Delta\eta = \eta_{\text{ptcl}} - \eta_{\text{cal}} \tag{6.20}$$

$$\Delta\phi = \phi_{\text{ptcl}} - \phi_{\text{cal}} \tag{6.21}$$

is then binned in terms of particle level transverse momentum p_T^{ptcl} and jet detector-η η_{det} (10×16 bins). In each $p_T^{\text{ptcl}} \times \eta_{\text{det}}$ the $\Delta\eta$ ($\Delta\phi$) is fitted with a double gaussian function of the form

$$f(x) = A_1 * \exp\left(-\frac{1}{2}\left(\frac{x-\mu}{\sigma_1}\right)^2\right) + A_2 * \exp\left(-\frac{1}{2}\left(\frac{x-\mu}{\sigma_2}\right)^2\right). \tag{6.22}$$

The mean of the gaussian, which is assumed to be the same for both of them, should be in an ideal case close to zero. The non-zero mean in the case of η resolutions is considered separately in Sec. 6.9.3. The RMS of the $f(x)$ distribution corresponds to the angular resolutions. To generate random number from the double gaussian distribution from Eq. 6.22, three parameters are needed - the widths of both gaussians (σ_1, σ_2) and the ratio of the areas below the gaussians $f = \frac{\text{area}_1}{\text{area}_1+\text{area}_2}$.

To simplify the usage of the resolutions, the individual parameters of the double gaussian fit $\sigma_1(p_T, \eta_{\text{det}})$, $\sigma_2(p_T, \eta_{\text{det}})$ and $f(p_T, \eta_{\text{det}})$ are fitted with continuous functions in p_T. The best agreement is achieved using the following forms:

$$F_{\sigma_1,\sigma_2}(p_T) = A + \frac{B}{p_T} + \frac{C}{pt^2} \tag{6.23}$$

$$F_f(p_T) = 1 - \exp(A - Bp_T) \tag{6.24}$$

in 16 bins of η_{det} and tabulated version of the fits is used in the parameterized d0jetsim simulation.

Fit plots for all parameters from the procedure outlined above are shown in Figs. 6.14 and 6.15 while the full set of plots is presented in [75].

6.9.3 Rapidity Bias

The simulation package also corrects for the angular η-bias. A systematic shift is observed in a Monte Carlo simulation between a (pseudo)rapidity of jets on particle and detector levels mostly due to nonuniformity of the calorimeter at the boundaries of the central and forward cryostats. The size of the rapidity bias is shown in Fig. 6.16.

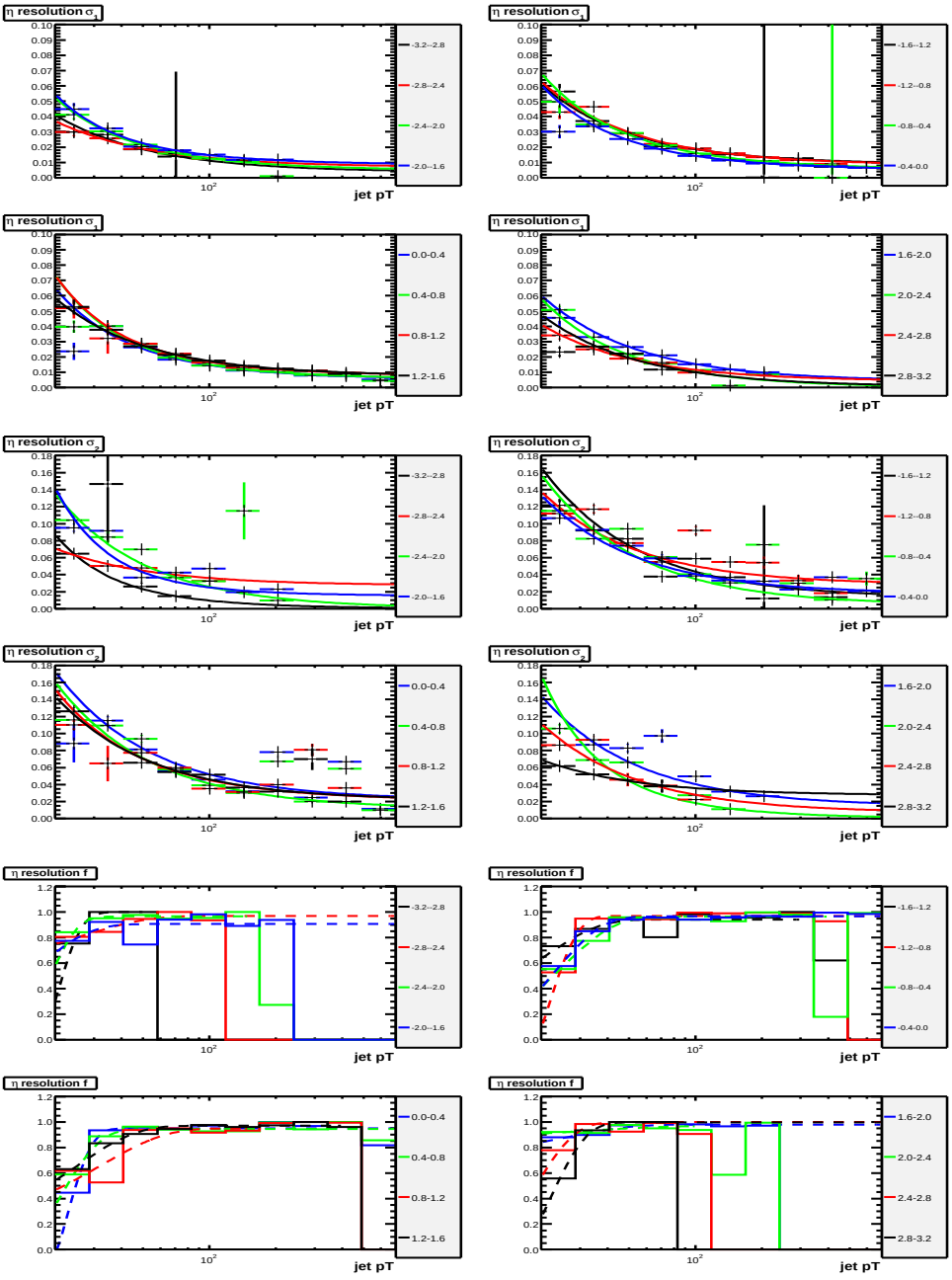

Figure 6.14: η resolution parameters, p_T dependence of fit parameters σ_1 (top four figures), σ_2 (middle four), f (bottom four) for η resolutions. 4 figures for each parameter, each contains 4 η^{det} bins.

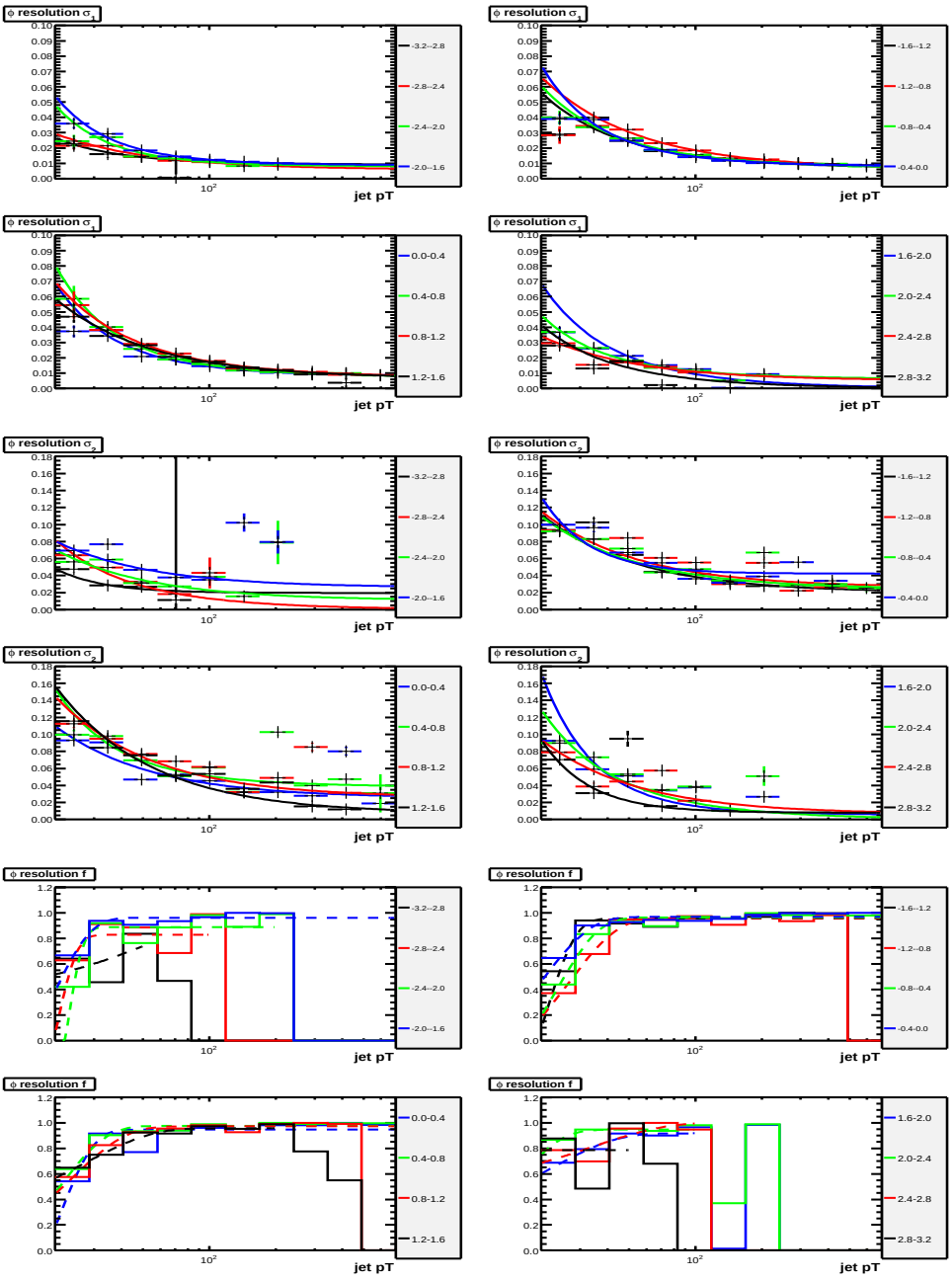

Figure 6.15: ϕ resolution parameters, p_T dependence of fit parameters σ_1 (top four figures), σ_2 (middle four), f (bottom four) for ϕ resolutions. 4 figures for each parameter, each contains 4 η^{det} bins.

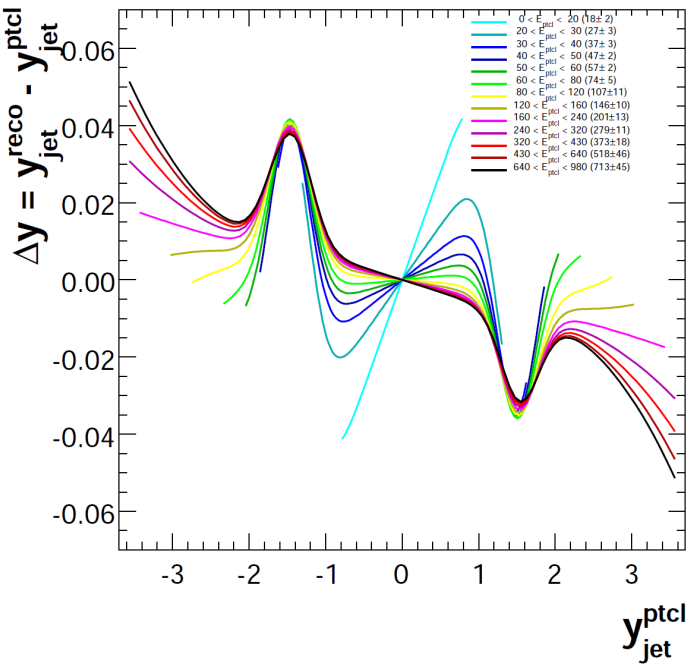

Figure 6.16: Rapidity bias parameterization, taken from [67].

6.9.4 Jet Simulation

Events generated with a Monte Carlo generator on the particle level are smeared using the measured resolutions. The ratio between the smeared (detector) level and the original particle level distribution in the variable of interest (in this measurement it is the three-jet mass $M_{3\text{jet}}$) are used to determine the unsmearing coefficients which are then applied to data. The unsmearing coefficient is defined as the ratio between the particle level and detector level variable

$$C_{\text{unsmear}} = \frac{MC^{\text{particle}}}{MC^{\text{detector}}} \tag{6.25}$$

and then applied to the data to get the particle (unsmeared) level cross section

$$DATA^{\text{unsmeared}} = C_{\text{unsmear}} \cdot DATA = \frac{MC^{\text{particle}}}{MC^{\text{detector}}} \cdot DATA \tag{6.26}$$

In order to use the unsmearing factors, the original smeared Monte Carlo distribution must describe the data. A set of control variables is chosen to show the level of agreement between the simulation and the data. It has been found that the default versions of common parton shower generators (Pythia, Herwig) do not provide a reasonably good agreement while $2 \to N$ LO ME generators (Alpgen, Sherpa) describe the data better (an example distribution is shown in Fig. 6.17). The Sherpa event generator is used for this analysis. The default version of the Sherpa generator needed a reweighting to achieve a good agreement with the data (except of the rapidity distribution of the fourth jet). The reweighting was established via an iterative procedure where the events were reweighted by a few three jet variables until a reasonable description was achieved. The final reweighting function used is

$$w' = 1.15 \cdot (1 - 0.25 \cdot M_{3\text{jet}}) \cdot (1 - 0.06 \cdot |y_3|) \cdot (1 + 0.055 \cdot |y_1|) \cdot w, \tag{6.27}$$

where the variables (three-jet mass $M_{3\text{jet}}$, leading jet rapidity y_1 and third leading jet rapidity y_3) are taken from the particle level. The original event weight w comes from the generated cross section. The control plots are presented in Appendix A. Pythia event generator with a reweighting which was used in dijet mass analysis is used to cross check the stability of the unsmearing factors and a systematic uncertainty is assigned for the modeling difference.

The unsmearing correction also contains a correction for energies of muons and neutrinos which are not taken into account in the JES/J4S correction. The unsmearing factors are presented in Fig. 6.18. To reduce the statistical

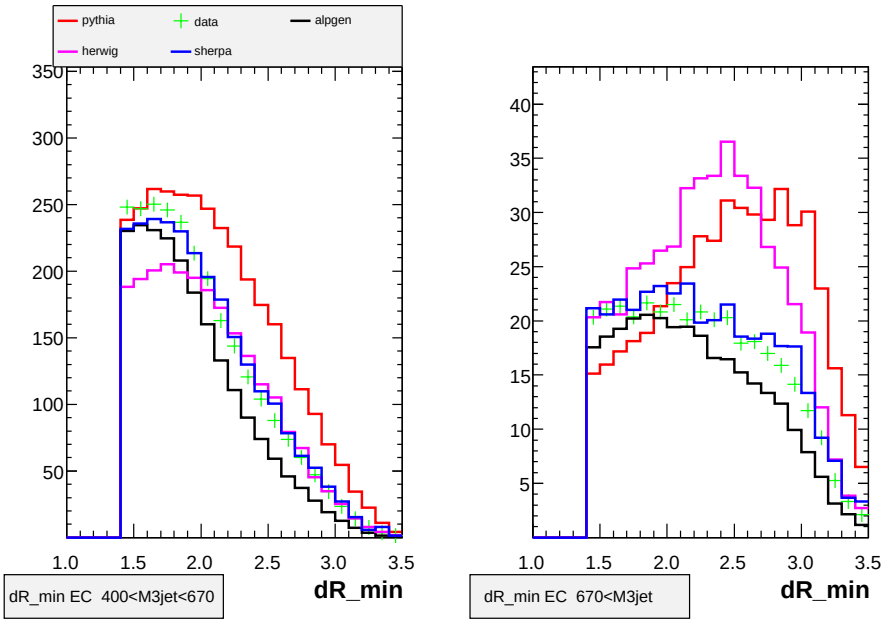

Figure 6.17: Minimum distance between jets in three-jet events comparing different Monte Carlo generators and data (in green) in the EC region ($|y| < 2.4$)). Note that the normalization is arbitrary, but the shape of the distribution favors the $2 \to N$ generators (as described in the text).

fluctuations the total unsmearing factor is fitted with a second order polynomial function and the smooth version is used in the analysis (Fig. 6.19).

6.10 Uncertainties

There are two types of uncertainties associated with each experimental measurement; statistical and systematic. Statistical uncertainty corresponds to the uncertainty due to the final amount of data. In each $M_{3\text{jet}}$ mass bin, the relative statistical uncertainty is given by $\sqrt{N}/N$, where N is the number of events in that bin. Most of the systematic uncertainties are estimated using the d0jetsim simulation. These include the uncertainties coming from p_T resolution (15 different sources), angular resolutions and biases, jetID efficiencies, vertex efficiencies and jet energy scale (48 different sources).

The individual p_T resolution uncertainty sources contain the systematic uncertainties for the final fit, soft radiation correction, particle level imbalance, closure residual and noise component and statistical uncertainty of the

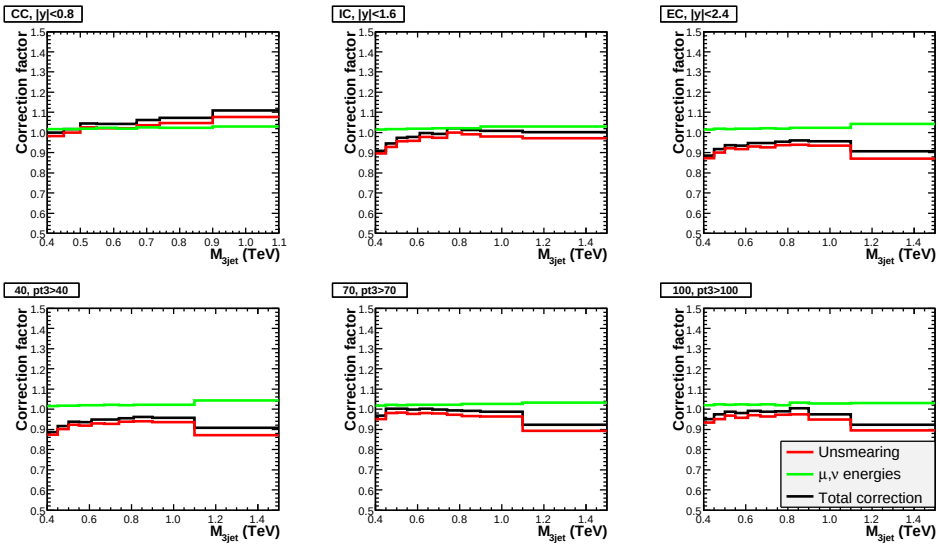

Figure 6.18: Unsmearing coefficients obtained using the d0jetsim simulation in all analysis regions. The dominant contribution to the unsmearing (red curve) comes from the jet transverse momentum resolutions, the second largest individual subcorrection is from jetID efficiency, the contribution of angular resolutions is small.

fit (Table 6.3).

The individual jet energy sources are described in Table 6.4.
In total, the following uncertainties are considered:

- Trigger efficiency - 2%, assigned in Section 6.7;
- Luminosity - 6.1% for Run IIa[54];
- MC reweighting - 2.5% from the difference between the unsmearing factors from PYTHIA and SHERPA(Fig. 6.20);
- Vertex efficiency - assigned 0.5% (Fig. 6.21);
- η bias - 3% (Fig. 6.22);
- JetID (Fig. 6.23);
- η resolutions - 1% (Fig. 6.24);
- ϕ resolutions - 0.5% (Fig. 6.25);
- p_T resolutions (Figs. 6.26–6.28);

Component	Description	Component	Description
ptres_01	fit uncertainty	ptres_09	statistical CC1
ptres_02	soft correction	ptres_10	statistical CC2
ptres_03	ptcl-level p_T imbalance	ptres_11	statistical IC1
ptres_04	noise CC	ptres_12	statistical IC2
ptres_05	noise IC	ptres_13	statistical EC1
ptres_06	noise EC	ptres_14	statistical EC2
ptres_07	noise forward	ptres_15	statistical forward
ptres_08	closure		

Table 6.3: Uncertainty sources of the jet transverse momentum resolution.

- JES (Figs. 6.29-6.35).
- Statistical uncertainty of the unsmearing factors (taken as 80% (due to the partial correlation between the two samples which are used there) of the stat. uncertainty from Fig. 6.19)

The uncertainty of individual systematic is estimated by varying the effect by $\pm 1\,\sigma$ from its central value and comparing the variation with the central value. The total uncertainty due to p_T resolution (JES) is calculated by adding all 15 (48) individual sources uncertainties together in quadrature. The total systematic uncertainty is calculated again by adding in all above mentioned effects in quadrature. For some systematics the correlations are not completely known and therefore separate up and down variations of the effect in CC, IC and EC are considered, but the overall variation is generally the largest and is taken as the effect systematics (jetID, η-bias, η, ϕ resolutions).

ID	Description	ID	Description
jes_001	EM energy scale	jes_025	η fit in EC
jes_002	Dead material	jes_026	η fit in EC
jes_003	Photon energy scale	jes_027	Zero suppression bias
jes_004	Photon sample purity	jes_028	ZSb number of vertices
jes_005	EM-jet background	jes_029	ZSb jet matching
jes_006	High-p_T extrapolation	jes_030	MPF method bias
jes_007	PDF uncertainty at high p_T	jes_031	MPFbPythiavs Herwig
jes_008	time stability	jes_032	MPFb scaling
jes_009	Fit in CC kRjetCCStat0	jes_033	MPF jet matching p_T
jes_010	Fit in CC kRjetCCStat1	jes_034	Detector showering
jes_011	Fit in CC kRjetCCStat2	jes_035	Shw sample purity
jes_012	η-intercalibration in CC	jes_036	Shw scaling
jes_013	η-intercalibration in IC	jes_037	Shw jet matching
jes_014	η-intercalibration in IC	jes_038	Shw template fits
jes_015	η-intercalibration in EC	jes_039	Shw Tune A vs Tune DW
jes_016	η-intercalibration in EC	jes_040	Closure
jes_017	η-intercalibration in EC	jes_041	MPFb for dijets
jes_018	η-intercalibration in EC	jes_042	MPFb for dijets
jes_019	JES resolution bias	jes_043	Dijet CC response
jes_020	η fit in CC	jes_044	Dijet CC response
jes_021	η fit in IC	jes_045	Dijet CC response
jes_022	η fit in IC	jes_046	Dijet CC response
jes_023	η fit in EC	jes_047	Inclusive jet response
jes_024	η fit in EC	jes_048	Offset systematics

Table 6.4: J4S systematic eigenvectors.

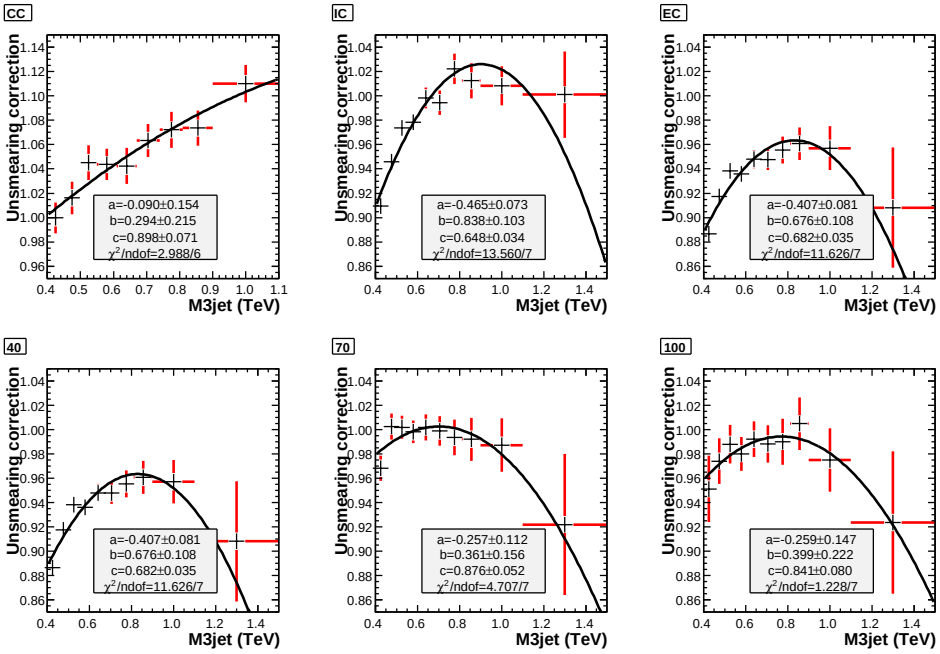

Figure 6.19: Fit of the total unsmearing factors with a second order polynomial function.

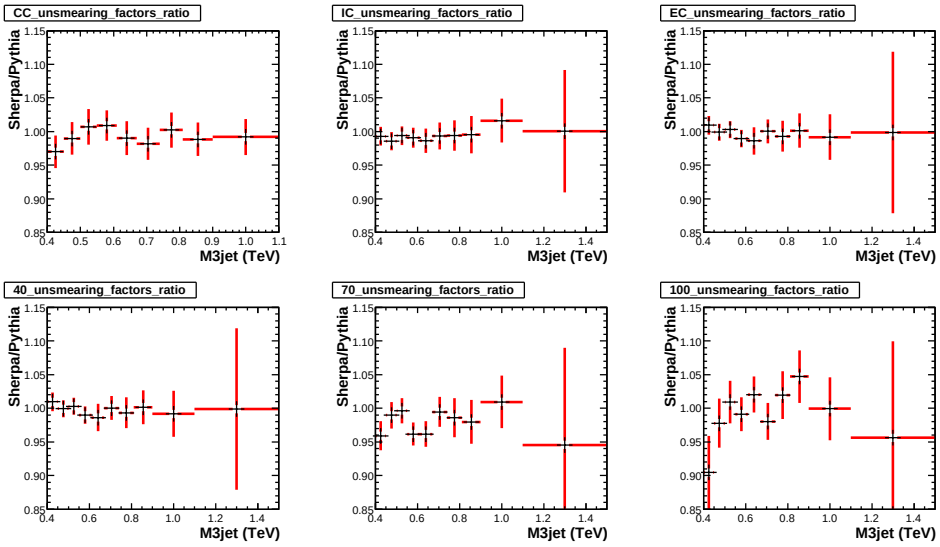

Figure 6.20: Ratio between the total unsmearing factors from Sherpa and Pythia Monte Carlo events. A systematic uncertainty of 2.5% is assigned due to different Monte Carlo modeling.

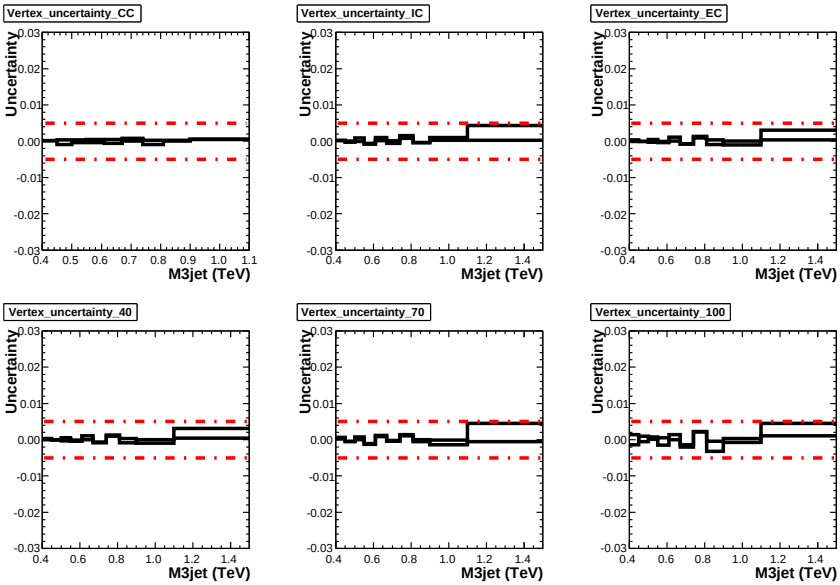

Figure 6.21: Vertex efficiency uncertainty. Red dash-dotted 0.5% lines show the assigned systematic uncertainty.

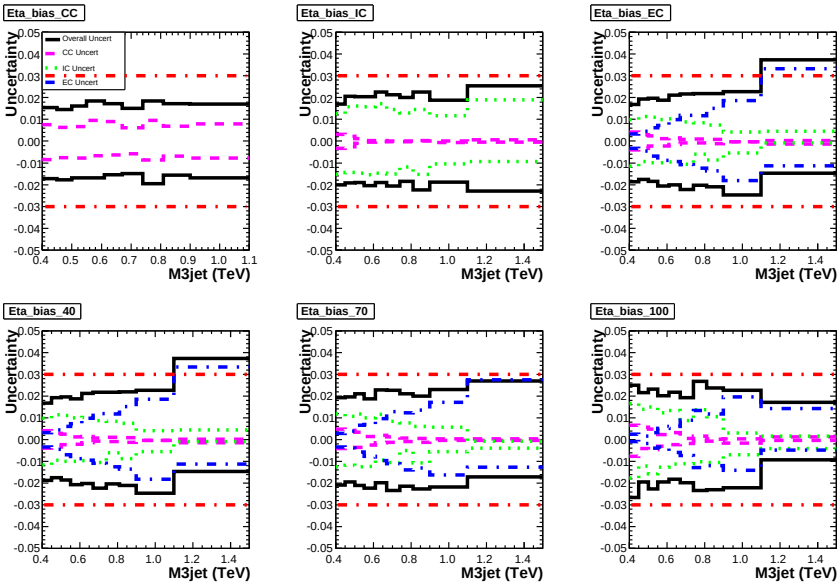

Figure 6.22: η bias uncertainty. Red dash-dotted 3% lines show the assigned systematic uncertainty.

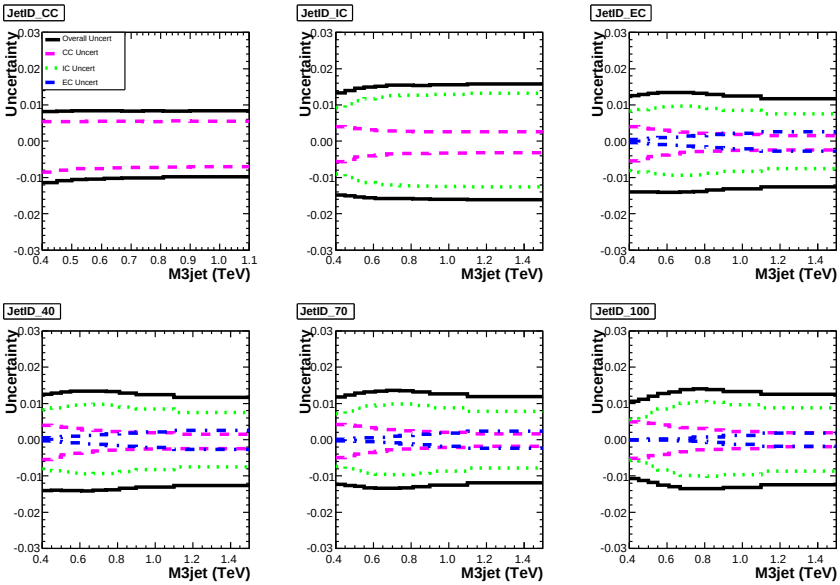

Figure 6.23: JetID uncertainty. The JetID efficiency is derived from data but is applied in the simulation.

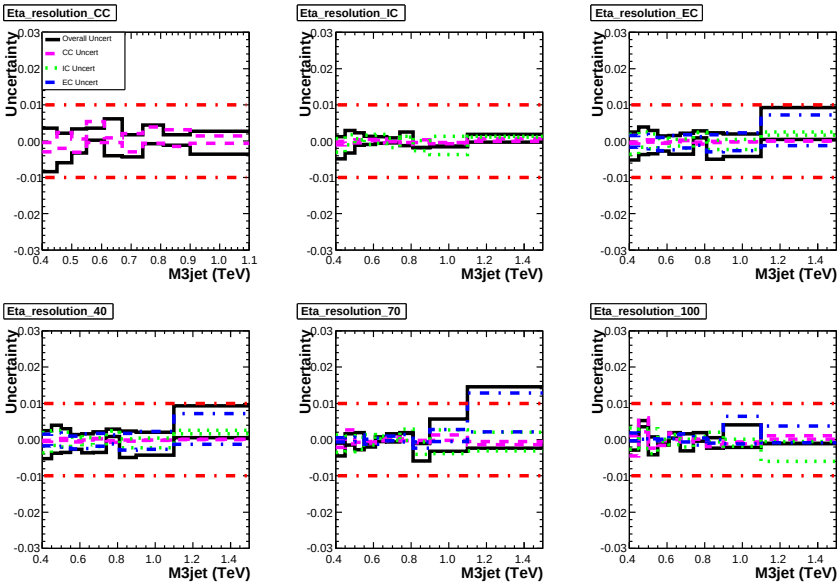

Figure 6.24: η resolution uncertainty. Red dash-dotted 1% lines show the assigned systematic uncertainty.

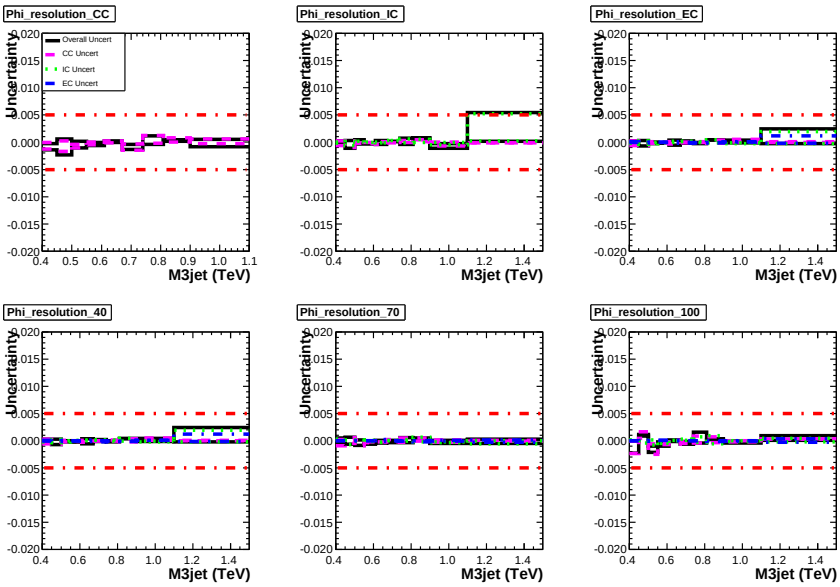

Figure 6.25: ϕ resolution uncertainty. Red dash-dotted 0.5% lines show the assigned systematic uncertainty.

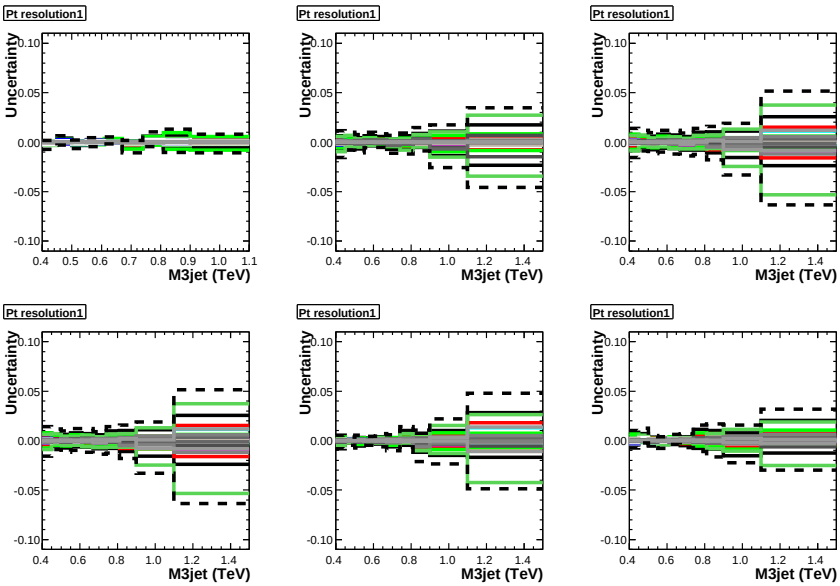

Figure 6.26: Transverse momentum resolution uncertainty (sources 1–5 in Table 6.3). Black dashed line shows the total uncertainty due to transverse momentum resolution with all 15 sources added in quadrature.

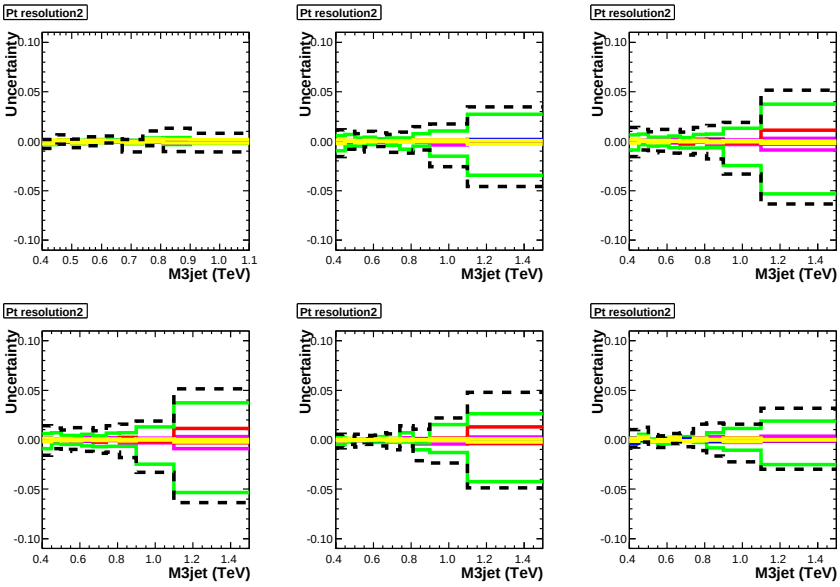

Figure 6.27: Transverse momentum resolution uncertainty (sources 6–10 in Table 6.3). Black dashed line shows the total uncertainty due to transverse momentum resolution with all 15 sources added in quadrature.

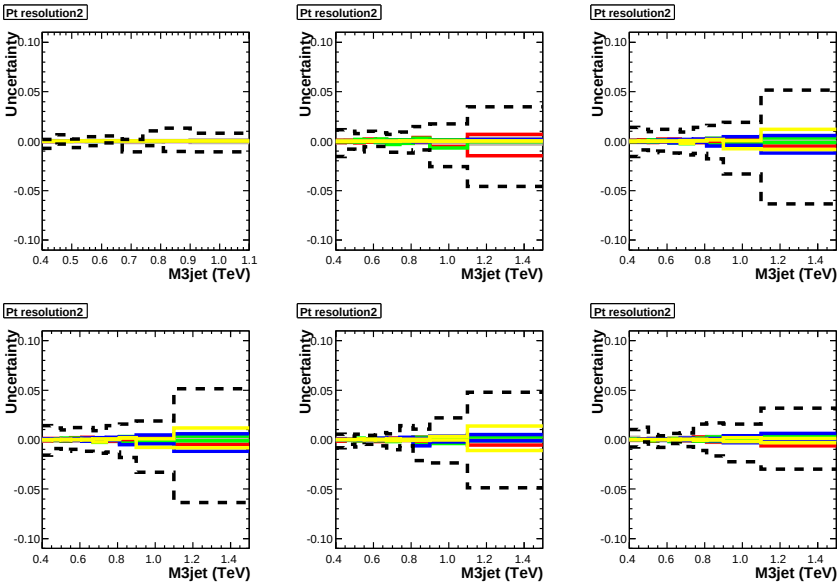

Figure 6.28: Transverse momentum resolution uncertainty (sources 11–15 in Table 6.3). Black dashed line shows the total uncertainty due to transverse momentum resolution with all 15 sources added in quadrature.

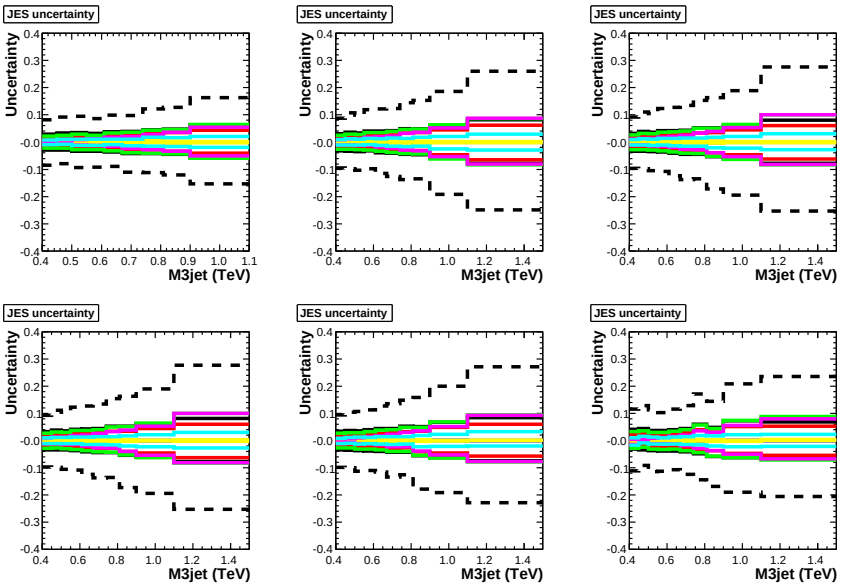

Figure 6.29: JES uncertainty (sources 1–7). Black dashed line shows the total uncertainty due to jet energy scale with all sources added in quadrature.

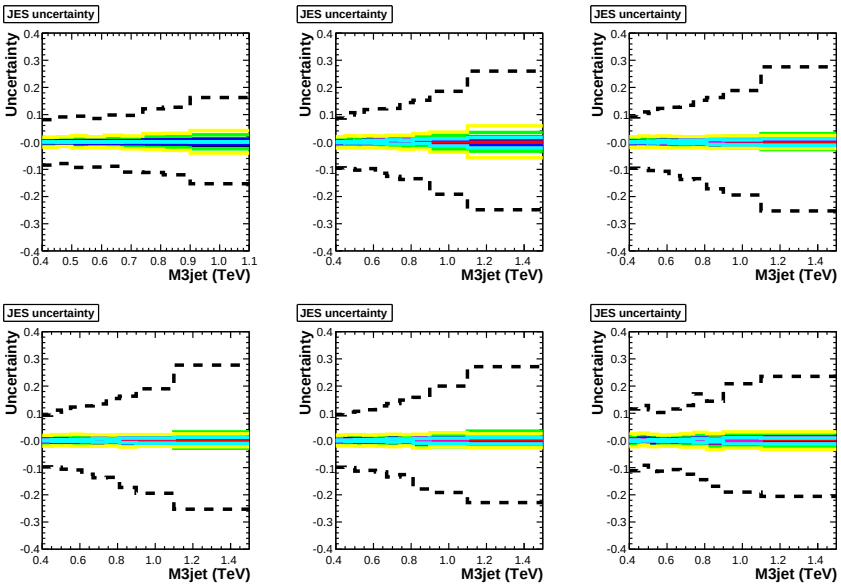

Figure 6.30: JES uncertainty (sources 7–14). Black dashed line shows the total uncertainty due to jet energy scale with all sources added in quadrature.

The dominant systematic uncertainty comes from JES while the second

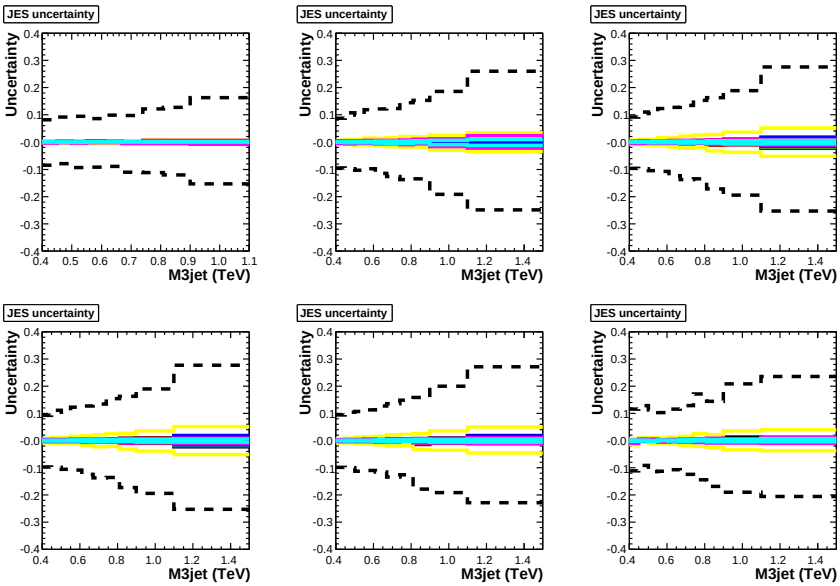

Figure 6.31: JES uncertainty (sources 15–21). Black dashed line shows the total uncertainty due to jet energy scale with all sources added in quadrature.

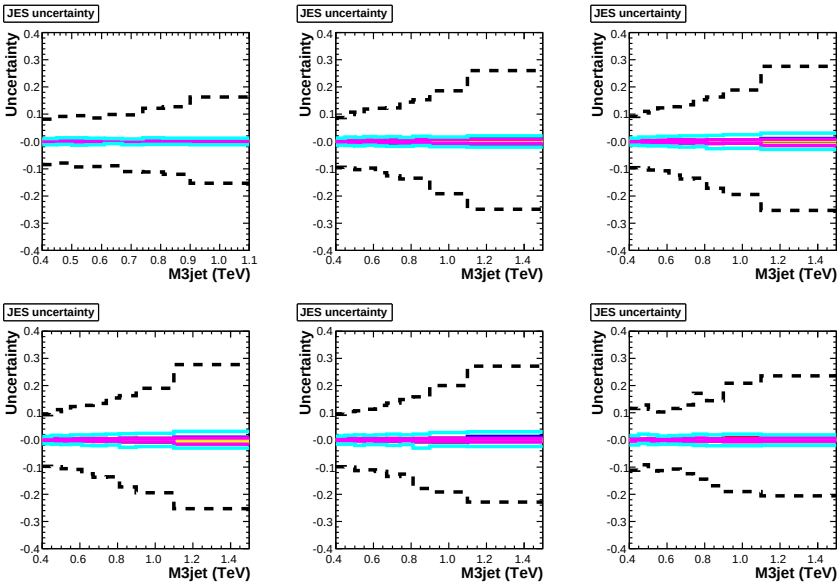

Figure 6.32: JES uncertainty (sources 22–28). Black dashed line shows the total uncertainty due to jet energy scale with all sources added in quadrature.

largest is the one from jet p_T resolution which is comparable with the luminosity uncertainty.

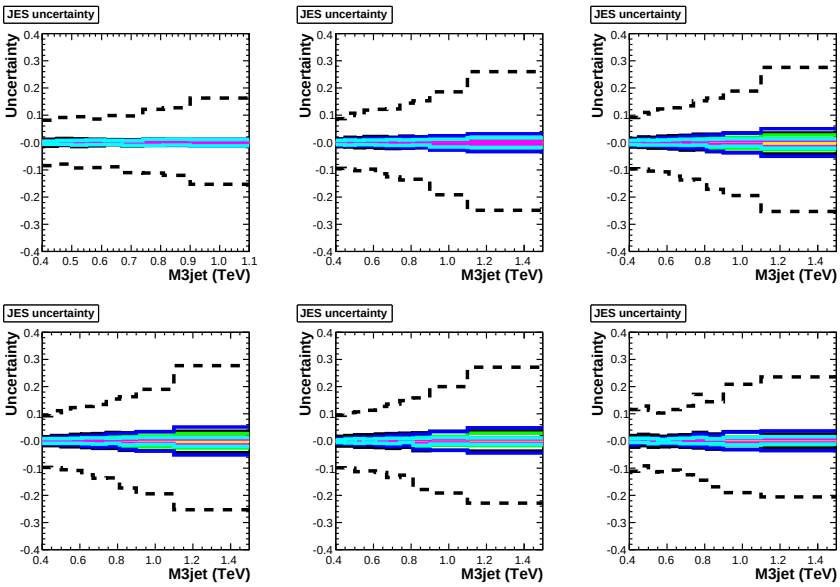

Figure 6.33: JES uncertainty (sources 29–35). Black dashed line shows the total uncertainty due to jet energy scale with all sources added in quadrature.

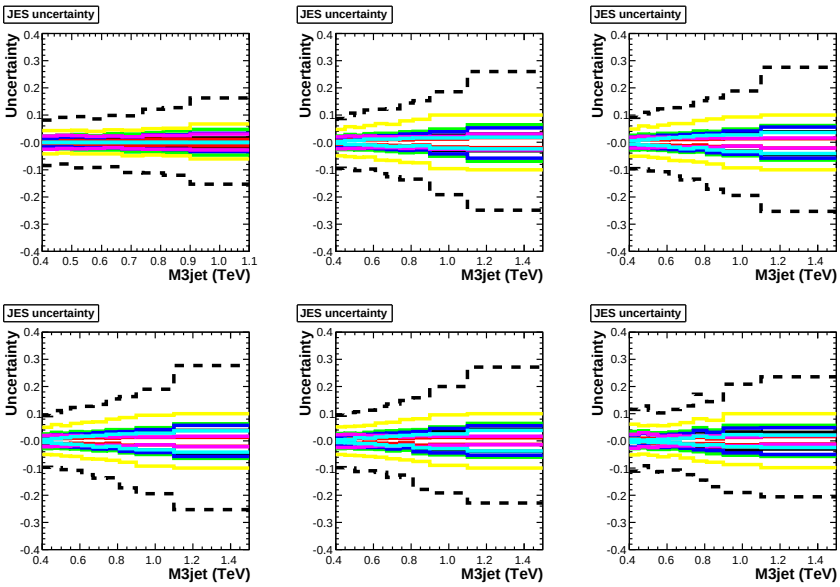

Figure 6.34: JES uncertainty (sources 35–42). Black dashed line shows the total uncertainty due to jet energy scale with all sources added in quadrature.

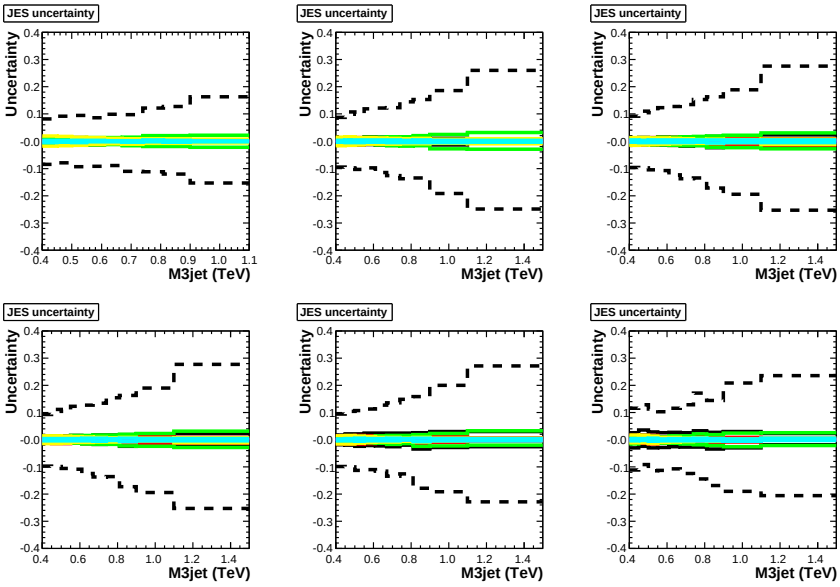

Figure 6.35: JES uncertainty (sources 42–48). Black dashed line shows the total uncertainty due to jet energy scale with all sources added in quadrature.

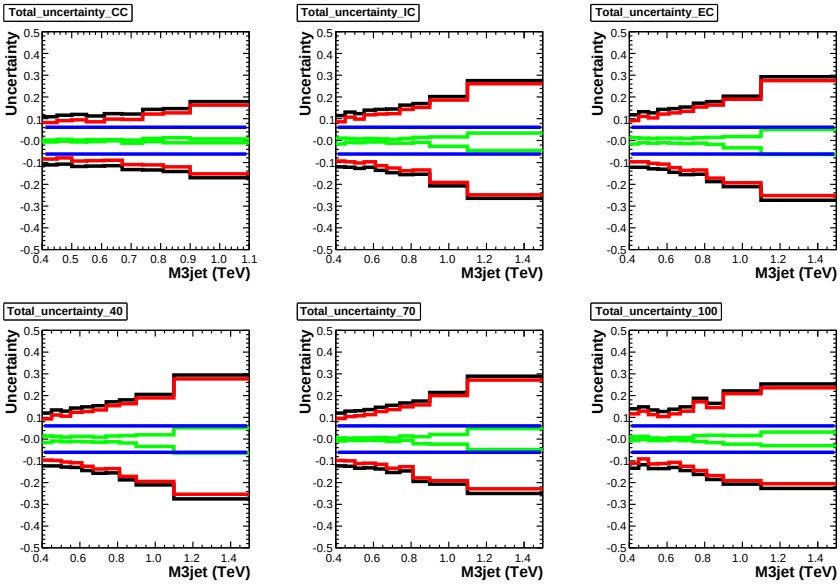

Figure 6.36: Total systematic uncertainty (in black) with three major components. The systematic uncertainty due to the jet energy scale is shown in red, the luminosity uncertainty in blue and the transverse momentum resolution uncertainty in green.

6.11 NLO pQCD Theory Prediction

6.11.1 NLO Calculation

The next-to-leading theory prediction is calculated using NLOJET++ program v4.1.2[35] using the MSTW2008 NLO PDF set[76] (the strong coupling constant value for this set is $\alpha_S(M_Z) = 0.1202$). The PDF uncertainty is estimated by computing the cross section for each of up and down variation of each of 20 eigenvectors in the MSTW2008 90% CL sets. The total PDF uncertainty is computed by adding all variations independently in quadrature. For comparison, the same cross sections were also calculated using the CTEQ6.6 PDF sets[77]. The central value of the cross section from the CTEQ6.6 PDF sets differs up to 40% from the MSTW2008 value. The CTEQ6.6 PDF uncertainty is also larger than the MSTW2008. It is important to note that in the evaluation of the MSTW2008 PDF sets, the same DØ Run II data set was used to constrain the PDF especially at higher values of gluon x.

The pQCD calculation depends on somewhat arbitrary choice of the renormalization and factorization scales. While not theoretically completely motivated it is common to choose both scales to be the same. In case of jet measurements, the scale is usually chosen to be a multiple of the (average) jet transverse momentum $\mu = \kappa p_T$. For the three-jet cross section calculation, the renormalization and factorization scales are chosen to be the same and equal to

$$\mu = \mu_r = \mu_f = p_T^{\text{avg}} = \frac{1}{3}\sum_{\text{jet}=1}^{3} p_T^{\text{jet}}. \tag{6.28}$$

The uncertainty due to scale dependence is calculated by varying the scale up and down by a factor of 2. For additional comparison, other scales (μ_0–μ_3) were investigated.

- $\mu_0 = \frac{1}{3}\sum_{\text{jet}=1}^{3} p_T^{\text{jet}}$;
- $\mu_1 = \frac{2}{3}\sum_{\text{jet}=1}^{3} p_T^{\text{jet}}$;
- $\mu_2 = \frac{1}{2}\sum_{\text{jet}=1}^{3} p_T^{\text{jet}}$;
- $\mu_3 = p_T^{\text{max}}$ (leading jet p_T).

The ratios of the NLO cross section calculated at scales μ_0–μ_3 is presented in Fig. 6.41, scale μ_0 is used for the final result (Eq. 6.28).

While the cross section can be calculated at the NLO order using the DØ Run II cone algorithm, it is not certain if the cross section is IR or collinear safe at this order due to properties of this algorithm. Potentially,

the NNLO correction (if it could be calculated) can be of the same order as the NLO itself rendering the result meaningless at NLO (or at maximum, valid at the LO order precision only). This could be only judged by testing the algorithm difference for example between the DØ Run II cone algorithm and the Seedless Infrared Safe Cone algorithm (SISCone[46]) at the NNLO order (or at least in a parton shower Monte Carlo model which can simulate the multiparton production of NNLO complexity) to test the difference in the cross section prediction by the two algorithms. For interest (but without the power to judge the result) the same NLO cross section was computed with the use of SISCone algorithm. At the NLO level of NLOJET++, the cross section differs only by about 2–3% and similar scale dependence of the result has been observed.

Figure 6.37 shows the cross section ratio at NLO for the DØ Run II algorithm with MSTW2008 and CTEQ6.6 PDF sets showing the difference in the central values. Figure 6.38 shows the total uncertainty coming from the 20 eigenvectors from the MSTW2008 sets while Fig. 6.39 shows the total uncertainty from 22 CTEQ6.6 eigenvectors. The size of the MSTW PDF uncertainty is smaller than the CTEQ one due to the fact that MSTW2008 is already using precise Tevatron Run II data in the PDF fit. Figure 6.40 shows the scale dependence by varying the central scale from Eq. 6.28 up and down by a factor of 2. The NLOJET++ calculation of the cross section at NLO order using the DØ Run II cone algorithm and SISCone algorithm is shown in the Fig. 6.42

6.11.2 Nonperturbative Corrections

Two nonperturbative corrections were obtained using the Pythia Monte Carlo generator. One contains the correction due to underlying event, the other due to hadronization. The total nonperturbative correction factor is obtained by multiplying those two together. The two effects almost cancel each other. Figure 6.43 shows the nonperturbative corrections. To reduce statistical fluctuations, the nonperturbative correction is fitted with a linear function which is then used in the analysis (Fig. 6.44).

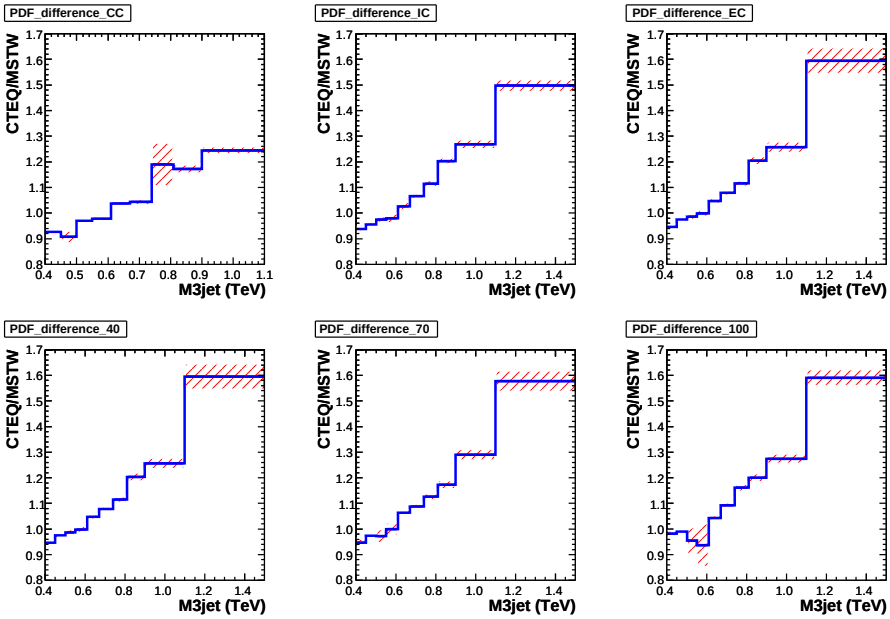

Figure 6.37: The ratios of the three-jet cross section calculations from NLO-JET++ using two different PDF sets (MSTW2008, CTEQ6.6) in 6 regions of the analysis. The shadings correspond to statistical uncertainties.

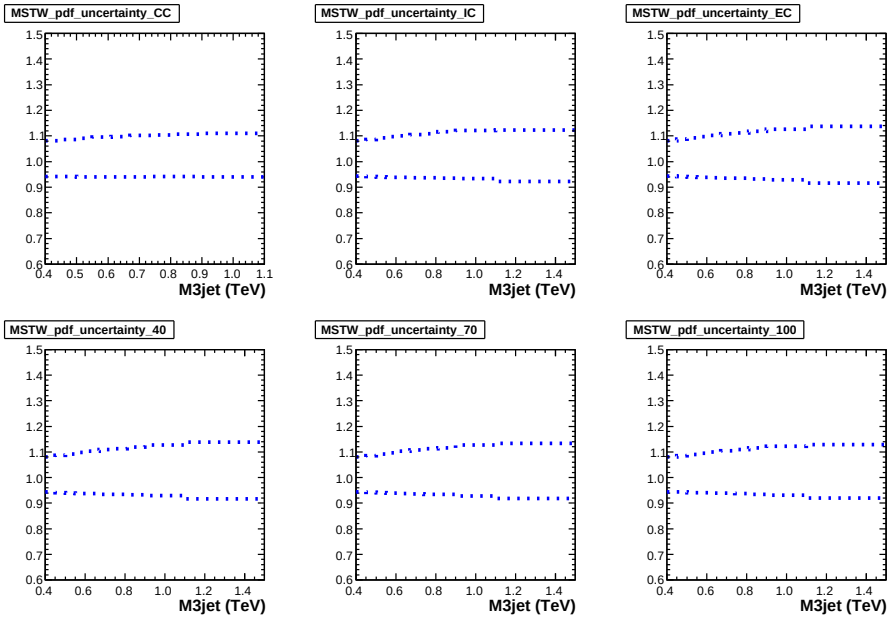

Figure 6.38: The PDF uncertainty of the NLO cross section coming from the 20 MSTW2008 PDF 90% CL eigenvectors.

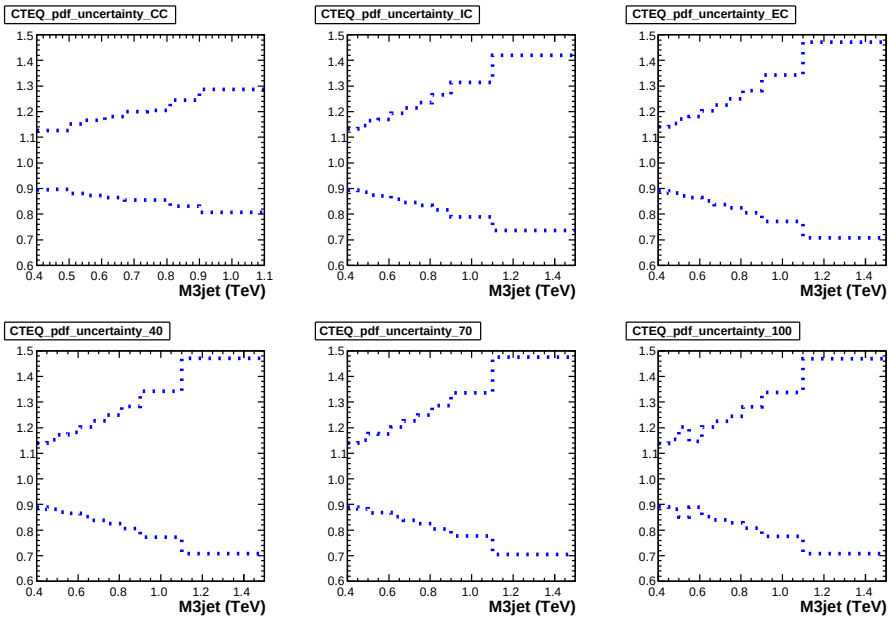

Figure 6.39: The PDF uncertainty of the NLO cross section coming from the 22 CTEQ6.6 PDF eigenvectors.

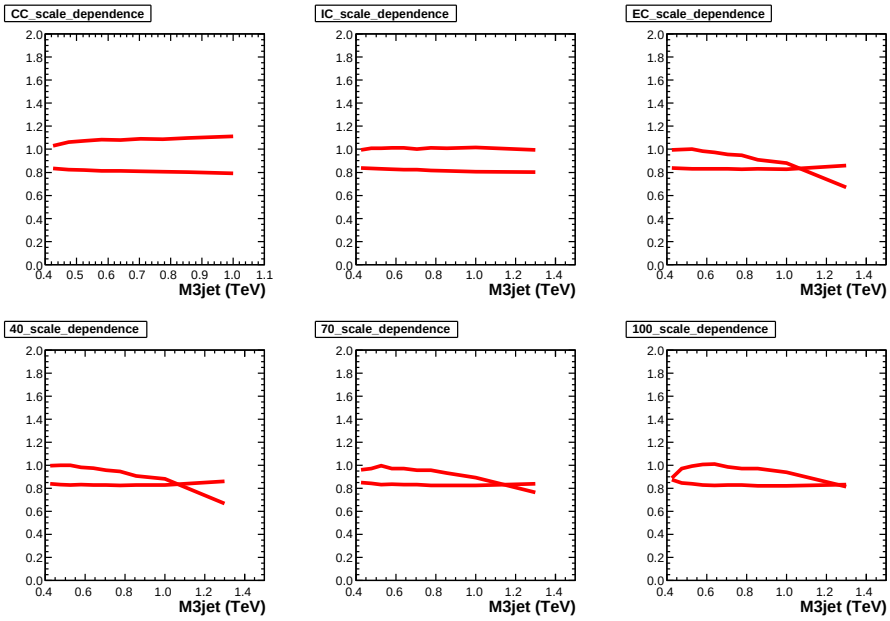

Figure 6.40: The scale dependence of the cross section (calculated with MSTW2008 PDFs) estimated by varying the scale $\mu = \mu_r = \mu_f = 1/3(p_T^1 + p_T^2 + p_T^3)$ up and down by a factor of 2.

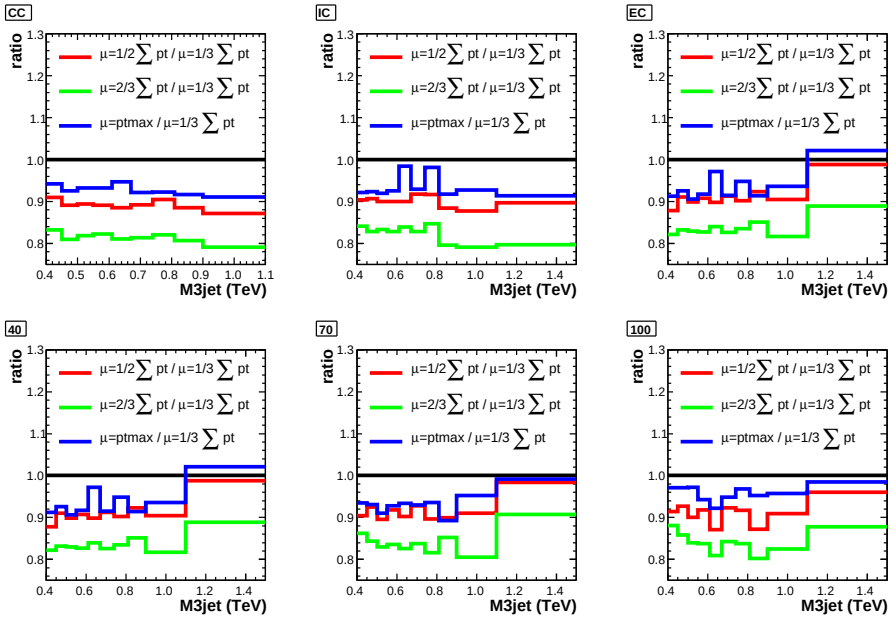

Figure 6.41: The ratios of NLO cross sections calculated with four different choices of the renormalization and hadronization scales.

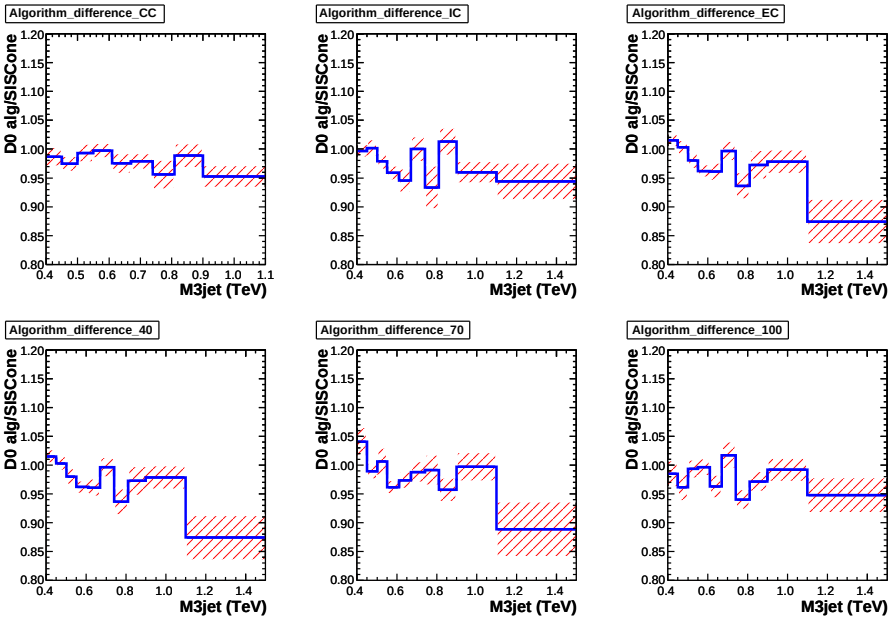

Figure 6.42: The ratios of the cross sections calculated with the DØ Run II Cone and the SISCone jet algorithms at the NLO level. The shaded areas correspond to statistical uncertainty.

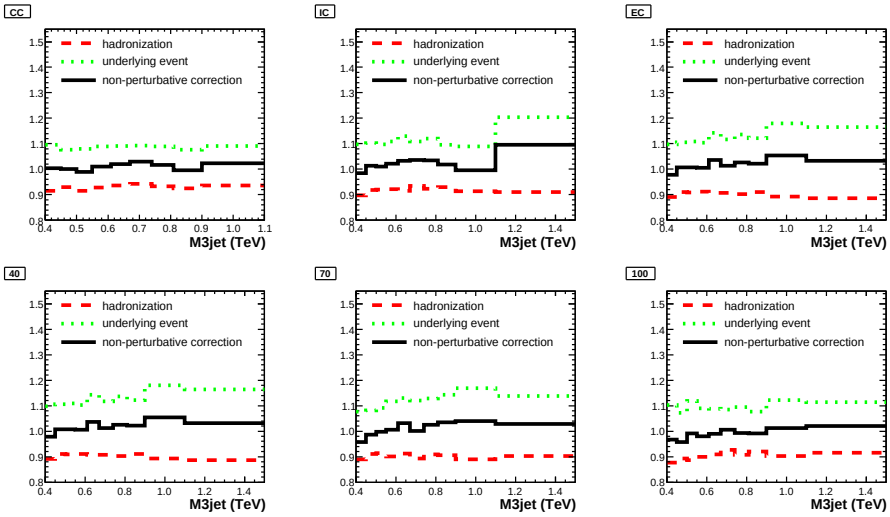

Figure 6.43: Summary of nonperturbative corrections due to underlying event and hadronization. The total correction is the product of both.

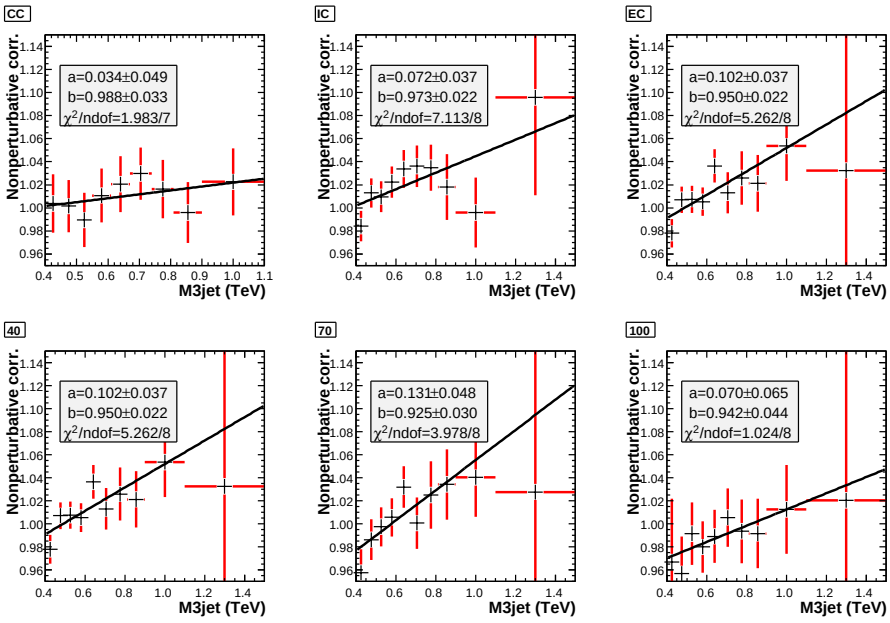

Figure 6.44: Total nonperturbative correction fit with a linear function.

6.12 Final result

The master formula for the three-jet mass cross section is given in Eq. 6.29.

$$\frac{\mathrm{d}\sigma}{\mathrm{d}M_{3\mathrm{jet}}} = \frac{1}{\mathcal{L} \cdot \Delta M_{3\mathrm{jet}}} \cdot \left(\sum_{i=1}^{N_{\mathrm{evt}}} \frac{1}{\epsilon_{\mathrm{v}}^{i}} \right) \cdot C_{\mathrm{unsmear}}. \tag{6.29}$$

Where $\mathcal{L}$ is the luminosity, $\epsilon_{\mathrm{v}}^{i}$ is the vertex efficiency applied using event-by-event weights (a function of instantaneous luminosity, the mean value is $\sim 92\%$), $\Delta M_{3\mathrm{jet}}$ is the bin width and C_{unsmear} is the unsmearing correction factor obtained from d0jetsim. The mass in the equation corresponds to the rescaled mass (Eq. 6.13).

The cross section is calculated in six regions. For the rapidity dependence, the cross section is calculated in CC ($|y| < 0.8$), IC ($|y| < 1.6$) and EC ($|y| < 2.4$) regions, the result is shown in Fig. 6.45. For the dependence on the third jet transverse momentum, it is calculated in 40 ($p_{T3} > 40\,\mathrm{GeV}$), 70 ($p_{T3} > 70\,\mathrm{GeV}$) and 100 ($p_{T3} > 100\,\mathrm{GeV}$) regions and the result is shown in Fig. 6.46. The data over theory ratio is presented in Fig. 6.47. The cross sections, event yields, statistical, systematic errors, theory predictions and nonperturbative corrections are summarized in Tables B.1–B.6.

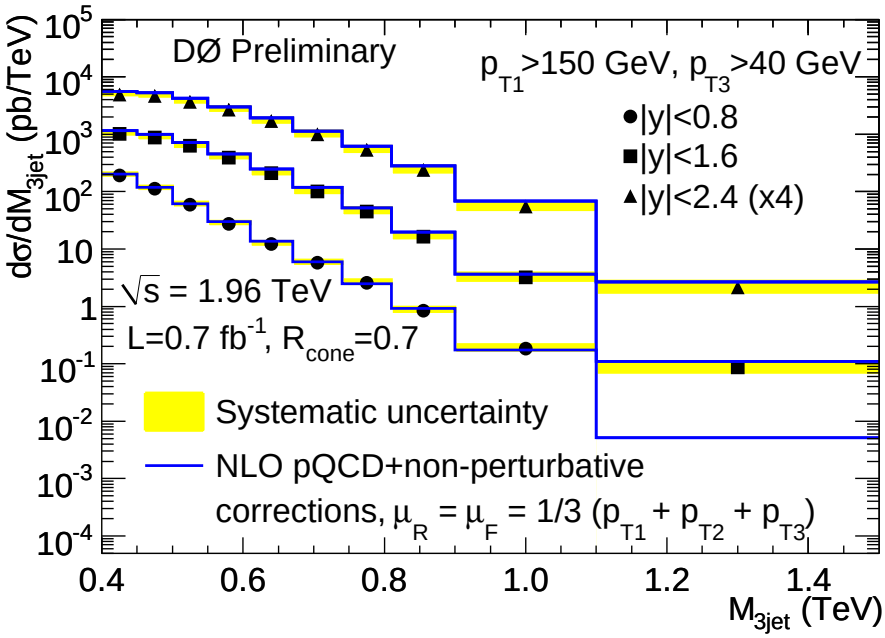

Figure 6.45: Differential inclusive three-jet cross section as a function of the invariant three-jet mass in regions of jet rapidities. The $|y| < 2.4$ region is scaled by a factor of 4 for readability. Systematic uncertainty is shown by a shaded band. Full lines correspond to the NLO calculations with NLOJET++ and MSTW2008 PDFs. No events are found in the highest $M_{3\text{jet}}$ bin in the $|y| < 0.8$ region.

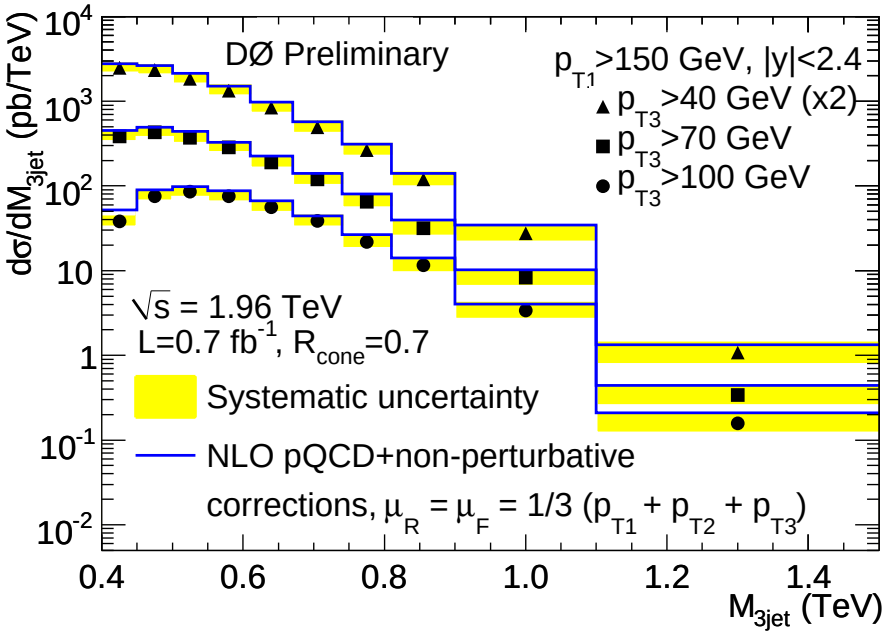

Figure 6.46: Differential inclusive three-jet cross section as a function of the invariant three-jet mass in regions of the third jet transverse momentum. The $p_{T3} > 40\,\text{GeV}$ region is scaled by a factor of 2 for readability. Systematic uncertainty is shown by a shaded band. Full lines correspond to the NLO calculations with NLOJET++ and MSTW2008 PDFs.

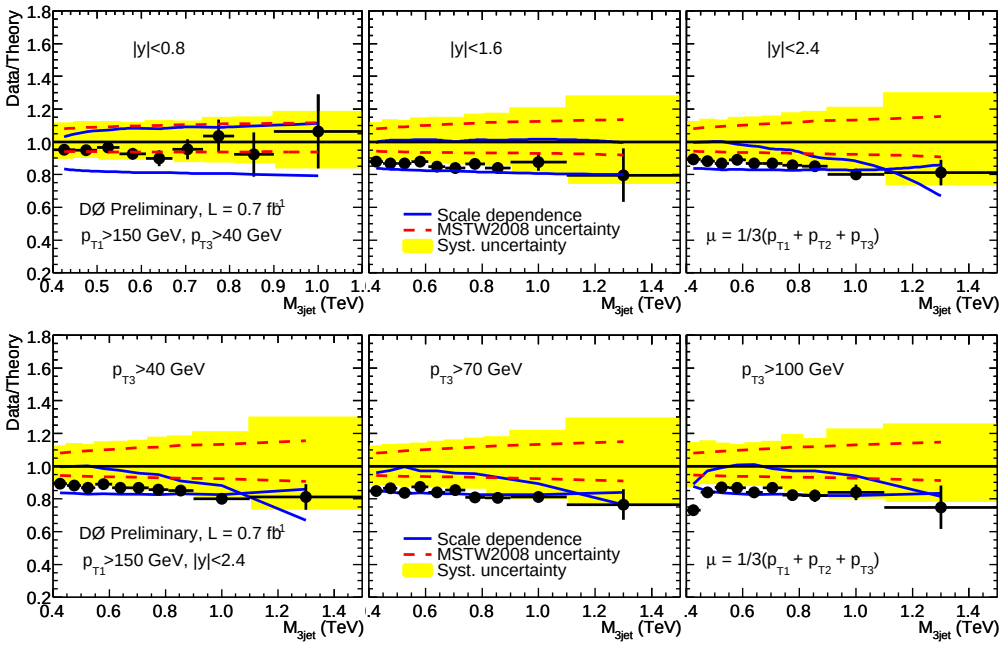

Figure 6.47: Data to theory ratio in all analysis regions. Top three plots correspond to three rapidity regions, bottom three correspond to three regions of the third jet transverse momentum. The total systematic uncertainty is shown by a shaded region. The PDF uncertainty comes from the 20 MSTW2008 NLO 90% CL eigenvectors. The scale uncertainty is determined by varying the scale up and down by a factor of 2.

7 Summary and Conclusion

This thesis presents the measurement of the inclusive three-jet cross section as a function of the invariant three-jet mass in three regions of jet rapidities and three regions of the third jet transverse momenta. The measurement is relevant in the context of perturbative Quantum chromodynamics (pQCD) where the matrix element for the production process is calculated at the next-to-leading order. Jet measurements in general contribute to our understanding of the proton structure (parton distribution functions), strong force dynamics (QCD at higher orders, running of the strong coupling constant α_{S}), and help to understand the backgrounds in searches for new physics beyond the Standard Model.

After an introduction, the thesis begins with a brief description of the Standard Model of elementary particles and a basic introduction to Quantum chromodynamics which leads to a definition of the concept of jet. In the next chapter, the definition of a jet algorithm is presented with details relevant to the DØ Run II midpoint cone algorithm. The chapter also discusses some of the latest progress in the jet algorithms. The fourth chapter describes the DØ detector where the data used in this thesis were collected. Chapter 5 details the jet energy scale calibration. The jet energy scale group at the DØ experiment achieved a remarkable precision in the jet energy calibration at hadron–hadron colliders where across a large part of a phase space the uncertainty is smaller than 2%. This in turn significantly reduces the total systematic uncertainty of many jet measurements. The final chapter before this summary then present the main topic of the thesis, namely the measurement of the three-jet cross section.

In the measurement, the production cross section of inclusive three-jet final states is studied on a sample with an integrated luminosity of $0.7\,\mathrm{fb}^{-1}$ collected by the DØ experiment between years 2002 and 2006. Generally, high transverse momentum cuts are set on the selected three-jet to study mainly the hard emission of jets and also to reduce the effect of worse transverse momentum resolution and larger jet energy scale uncertainty connected with lower transverse momentum jets. Also, large angular separation between all

selected jets is required to reduce potential sensitivity to jet algorithm details, namely the splitting/merging procedure. The differential inclusive three-jet cross section is then studied in three regions of jet rapidities (Fig. 6.45) and in three regions of the softest (third) jet transverse momentum (Fig. 6.46) as a function of the invariant three-jet mass.

The unsmearing coefficients which enable to present the cross section corrected of all detector related issues (and therefore making the result useful to other/future experiments) were derived using a parameterized jet simulation based on events generated with SHERPA Monte Carlo generator. After a small reweighting a good agreement is found between this LO $2 \to N$ generator while generally the LO $2 \to 2$ with parton shower simulations failed to describe the data.

The theory prediction is calculated using the NLOJET++ program at the next-to-leading order. The nonperturbative corrections for underlying event and for hadronization were estimated using PYTHIA Monte Carlo generator. The latest parton distribution function sets of MSTW2008 and CTEQ6.6 are used in the calculation.

In summary, this thesis presents the first measurement of the inclusive three-jet cross section in Run II of the Fermilab Tevatron Collider. Perturbative QCD provides a reasonable description of the data in all six presented regions (Fig. 6.47). No obvious signs of new physics are seen in this particular channel.

There are several ways to extend this analysis. The obvious one is to extend the dataset used to the dataset collected by the DØ experiment. Due to continuous improvement on the accelerator side, the experiment has already collected a dataset of an integrated luminosity of $7\,\mathrm{fb}^{-1}$ as of February 2010 (i.e. ten times larger than the one used in this analysis) which will reduce the statistical uncertainty by a factor of 3. The changes in the detector, trigger and reconstruction algorithms for the Run IIb data taking period would make what looks like an easy step somewhat complicated task. Another direction of extending the result is to make use of lower inclusive jet triggers which would enable reducing the leading jet transverse momentum cut and therefore expanding the available phase space. Third, but maybe the most interesting would be to investigate also the other three-jet system variables like X_3 and X_4 and angles as described in Sec. 6.2.

So, in the immortal words of Bugs Bunny, that's all folks![78].

A Control plots

A set of control variables is chosen to show the agreement between the simulated events and data. The generated particle level events are smeared by the known resolutions and compared with the real (smeared) data events. The simulated events are reweighted as described in Sec. 6.9.

The following variables were chosen:

- Primary vertex z-distribution;
- Leading jet transverse momentum;
- Second leading jet transverse momentum;
- Third leading jet transverse momentum;
- Absolute value of the leading jet rapidity;
- Absolute value of the second leading jet rapidity;
- Absolute value of the third leading jet rapidity;
- Minimum distance between all three jets $\mathrm{d}R_{\mathrm{min}}$;
- Ratio of the fourth jet transverse momentum to the third jet (transverse momentum cut on the fourth jet $p_T^4 \geq 25\,\mathrm{GeV}$ and no rapidity cut on the fourth jet);
- Absolute value of the fourth jet rapidity (if present, same cuts as above);
- The rescaled three-jet mass $RM_{3\mathrm{jet}}$ defined in Eq. 6.13.

Each control variable (except the three-jet mass) is divided into low (left column) and high mass (right column) regions to show the agreement at both sides of the spectra. For each control plot, two sets of figures is presented. First corresponds to the three regions of rapidity dependence (CC, IC and EC corresponding to $|y| < 0.8$, $|y| < 1.6$ and $|y| < 2.4$. Second corresponds to

the three regions of third jet transverse momentum dependence (40, 70 and 100 which mean $p_{T3} > 40$, 70 or 100 GeV. The low mass region corresponds to rescaled masses between 400 and 670 GeV, the high mass region is above 670 GeV. Data are shown with blue markers, simulation as red histograms.

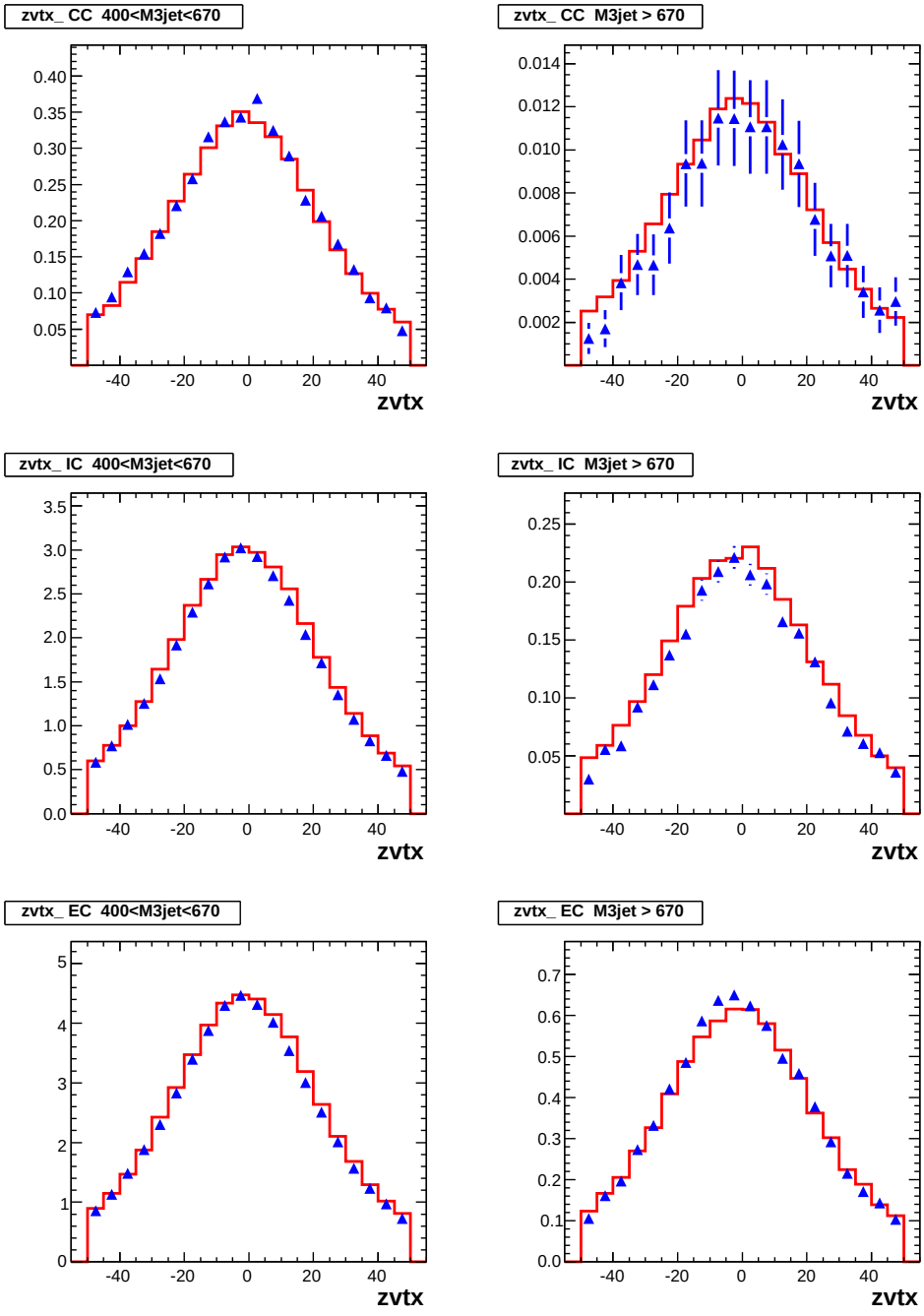

Figure A.1: z-vertex coordinate control plot 1.

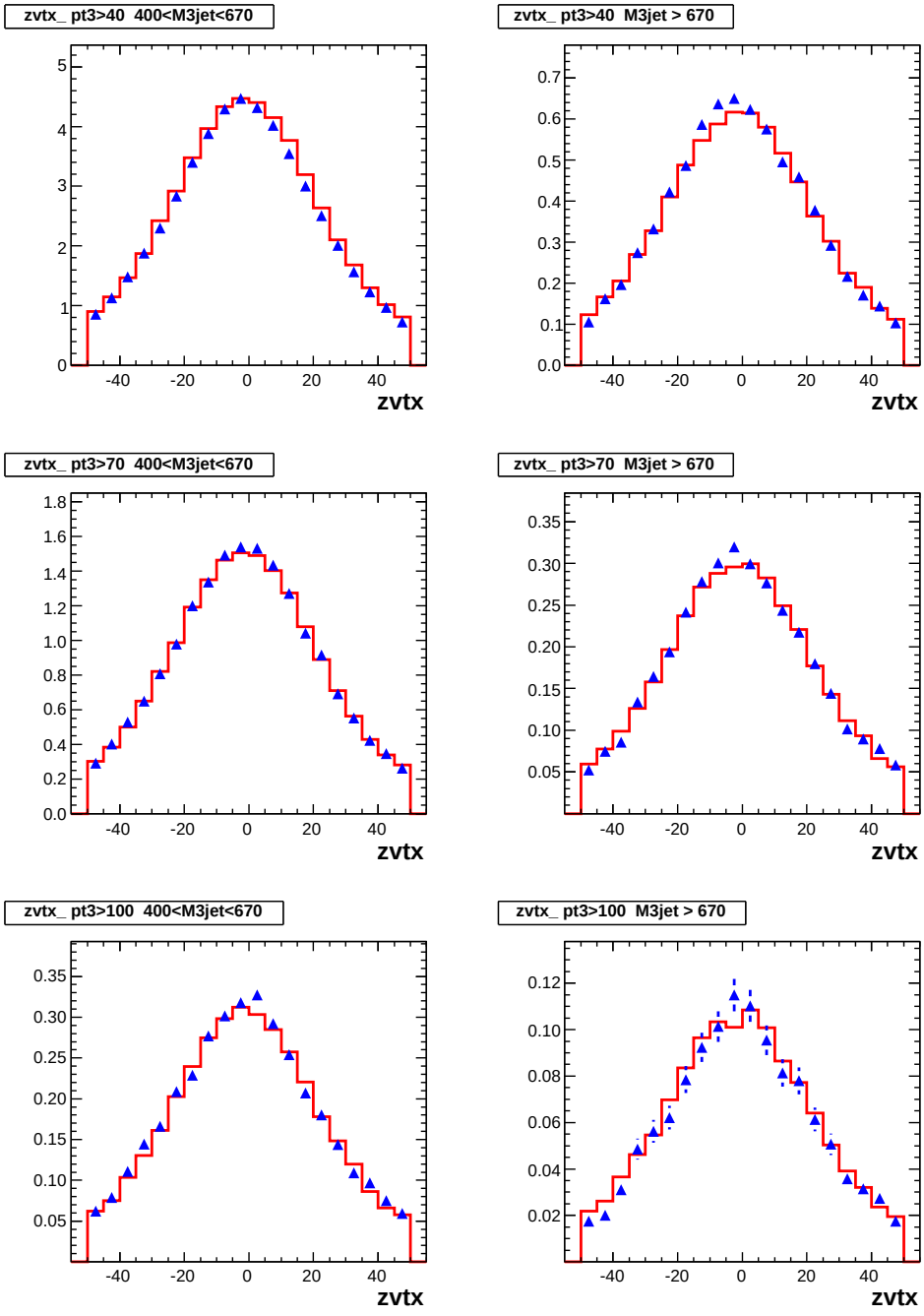

Figure A.2: z-vertex coordinate control plot 2.

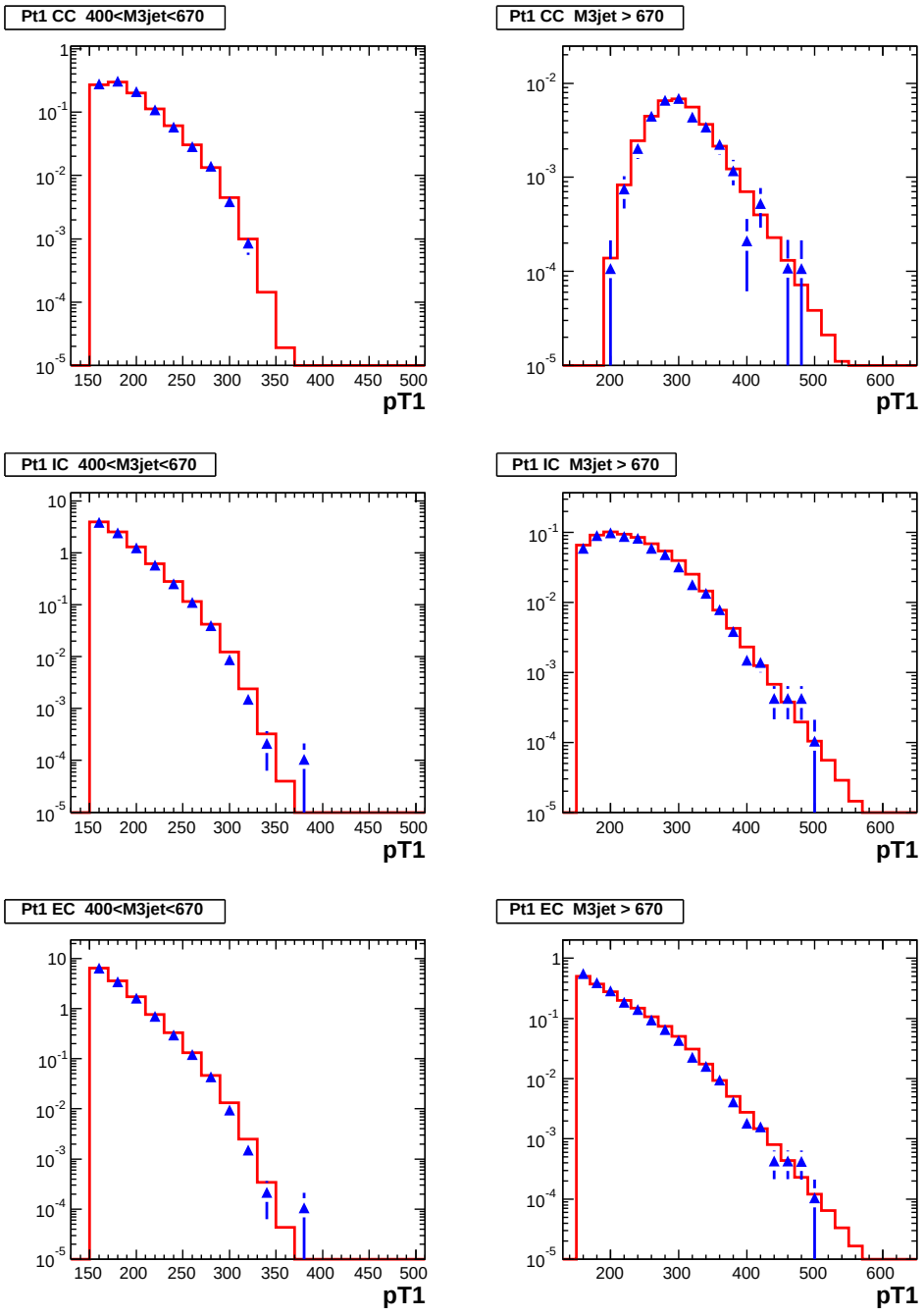

Figure A.3: Leading jet transverse momentum control plot 1.

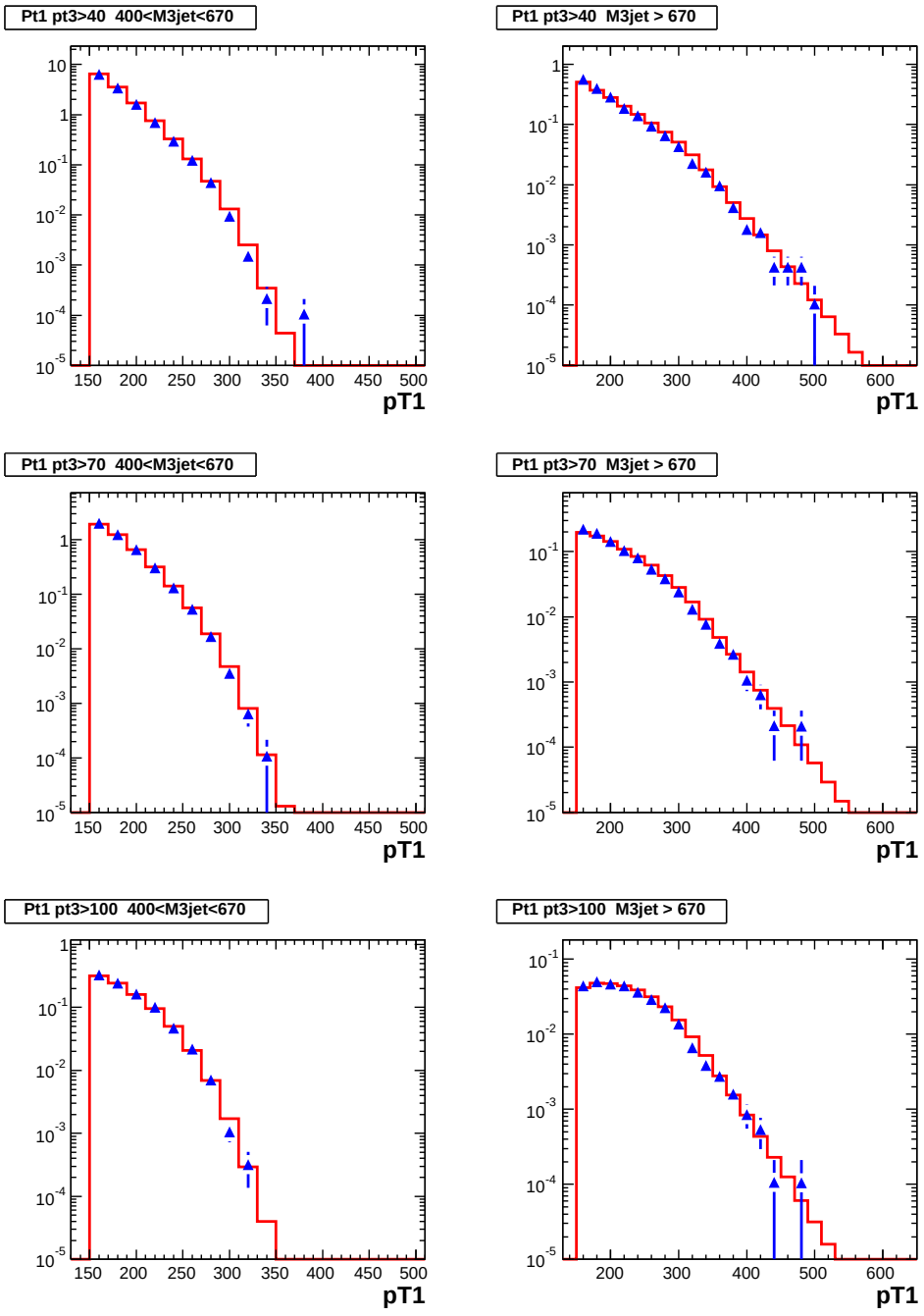

Figure A.4: Leading jet transverse momentum control plot 2.

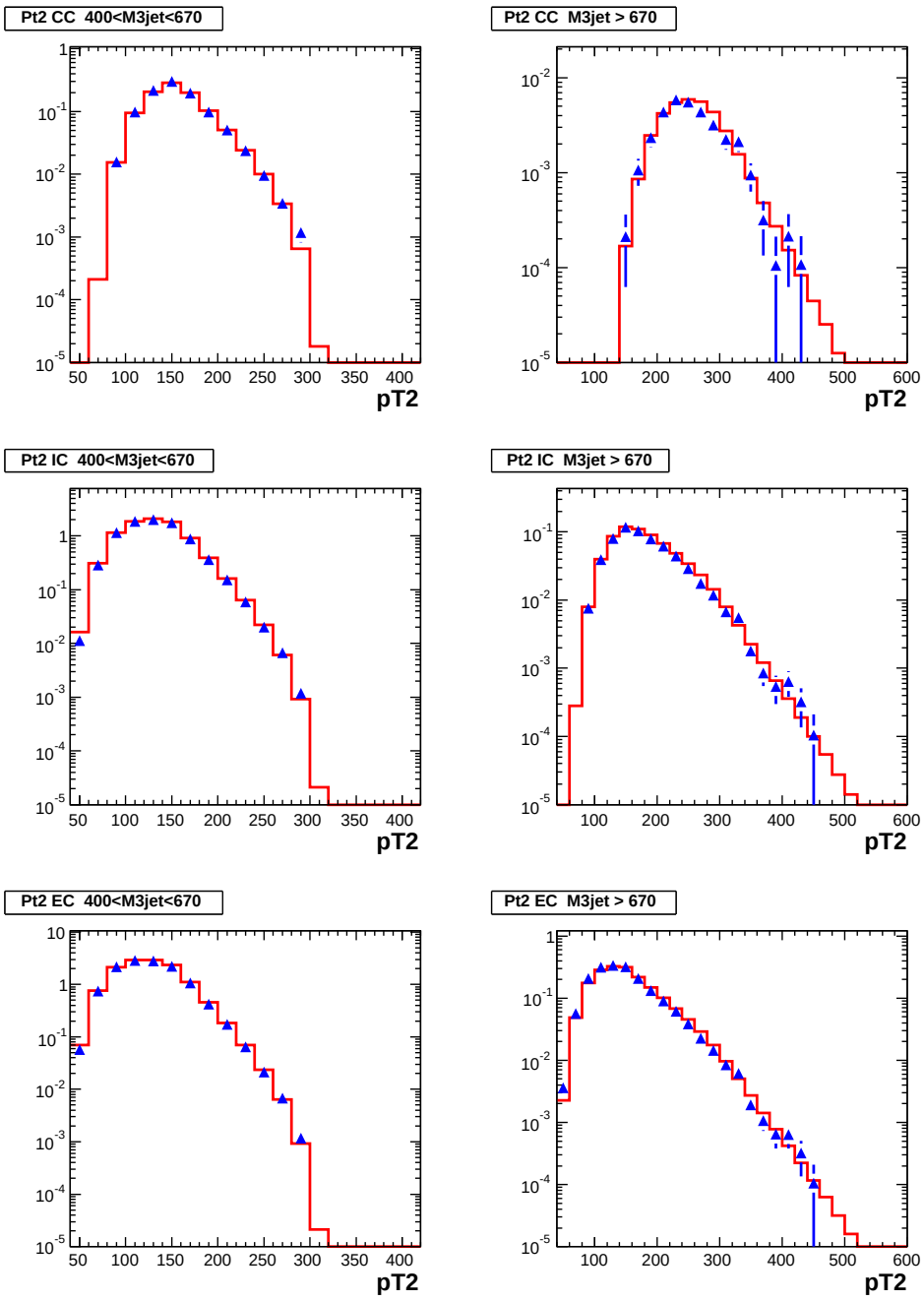

Figure A.5: Second leading jet transverse momentum control plot 1.

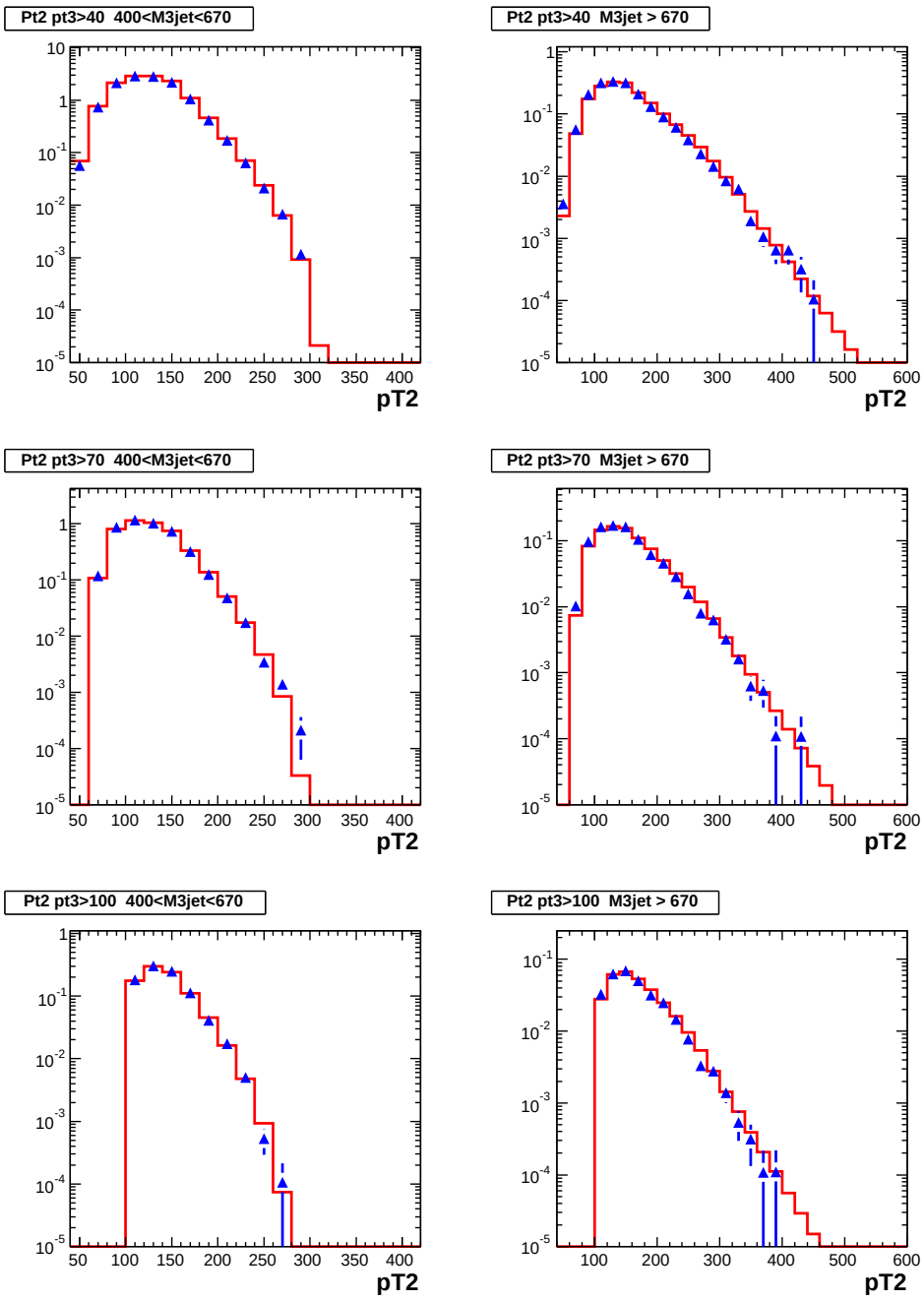

Figure A.6: Second leading jet transverse momentum control plot 2.

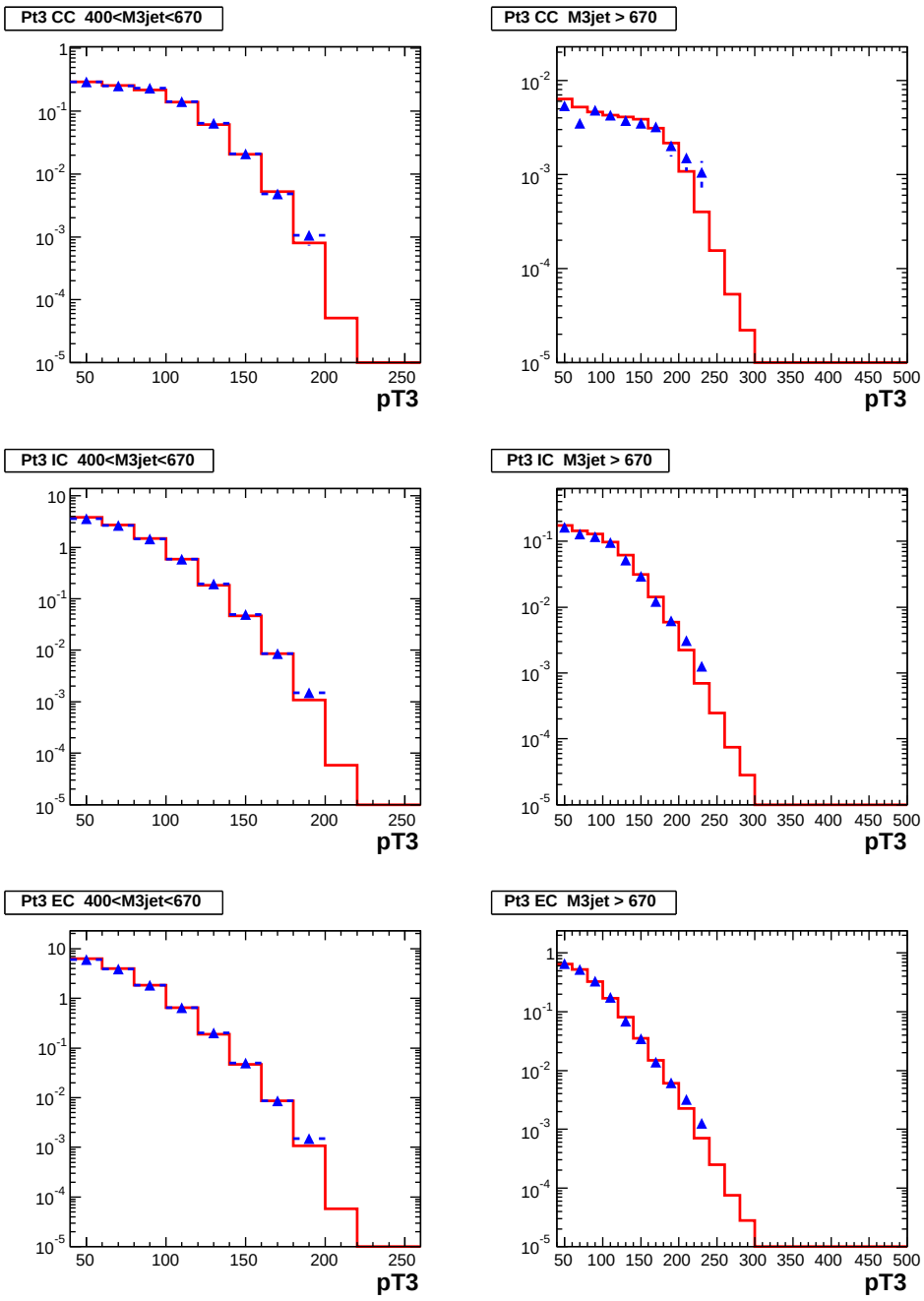

Figure A.7: Third leading jet transverse momentum control plot 1.

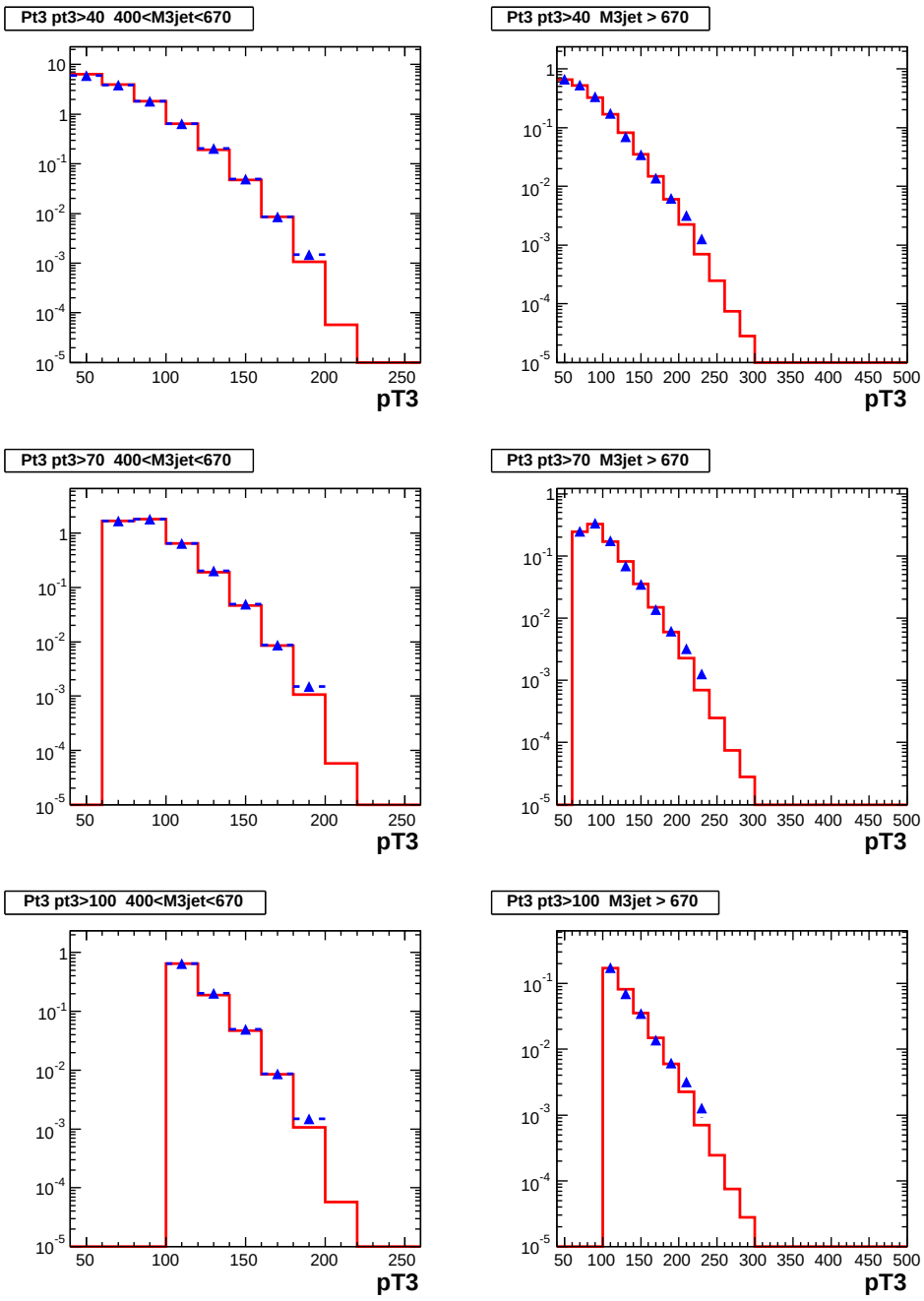

Figure A.8: Third leading jet transverse momentum control plot 2.

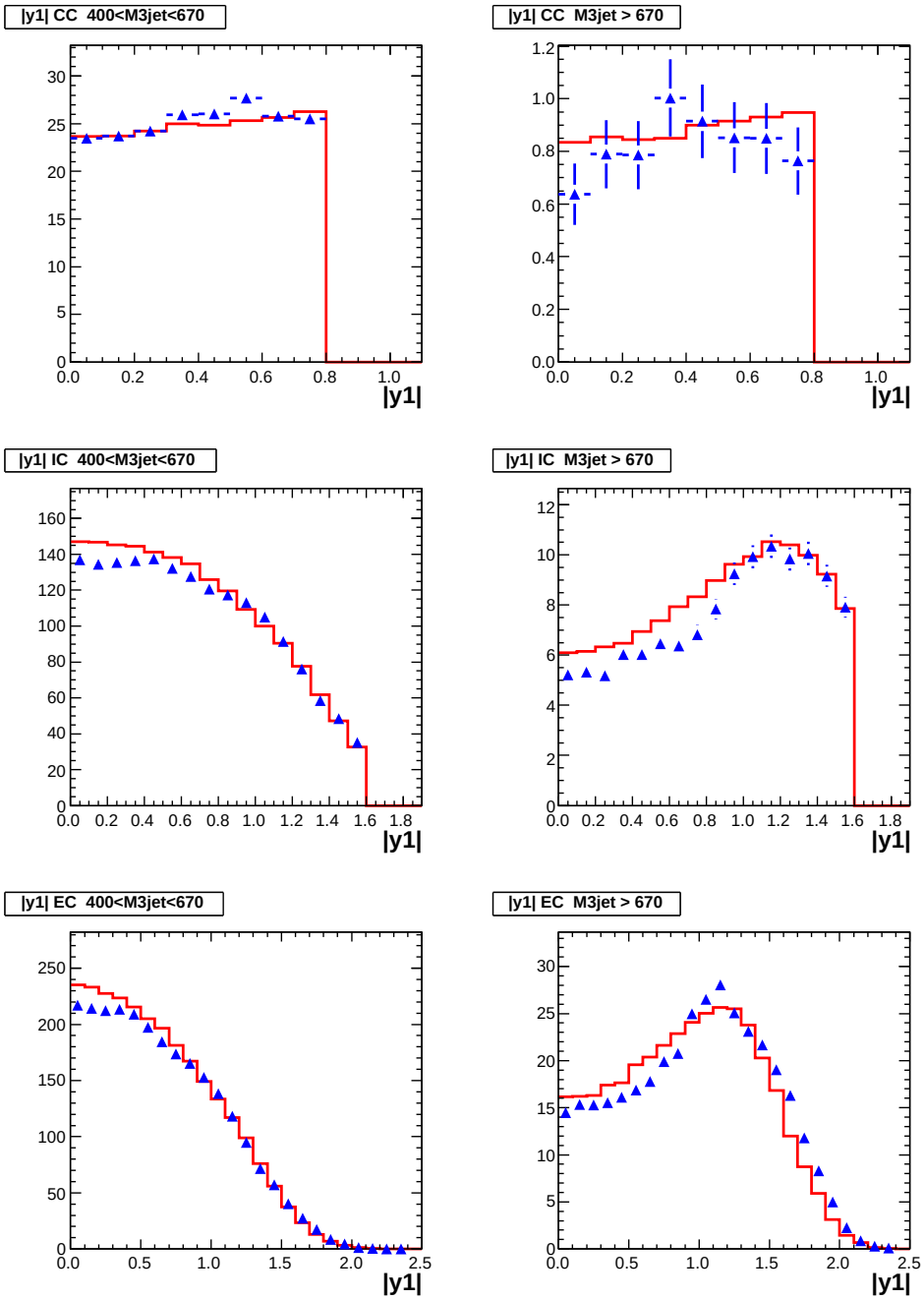

Figure A.9: Leading jet rapidity control plot 1.

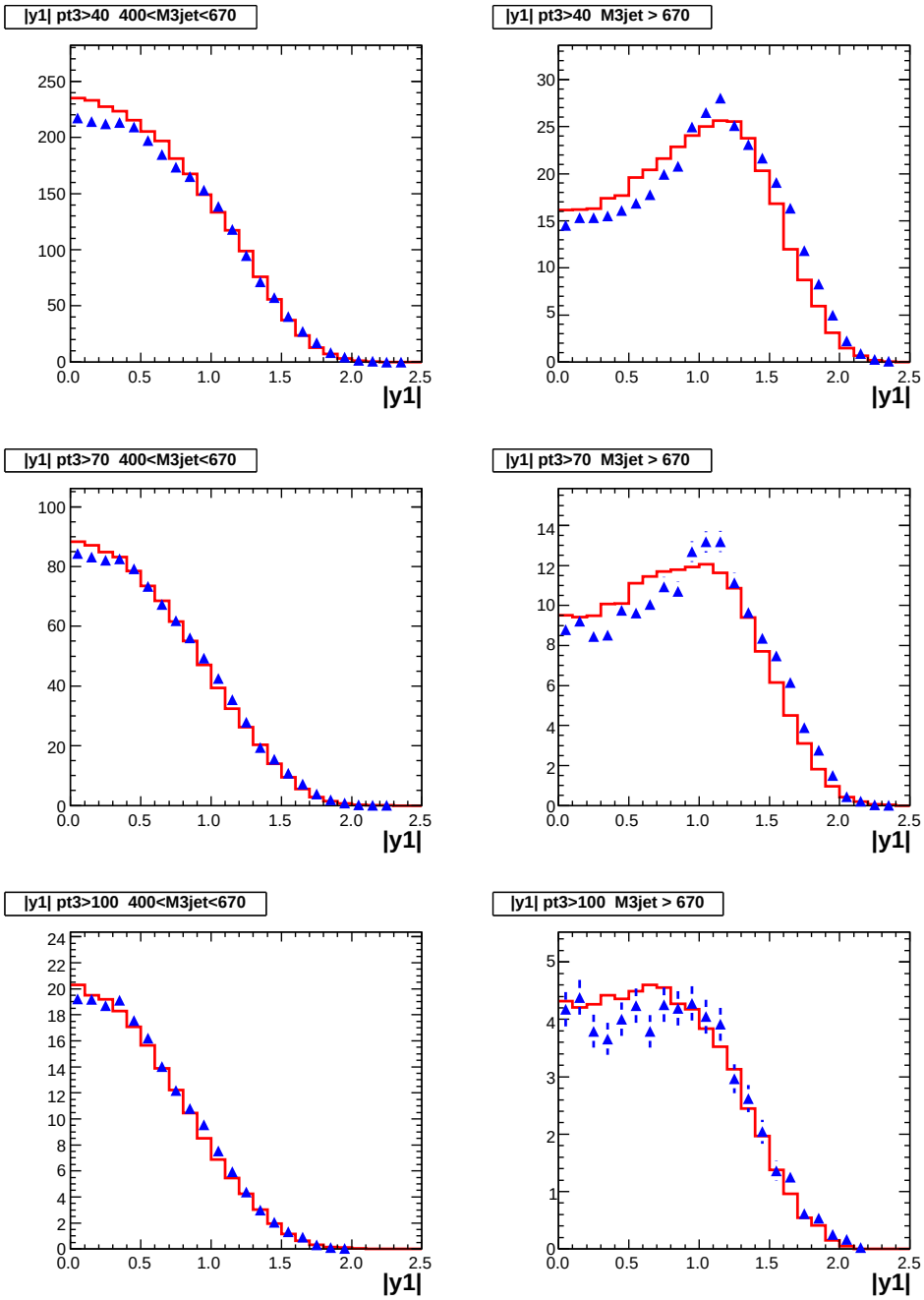

Figure A.10: Leading jet rapidity control plot 2.

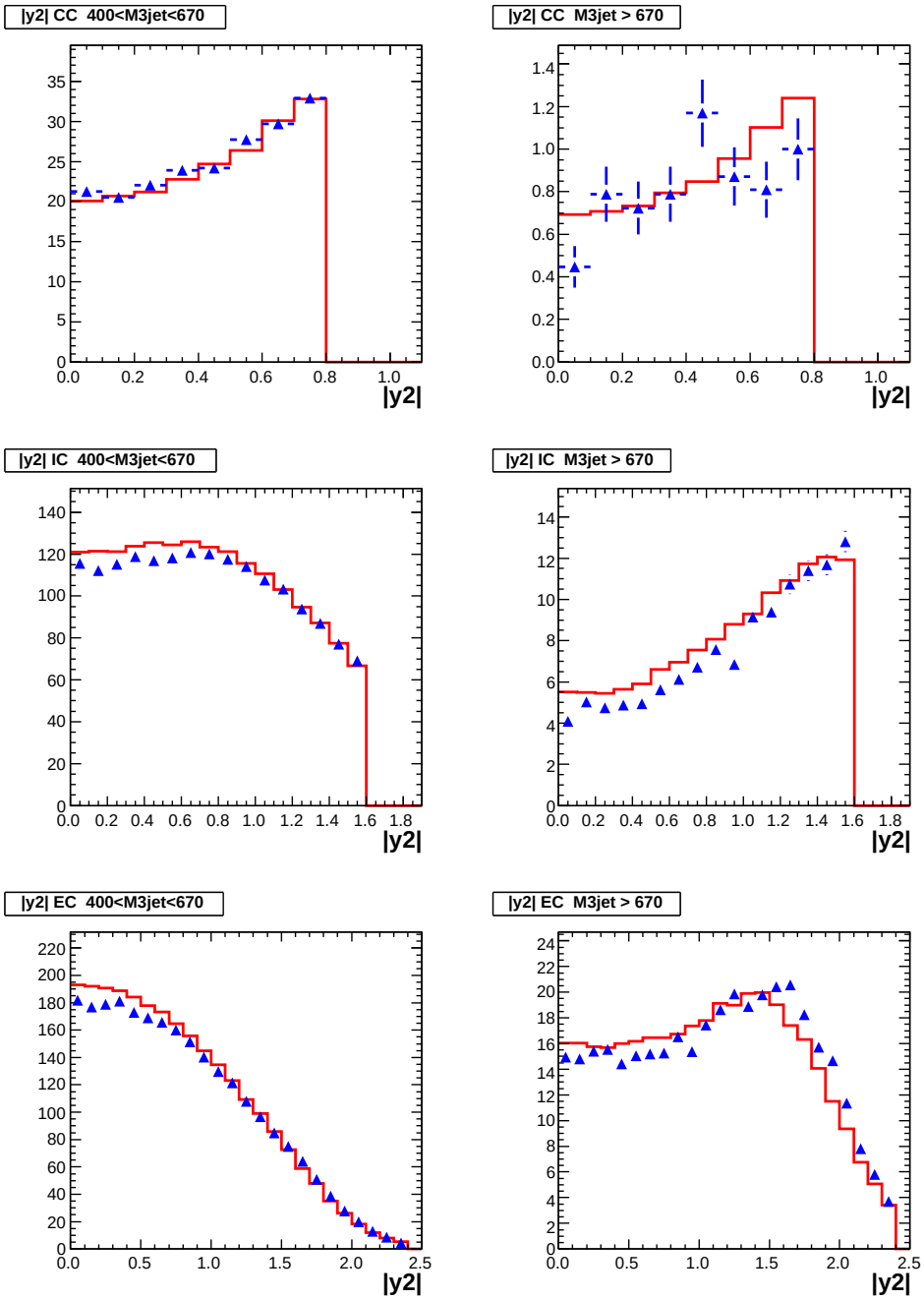

Figure A.11: Second leading jet rapidity control plot 1.

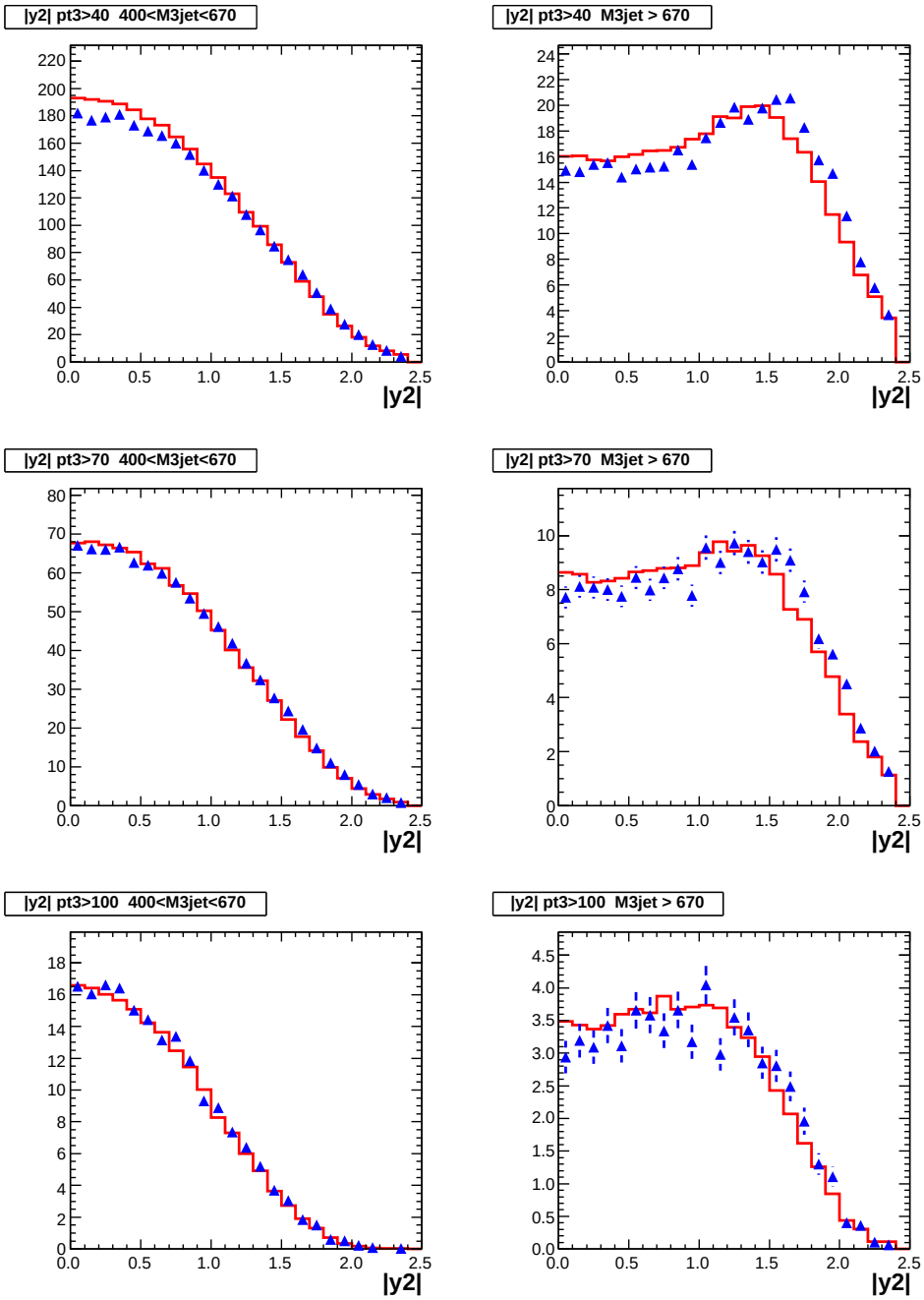

Figure A.12: Second leading jet rapidity control plot 2.

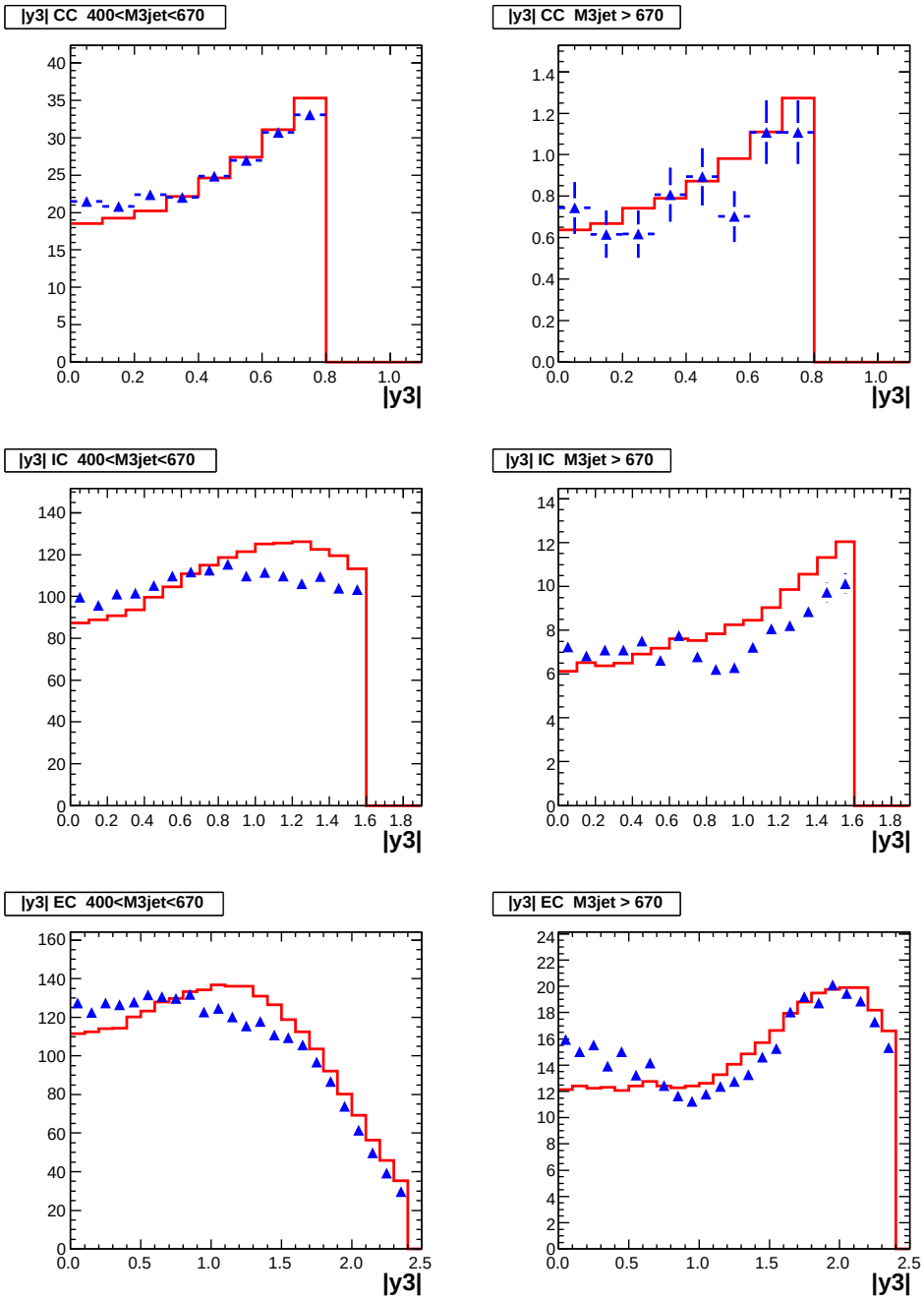

Figure A.13: Third leading jet rapidity control plot 1.

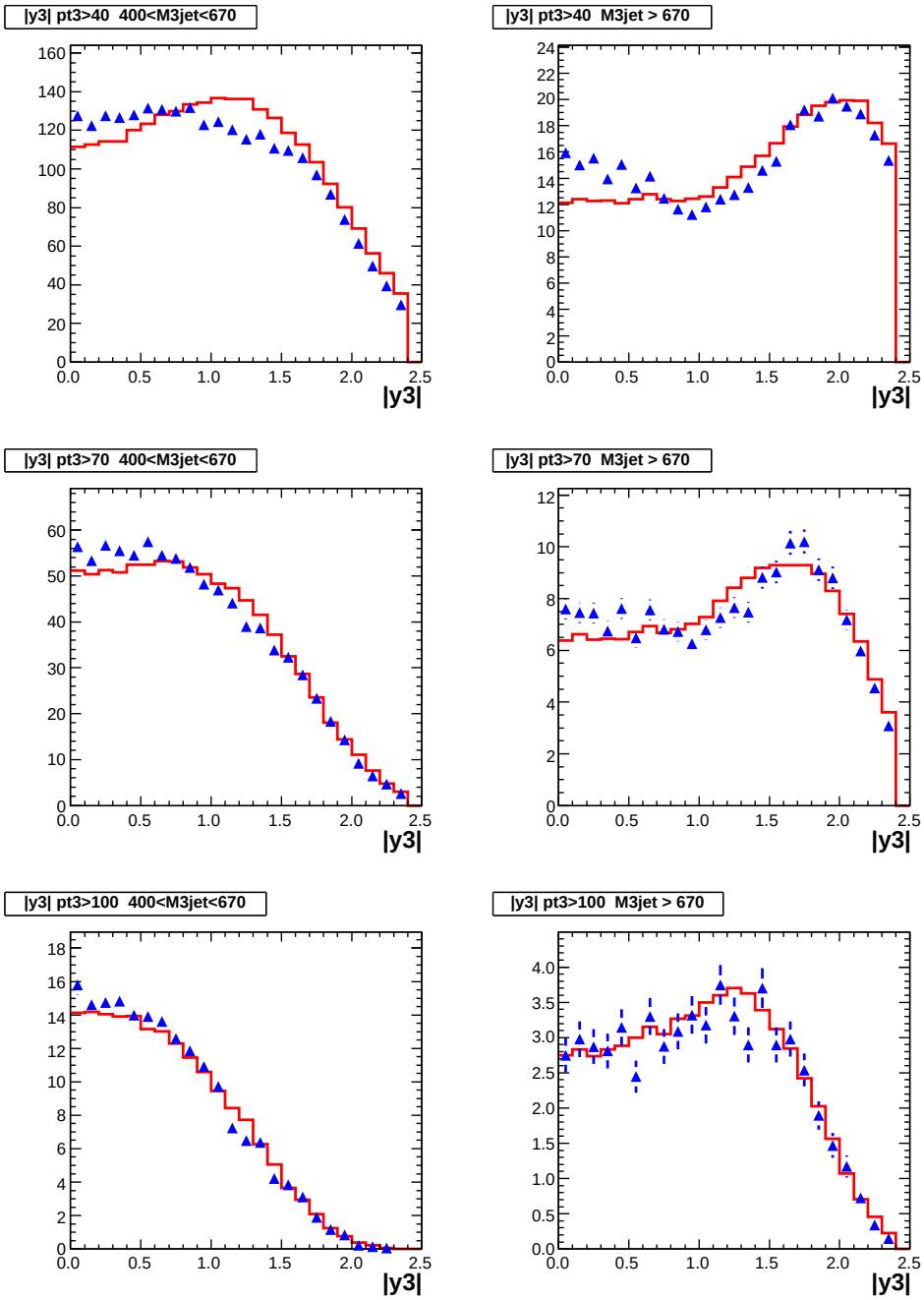

Figure A.14: Third leading jet rapidity control plot 2.

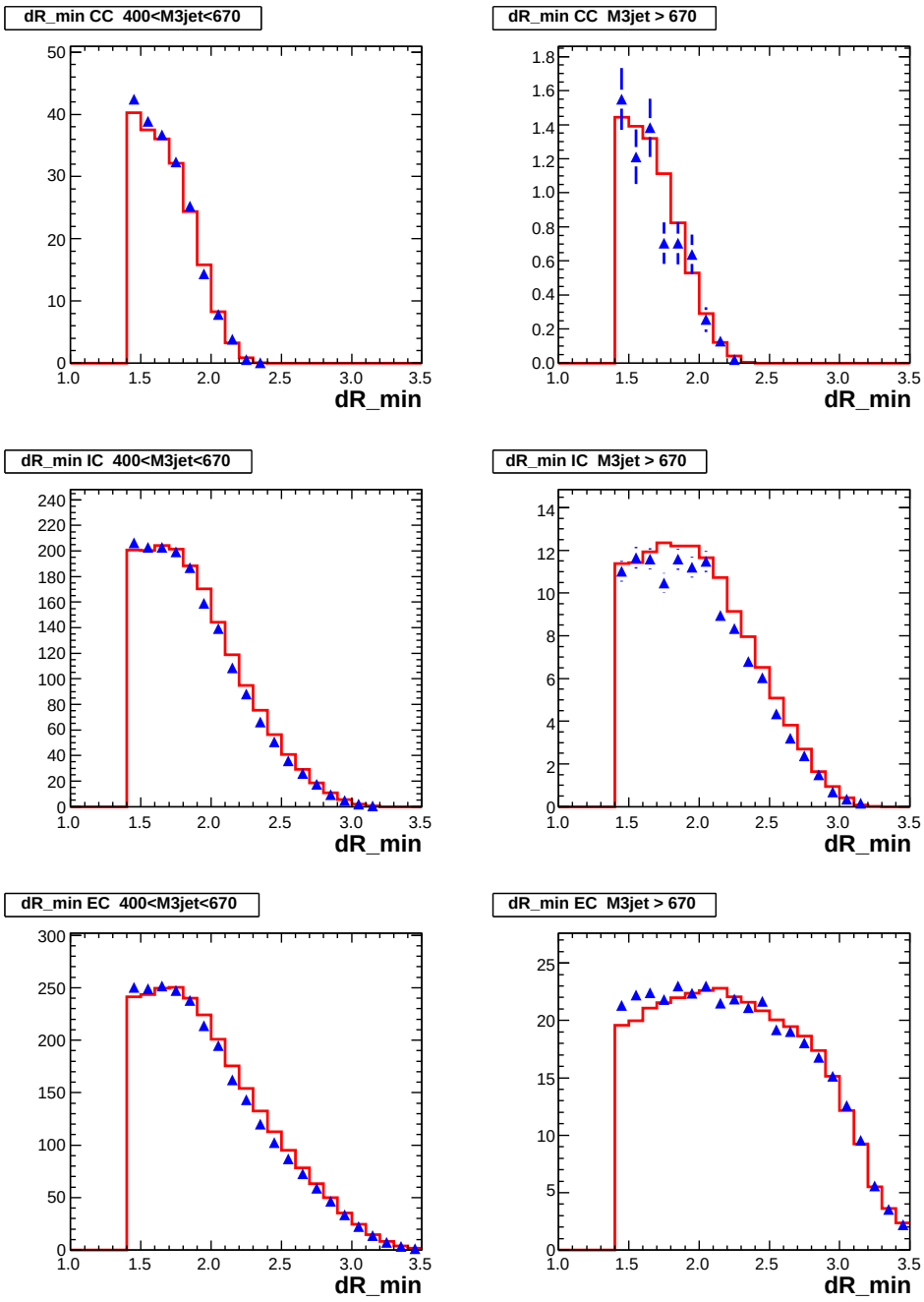

Figure A.15: Minimum distance between jets control plot 1.

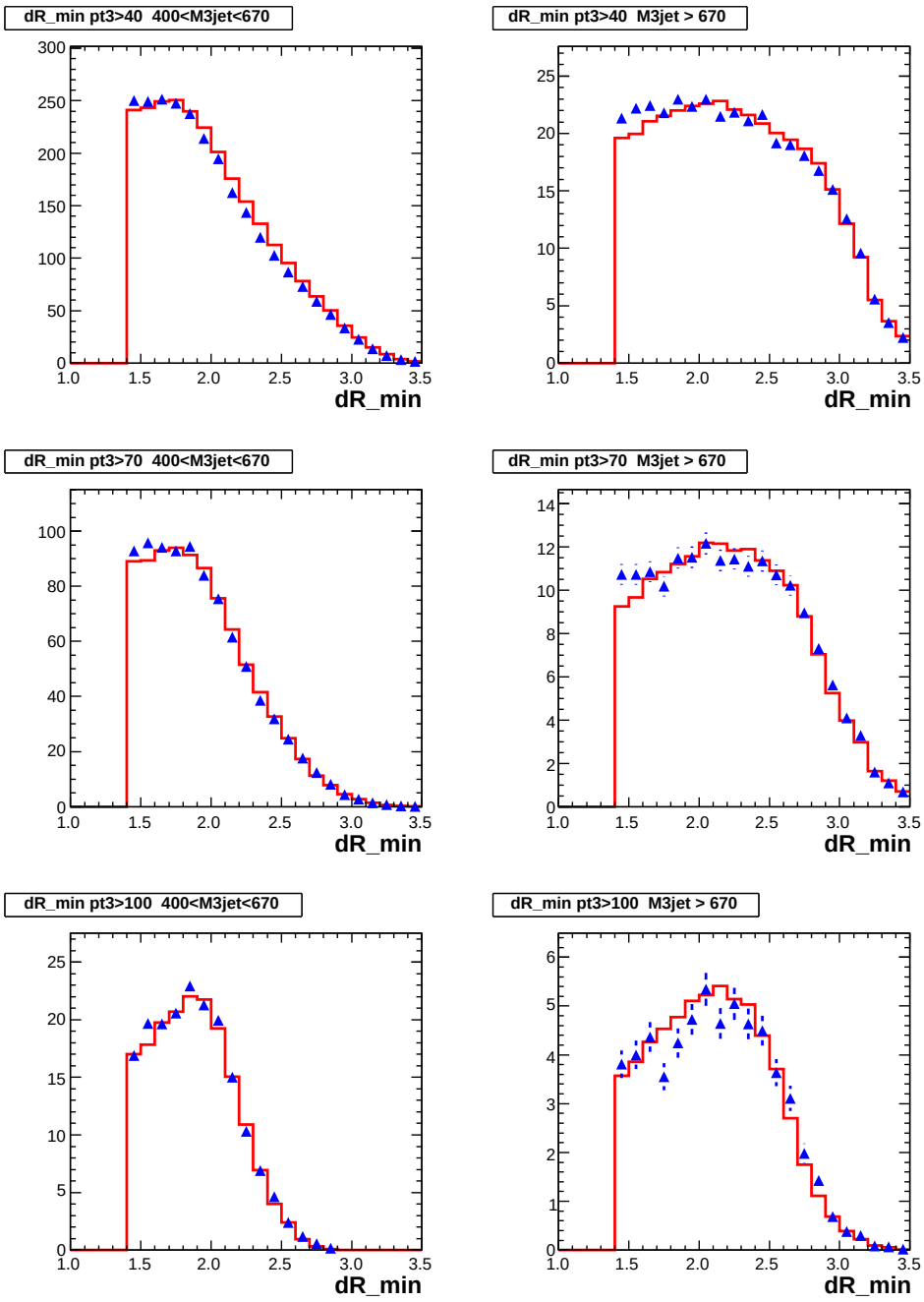

Figure A.16: Minimum distance between jets control plot 2.

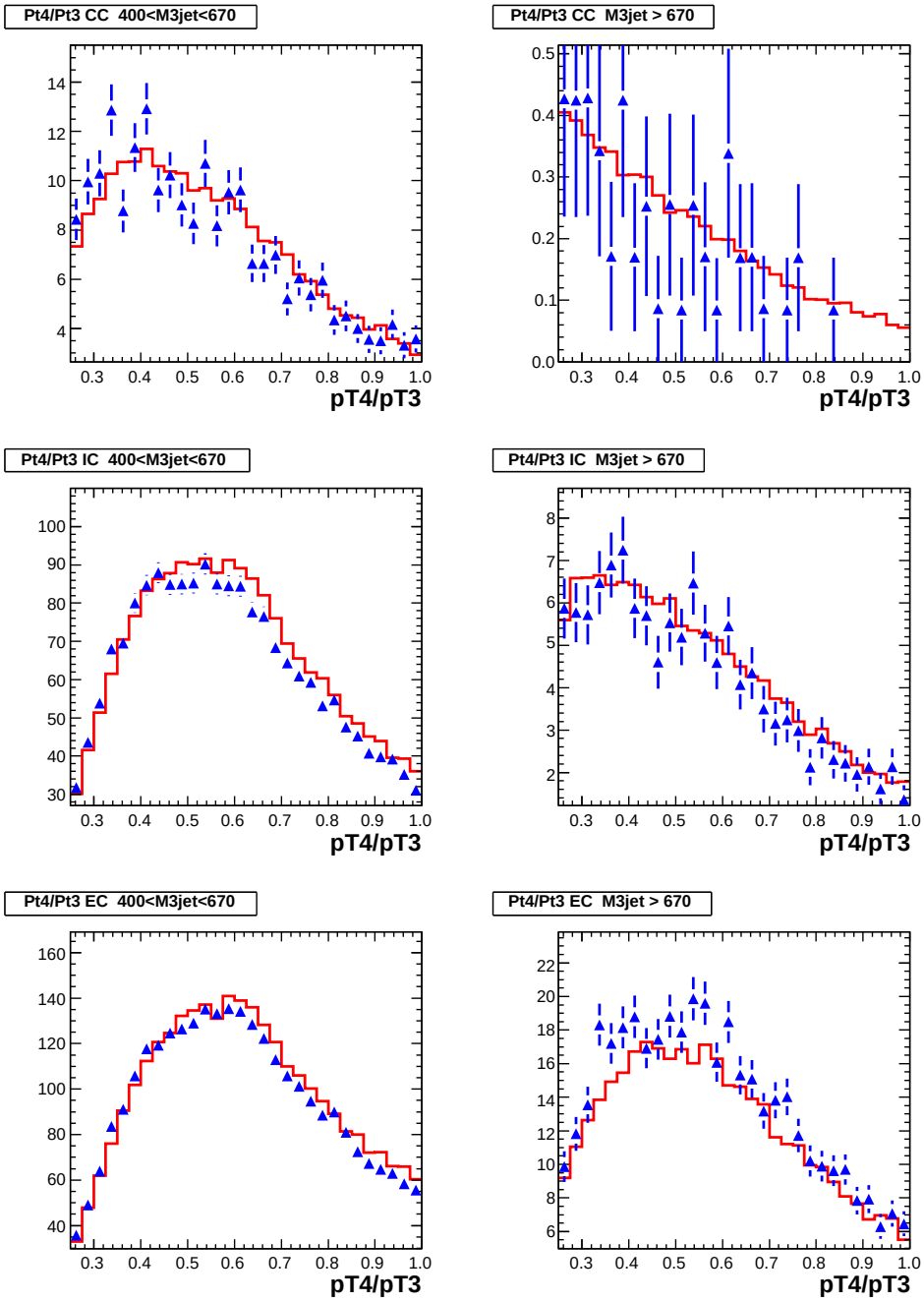

Figure A.17: Fourth jet transverse momentum divided by the third jet transverse momentum control plot 1.

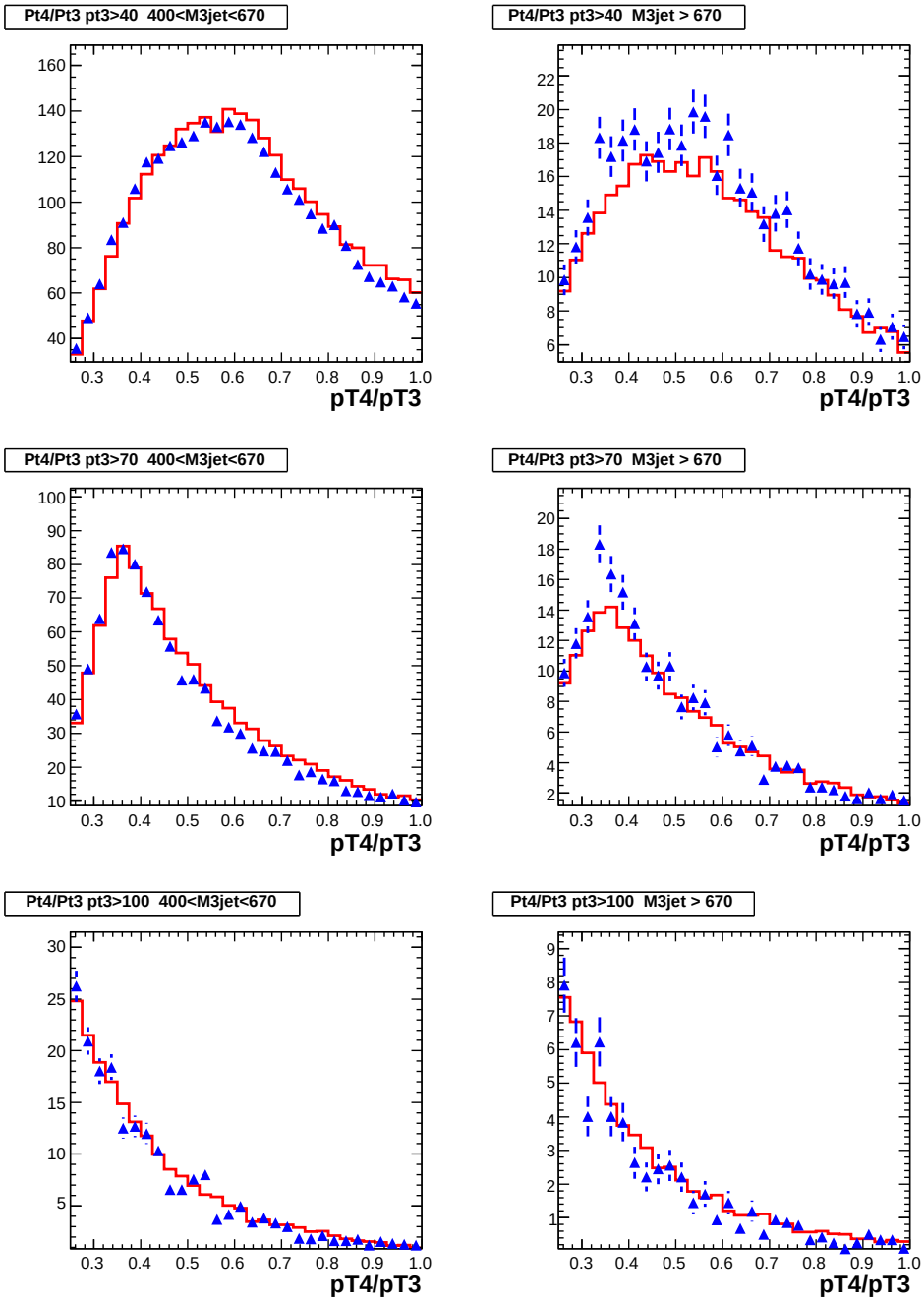

Figure A.18: Fourth jet transverse momentum divided by the third jet transverse momentum control plot 2.

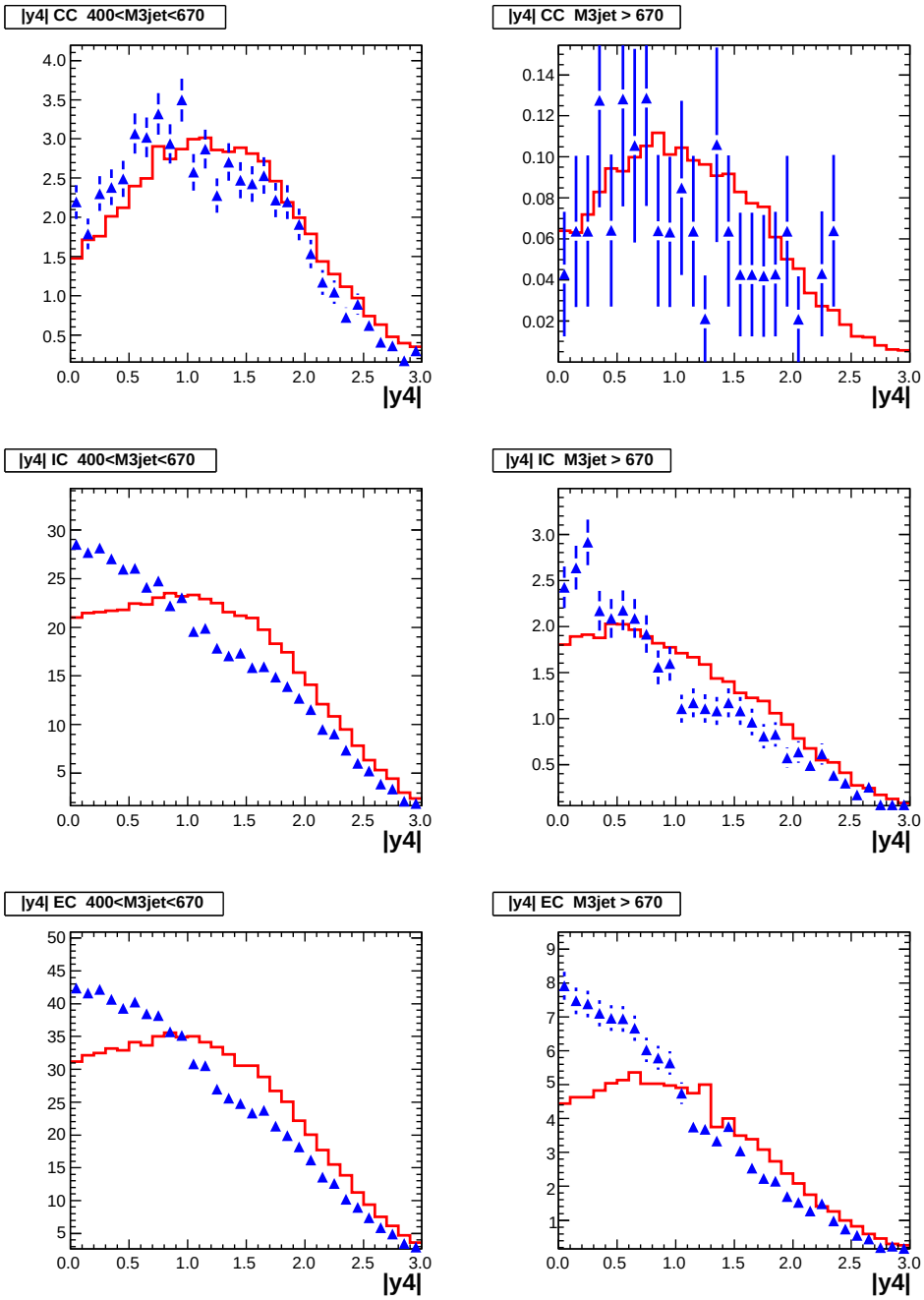

Figure A.19: Fourth jet rapidity control plot 1.

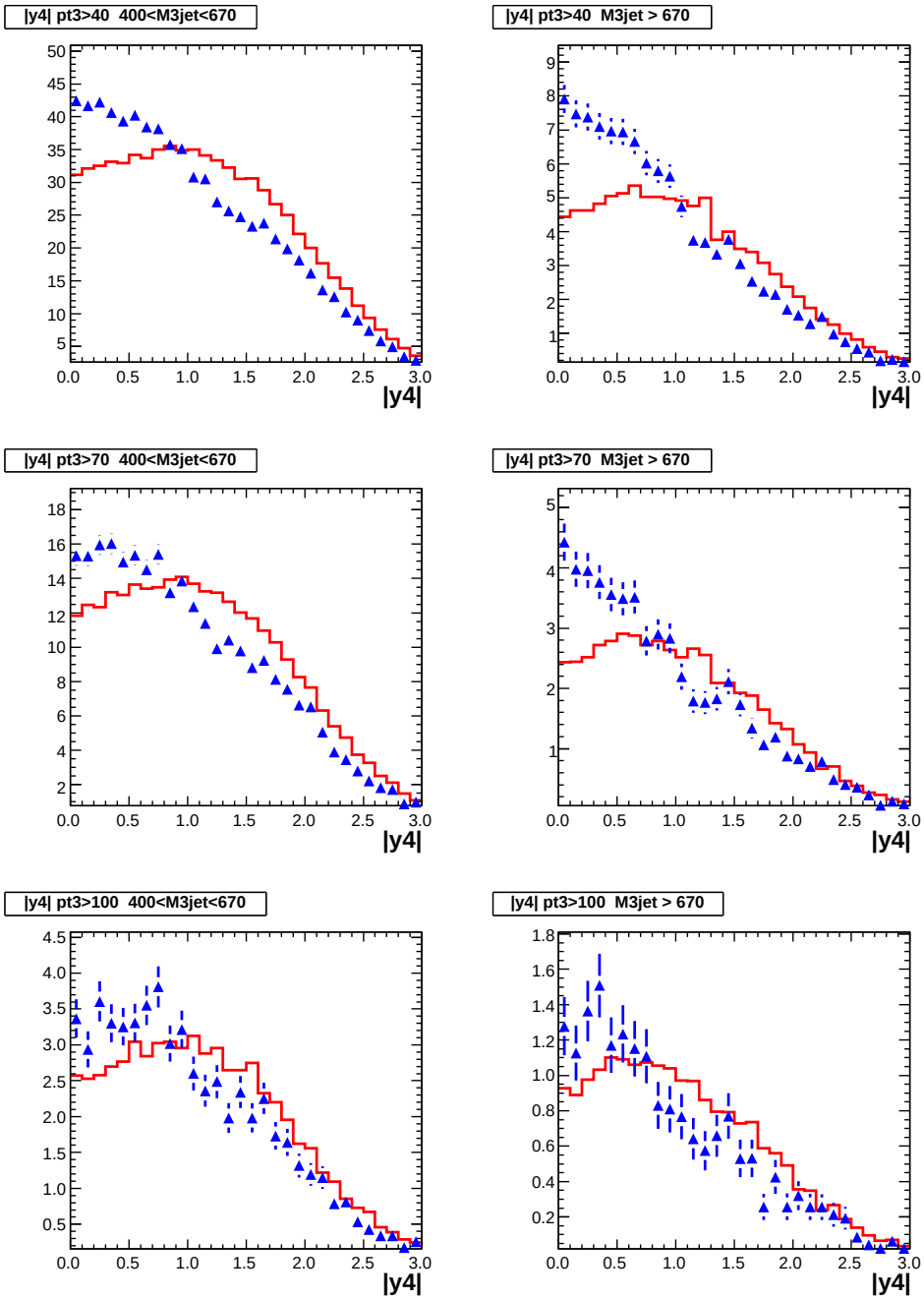

Figure A.20: Fourth jet rapidity control plot 2.

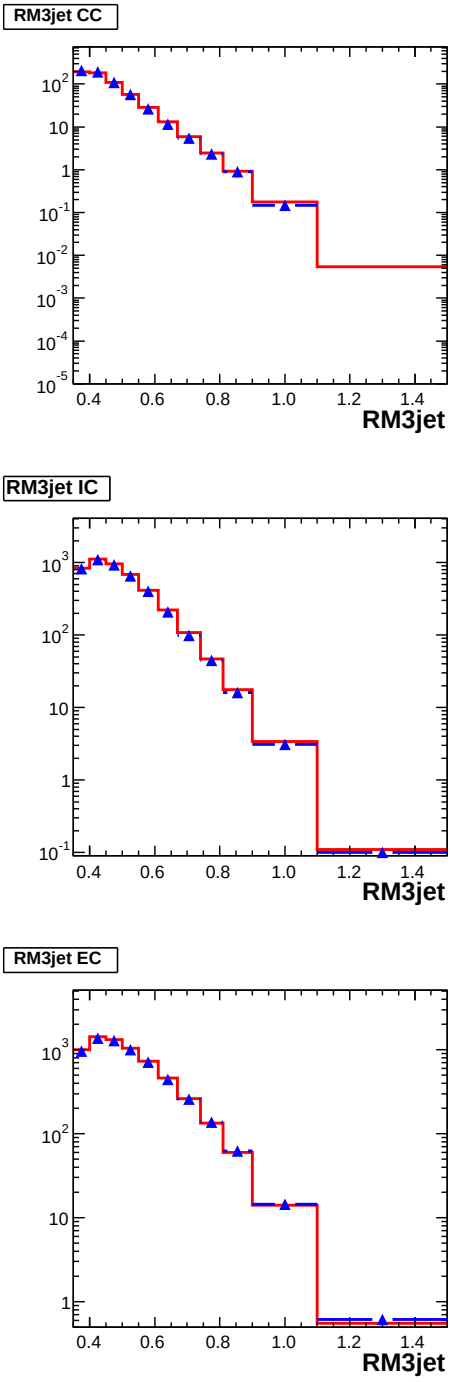

Figure A.21: Rescaled three-jet mass control plot 1.

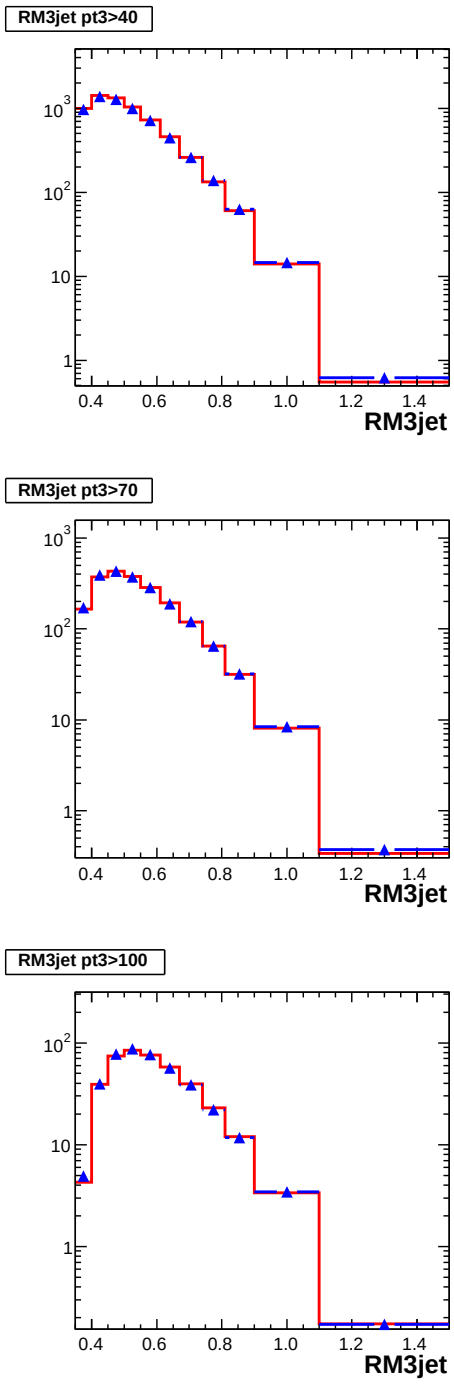

Figure A.22: Rescaled three-jet mass control plot 2.

B Cross section tables

$M_{3\text{jet}}$ (TeV)	$\langle M_{3\text{jet}} \rangle$ (TeV)	N^{entries}	Data (pb/TeV)	δ^{stat} %	δ^{sys} %	Theory (pb/TeV)	Nonpert. correction
0.40–0.45	0.423	4496	192.861	1.5	+11.0,-11.2	202.971	1.002
0.45–0.50	0.473	2587	112.120	2.0	+11.8,-10.8	118.074	1.004
0.50–0.55	0.522	1344	58.856	2.7	+12.0,-11.9	60.934	1.006
0.55–0.61	0.576	750	27.643	3.7	+11.4,-11.7	29.797	1.008
0.61–0.67	0.636	328	12.231	5.5	+12.3,-11.6	13.594	1.010
0.67–0.74	0.699	249	5.752	6.3	+12.2,-13.3	6.030	1.012
0.74–0.81	0.769	110	2.562	9.5	+14.3,-13.4	2.473	1.014
0.81–0.90	0.848	46	0.847	14.7	+14.8,-14.2	0.918	1.017
0.90–1.10	0.954	22	0.184	21.3	+17.9,-17.0	0.173	1.022

Table B.1: Three-jet mass cross section for the CC region. The number of events is for the rescaled mass. The nonperturbative correction is already included in the theory cross section.

$M_{3\text{jet}}$ (TeV)	$\langle M_{3\text{jet}} \rangle$ (TeV)	N^{entries}	Data (pb/TeV)	δ^{stat} %	δ^{sys} %	Theory (pb/TeV)	Nonpert. correction
0.40–0.45	0.425	25703	1007.112	0.6	+11.4,-12.1	1145.441	1.004
0.45–0.50	0.474	21807	873.877	0.7	+13.1,-12.3	1006.286	1.007
0.50–0.55	0.523	15360	627.885	0.8	+12.4,-12.7	722.777	1.011
0.55–0.61	0.577	11379	394.773	0.9	+14.1,-12.3	449.201	1.015
0.61–0.67	0.637	5905	208.309	1.3	+14.3,-13.7	245.979	1.019
0.67–0.74	0.700	3265	100.067	1.8	+14.5,-14.7	118.984	1.024
0.74–0.81	0.771	1465	45.370	2.6	+16.3,-15.7	52.427	1.029
0.81–0.90	0.847	677	16.417	3.8	+17.0,-15.4	19.558	1.034
0.90–1.10	0.960	293	3.184	5.8	+20.2,-20.7	3.636	1.045
1.10–1.50	1.175	24	0.087	20.4	+27.5,-26.5	0.109	1.066

Table B.2: Three-jet mass cross section for the IC region. The number of events is for the rescaled mass. The nonperturbative correction is already included in the theory cross section.

$M_{3\text{jet}}$ (TeV)	$\langle M_{3\text{jet}} \rangle$ (TeV)	N^{entries}	Data (pb/TeV)	δ^{stat} %	δ^{sys} %	Theory (pb/TeV)	Nonpert. correction
0.40–0.45	0.425	32350	1234.652	0.6	+11.9,-12.2	1384.588	0.994
0.45–0.50	0.474	30022	1165.579	0.6	+13.4,-12.3	1320.435	0.999
0.50–0.55	0.524	23435	923.455	0.7	+12.8,-12.9	1064.389	1.004
0.55–0.61	0.578	20087	668.398	0.7	+14.3,-13.1	750.344	1.009
0.61–0.67	0.638	12520	421.463	0.9	+14.7,-14.5	486.342	1.015
0.67–0.74	0.701	8523	248.016	1.1	+15.4,-15.6	285.698	1.022
0.74–0.81	0.771	4532	132.571	1.5	+17.1,-15.4	154.756	1.029
0.81–0.90	0.848	2639	60.125	1.9	+17.9,-18.8	70.591	1.037
0.90–1.10	0.963	1362	13.797	2.7	+20.5,-21.1	17.261	1.052
1.10–1.50	1.167	116	0.540	9.3	+29.4,-27.4	0.665	1.082

Table B.3: Three-jet mass cross section for the EC region. The number of events is for the rescaled mass. The nonperturbative correction is already included in the theory cross section.

$M_{3\text{jet}}$ (TeV)	$\langle M_{3\text{jet}} \rangle$ (TeV)	N^{entries}	Data (pb/TeV)	δ^{stat} %	δ^{sys} %	Theory (pb/TeV)	Nonpert. correction
0.40–0.45	0.425	32350	1234.652	0.6	+11.9,-12.2	1384.588	0.994
0.45–0.50	0.474	30022	1165.579	0.6	+13.4,-12.3	1320.435	0.999
0.50–0.55	0.524	23435	923.455	0.7	+12.8,-12.9	1064.389	1.004
0.55–0.61	0.578	20087	668.398	0.7	+14.3,-13.1	750.344	1.009
0.61–0.67	0.638	12520	421.463	0.9	+14.7,-14.5	486.342	1.015
0.67–0.74	0.701	8523	248.016	1.1	+15.4,-15.6	285.698	1.022
0.74–0.81	0.771	4532	132.571	1.5	+17.1,-15.4	154.756	1.029
0.81–0.90	0.848	2639	60.125	1.9	+17.9,-18.8	70.591	1.037
0.90–1.10	0.963	1362	13.797	2.7	+20.5,-21.1	17.261	1.052
1.10–1.50	1.167	116	0.540	9.3	+29.4,-27.4	0.665	1.082

Table B.4: Three-jet mass cross section for the 40 region. The number of events is for the rescaled mass. The nonperturbative correction is already included in the theory cross section.

$M_{3\text{jet}}$ (TeV)	$\langle M_{3\text{jet}} \rangle$ (TeV)	N^{entries}	Data (pb/TeV)	δ^{stat} %	δ^{sys} %	Theory (pb/TeV)	Nonpert. correction
0.40–0.45	0.426	9174	383.880	1.0	+12.0,-12.3	452.355	0.980
0.45–0.50	0.475	10186	429.036	1.0	+12.8,-12.5	495.498	0.987
0.50–0.55	0.524	8749	370.531	1.1	+13.0,-13.4	442.369	0.993
0.55–0.61	0.578	8090	286.644	1.1	+13.5,-13.2	328.281	1.000
0.61–0.67	0.638	5356	190.369	1.4	+14.6,-13.8	226.719	1.008
0.67–0.74	0.701	3946	120.312	1.6	+15.4,-15.3	140.874	1.017
0.74–0.81	0.772	2142	65.231	2.2	+16.6,-14.6	80.751	1.026
0.81–0.90	0.849	1351	31.845	2.7	+17.5,-19.5	39.463	1.036
0.90–1.10	0.966	793	8.267	3.6	+21.4,-20.6	10.192	1.055
1.10–1.50	1.167	70	0.340	12.0	+28.9,-24.9	0.443	1.095

Table B.5: Three-jet mass cross section for the 70 region. The number of events is for the rescaled mass. The nonperturbative correction is already included in the theory cross section.

$M_{3\text{jet}}$ (TeV)	$\langle M_{3\text{jet}} \rangle$ (TeV)	N^{entries}	Data (pb/TeV)	δ^{stat} %	δ^{sys} %	Theory (pb/TeV)	Nonpert. correction
0.40–0.45	0.429	926	37.987	3.3	+13.9,-13.5	51.891	0.972
0.45–0.50	0.476	1825	75.501	2.3	+14.8,-11.8	90.032	0.976
0.50–0.55	0.525	2048	85.334	2.2	+13.5,-13.6	98.064	0.979
0.55–0.61	0.579	2165	75.635	2.1	+12.7,-13.5	87.207	0.983
0.61–0.67	0.639	1592	55.916	2.5	+13.8,-13.0	66.659	0.987
0.67–0.74	0.701	1272	38.423	2.8	+14.8,-14.5	44.212	0.992
0.74–0.81	0.772	722	21.827	3.7	+18.8,-16.3	26.560	0.997
0.81–0.90	0.851	495	11.623	4.5	+16.4,-18.5	14.178	1.002
0.90–1.10	0.966	324	3.379	5.6	+22.2,-20.6	4.024	1.012
1.10–1.50	1.168	32	0.158	17.7	+25.3,-22.6	0.210	1.034

Table B.6: Three-jet mass cross section for the 100 region. The number of events is for the rescaled mass. The nonperturbative correction is already included in the theory cross section.

C Three-jet Event Display

Many events contain at least three jets. Not that many are visually interesting like the one presented in this Appendix. The selected event, run number 204698, event number 48041857, collected on March 13, 2005 somewhen between 10:30am and 2:30pm, contains three jets in the central region of the calorimeter ($|y| < 0.8$) in a configuration which is called "Mercedes type" due to the perfect balance of three jets in the transverse plane. The reconstructed three-jet mass of this event is almost 1 TeV.

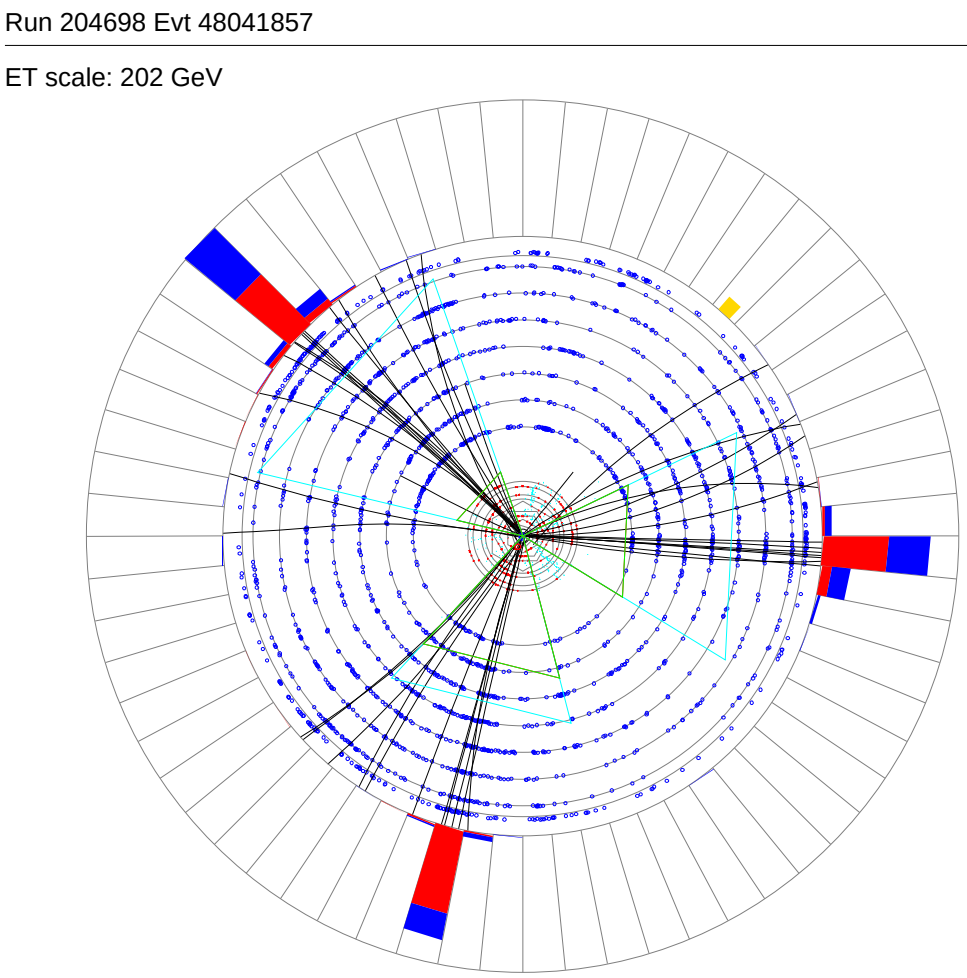

Figure C.1: Transverse (XY) view of the event 204698, 48041857. The interaction vertex is located in the center of the picture. Each hit in the silicon and scintillating fiber detector is presented with red and blue dots. Reconstructed charged particle tracks with transverse momentum above 0.5 GeV are shown in black. The outer red and blue bars represent energies deposited in the electromagnetic and hadronic layers of the calorimeter. The yellow bar represents the missing transverse energy of the event confirming the nice balance of the three jets.

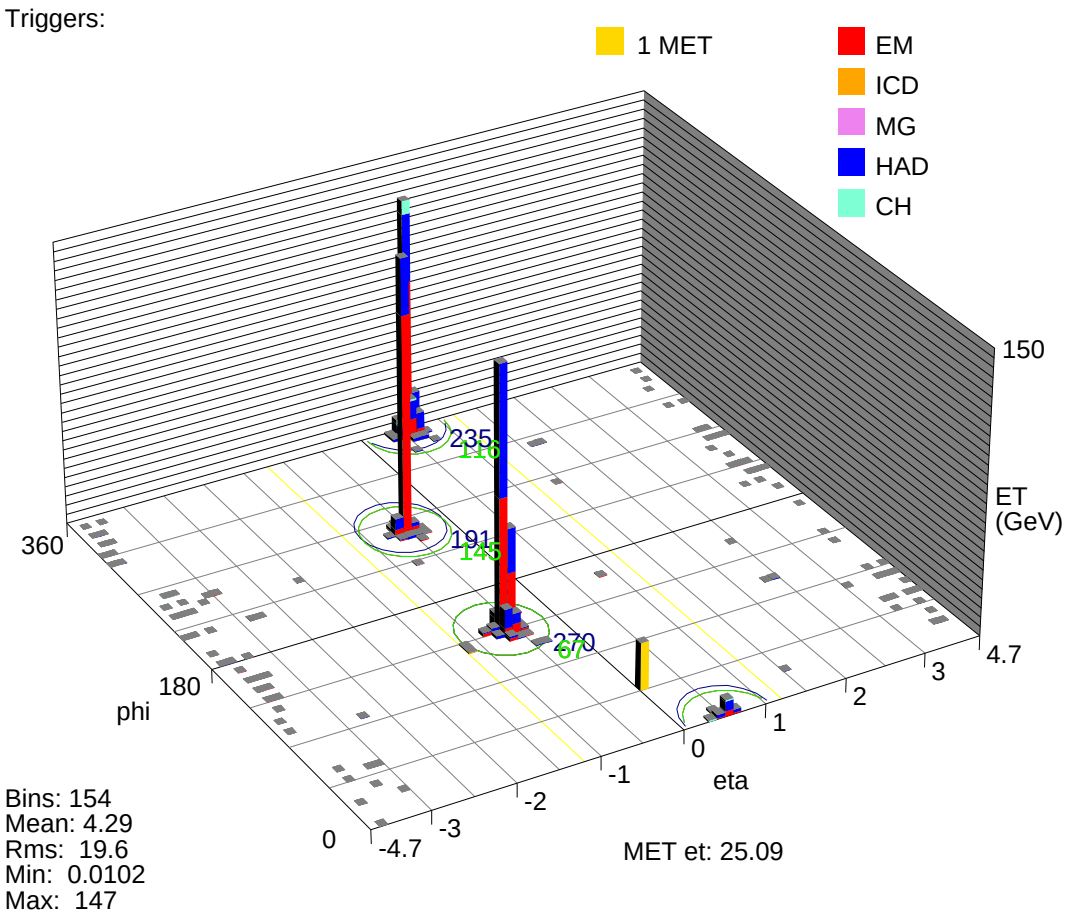

Figure C.2: The so-called lego display showing the energy depositions in individual calorimeter towers (eta and phi coordinates). Vertical axis corresponds to the transverse energy.

Bibliography

[1] J. Dalton, W. H. Wollaston, T. Thomson, *Foundations of the atomic theory: comprising papers and extracts by John Dalton, William Hyde Wollaston, M. D., and Thomas Thomson, M. D. (1802-1808)*, Edinburgh, W.F. Clay, (1893).

[2] J. J. Thomson, *Cathode Rays*, Phil. Mag., 44, 293 (1897).

[3] E. D. Bloom *et al.*, *High-Energy Inelastic e p Scattering at 6-Degrees and 10-Degress*, Phys. Rev. Lett. **23**, 930 (1969); J. I. Friedman and H. W. Kendall, *Deep inelastic electron scattering*, Ann. Rev. Nucl. Part. Sci. **22**, 203 (1972); R. P. Feynman, *Very high-energy collisions of hadrons*, Phys. Rev. Lett. **23**, 1415 (1969); J. D. Bjorken and E. A. Paschos, *Inelastic Electron Proton and gamma Proton Scattering, and the Structure of the Nucleon*, Phys. Rev. **185**, 1975 (1969).

[4] V. M. Abazov, *et al.*, *Measurement of the Inclusive Jet Cross Section in $p\bar{p}$ Collisions at $\sqrt{s} = 1.96$ TeV*, Phys. Rev. Lett. 101, 062001 (2008).

[5] V. M. Abazov, *et al.*, *Measurement of the Dijet Invariant Mass Cross Section in $p\bar{p}$ Collisions at $\sqrt{s} = 1.96$ TeV*, Submitted to Phys. Lett. B, arXiv.org:1002.4594 (2010).

[6] V. M. Abazov, *et al.*, *Measurement of Dijet Angular Distributions at $\sqrt{s} = 1.96$ TeV and Searches for Quark Compositeness and Extra Spatial Dimensions*, Phys. Rev. Lett. 103, 191803 (2009).

[7] V. M. Abazov, *et al.*, *Measurement of Dijet Azimuthal Decorrelations at Central Rapidities in $p\bar{p}$ Collisions at $\sqrt{s} = 1.96$ TeV*, Phys. Rev. Lett. 94, 221801 (2005).

[8] R. Brandelik, *et. al.* (TASSO Collaboration), *Evidence for Planar Events in e+ e- Annihilation at High-Energies*, Phys. Lett. B86, 243 (1979).

[9] D. P. Barber, *et. al.* (MARK-J Collaboration), *Discovery of Three-Jet Events and a Test of Quantum Chromodynamics at PETRA*, Phys. Rev. Lett. 43, 830 (1979); W. Bartel, *et. al.* (JADE Collaboration), *Differential Three Jet Cross-section in e^+e^- Annihilation and Comparison with Second Order Predictions of QCD and Abelian Vector Theory*, Phys. Lett. B119, 239 (1982); R. Brandelik, *et. al.* (TASSO Collaboration), *Evidence for a Spin One Gluon in Three Jet Events*, Phys. Lett. B97, 453 (1980).

[10] G. Alexander, *et. al.* (OPAL Collaboration), *Measurement of Three-Jet Distributions Sensitive to the Gluon Spin in e^+e^- Annihilations at $\sqrt{s} = 91\,\mathrm{GeV}$*, Z. Phys. C62, 643 (1991); D. Buskulic, *et. al.* (ALEPH Collaboration), *Quark and Gluon Jet Properties in Symmetric Three-Jet Events*, Phys. Lett. B384, 353 (1996); P. Abreu, *et. al.* (DELPHI Collaboration), *Energy Dependence of the Differences between the Quark and Gluon Jet Fragmentation*, Z. Phys, C70, 179 (1996); B. Adeva, *et. al.* (L3 Collaboration), *A Test of QCD based on 3-Jet Events from Z^0 Decays*, Phys. Lett. B263, 551 (1991).

[11] G. Arnison, *et. al.* (UA1 Collaboration), *Comparison of Three Jet and Two Jet Cross-Sections in p anti-p Collisions at the CERN SPS p anti-p Collider.*, Phys. Lett. B158, 494 (1985).

[12] J. A. Appel, *et. al.* (UA2 Collaboration), *A Study of Three Jet Events at the CERN anti-p p Collider.*, Z. Phys. C30, 341 (1986).

[13] A. L. S. Angelis, *et. al.* (CMOR Collaboration), *Three Jet Events At The CERN Intersecting Storage Rings*, Nucl. Phys. B303, 569 (1988).

[14] S. Abachi, *et. al.* (DØ Collaboration), *Studies of topological distributions of inclusive three- and four-jet events in $\bar{p}p$ collisions at $\sqrt{s} = 1800\,\mathrm{GeV}$ with the D0 detector*, Phys. Rev. D53, 6000 (1996).

[15] F. Abe, *et. al.* (CDF Colaboration), *The topology of Three Jet Events in anti-p p Collisions at sqrts = 1.8 TeV.*, Phys. Rev. D45, 1448 (1992); F. Abe, *et. al.* (CDF Collaboration), *Properties of High-Mass Multijet Events at the Fermilab Proton-Antiproton Collider.*, Phys. Rev. Lett. 75, 608 (1995).

[16] D. E. Acosta, *et. al.* (CDF Collaboration), *Comparison of Three-jet Events in $p\bar{p}$ Collisions at $\sqrt{s} = 1.8\,\mathrm{TeV}$ to Predictions from a Next-to-leading Order QCD Calculation*, Phys. Rev. D71, 032002 (2005).

[17] Z. Hubacek, *Properties of DØ Run II Cone Algorithm*, presentation at TeV4LHC Workshop at CERN, April 2005.

[18] TeV4LHC QCD Working Group, *Tevatron-for-LHC Report of the QCD Working Group*, hep-ph/0610012, Fermilab-Conf-06-359.

[19] V. M. Abazov, *et al.* (DØ Collaboration), *The Upgraded D0 Detector*, Nucl. Instr. and Methods A565, 463 (2006).

[20] *Digging down to the top (quark)*, Fermilab Today, Sep 28, 2006 http://www.fnal.gov/pub/today/archive_2006/today06-09-28.html.

[21] *The proton's parton patrol*, Fermilab Today, Jan 24, 2008 http://www.fnal.gov/pub/today/archive_2008/today08-01-24.html.

[22] JES Group, *Jet Energy Scale Determination at DØ Run II (final p17 version)*, DØ Note 5382, Version 1.4 (2007).

[23] J. Hegeman, *Showering analysis for final p17 jet energy scale*, DØ Note 5383, Version 1.2 (2007).

[24] M. Voutilainen, JES Group, *Jet Four-vector Scale Determination for Dijets in DØ Run IIa (final p17 version)*, DØ Note 5550 (2008).

[25] *DZero Preliminary Jet Energy Scale*, http://www-d0.fnal.gov/phys_id/jes/public/plots_v7.1/, 2006.

[26] *DZero Final Run IIa Jet Energy Scale*, http://www-d0.fnal.gov/phys_id/jes/public_RunIIa/, 2008.

[27] M. Gell-Mann, *A Schematic Model of Baryons and Mesons*, Phys. Lett. 8, 214, 1964; G. Zweig, *An SU(3) model for strong interaction symmetry and its breaking*, CERN preprint 8419/TH.412.

[28] D. J. Gross, F. Wilczek, *Ultraviolet Behavior of Nonabelian Gauge Theories*, Phys. Rev. Lett. 30, 1343 (1973); H. D. Politzer, *Reliable Perturbative Results for Strong Interactions?*, Phys. Rev. Lett. 30, 1346 (1973).

[29] C. Amsler, *et. al.* (Particle Data Group), *The Review of Particle Physics*, Phys. Lett. B667, 1 (2008).

[30] T. Sjöstrand, S. Mrenna, P. Skands, *PYTHIA 6.4 Physics and Manual*, JHEP05 026 (2006).

[31] G. Corcella, I. G. Knowles, G. Marchesini, S. Moretti, K. Odagiri, P. Richardson, M. H. Seymour, B. R. Webber, *HERWIG 6: an event generator for Hadron Emission Reactions With Interfering Gluons (including supersymmetric processes)*, JHEP 0101 010 (2001), hep-ph/0011363.

[32] M. L. Mangano, M. Moretti, F. Piccinini, R. Pittau, A. Polosa, *ALPGEN, a generator for hard multiparton processes in hadronic collisions*, JHEP 0307:001 (2003), hep-ph/0206293.

[33] T. Gleisberg, S. Hoeche, F. Krauss, M. Schoenherr, S. Schumann, F. Siegert, J. Winter, *Event generation with SHERPA 1.1*, JHEP02 (2009) 007.

[34] R. Brun, F. Carminati, CERN Program Library Long Writeup W5013 (unpublished, 1993).

[35] Z. Nagy, *Three jet cross-sections in hadron hadron collisions at next-to-leading order*, Phys. Rev. Lett. 88, 122003 (2002); Z. Nagy, *Next-to-leading order calculation of three jet observables in hadron hadron collision*, Phys. Rev. D68, 094002 (2003); ; Z. Nagy,http://www.desy.de/~znagy/Site/NLOJet++.html.

[36] Z. Kunszt, D. E. Soper, *Calculation of jet cross sections in hadron collisions at order* α_s^3, Phys. Rev. D46, 192 (1992). T. O. Eynck, E. Laenen, L. Phaf, S. Weinzierl, *Comparison of phase space slicing and dipole subtraction methods for* $\gamma^\star \to QQ$, Eur. Phys. J. C23, 259 (2002).

[37] S. Catani, M. H. Seymour, *A General Algorithm for Calculating Jet Cross Sections in NLO QCD*, Nucl. Phys. B485, 291 (1997), Erratum-ibid.B510, 503 (1998), hep-ph/9605323.

[38] A. Kupco, *Measurement and QCD analysis of inclusive dijet mass cross section in* $p\bar{p}$ *collisions at* $\sqrt{s} = 1.96\,\mathrm{TeV}$, Doctoral Thesis, Charles University, 2003.

[39] G. Hanson, *et. al.*, *Evidence for Jet Structure in Hadron Production by e+ e- Annihilation.*, Phys. Rev. Lett 35, 1609 (1975).

[40] G. Blazey, *et al.*, *Run II Jet Physics: Proceedings of the Run II QCD and Weak Boson Physics Workshop*, hep-ex/0005012, FERMILAB-CONF-00-092-E (2000).

[41] V. M. Abazov, *et. al.* (DØ Collaboration), *Subjet multiplicity of gluon and quark jets reconstructed with the $k_\perp$ algorithm in $p\bar{p}$ collisions*, Phys. Rev D 65, 052008 (2002).

[42] A. Abulencia, *et. al.* (CDF Collaboration), *Measurement of the Inclusive Jet Cross Section Using the k_{T} Algorithm in $p\bar{p}$ Collisions at $\sqrt{s} = 1.96\,\mathrm{TeV}$*, Phys. Rev. Lett. 96, 122001 (2006).

[43] S. D. Ellis, D. E. Soper, *Successive combination jet algorithm for hadron collisions*, Phys. Rev. D 48, 3160 - 3166 (1993).

[44] G. Sterman, S. Weinberg, *Jets from Quantum Chromodynamics*, Phys. Rev. Lett. 39, 1436 (1977).

[45] E. Busato, B. Andrieu, *Jet Algorithms in the DØ Run II Software: Description and User's Guide*, DØ Note 4457 (2004).

[46] G. P. Salam, G. Soyez, *A practical Seedless Infrared-Safe Cone jet algorithm*, JHEP 05, 086 (2007).

[47] M. Cacciari, G. P. Salam, *Dispelling the N**3 myth for the k(t) jet-finder*, Phys. Lett. B641, 57 (2006), hep-ph/0512210.

[48] Yu. L. Dokshitzer, G. D. Leder, S. Moretti, B. R. Webber, *Better Jet Clustering Algorithms*, JHEP9708 001 (1997), hep-ph/9707323v2.

[49] M. Cacciari, G. P. Salam and G. Soyez, *The anti-kt jet clustering algorithm*, JHEP 0804 063 (2008), arXiv:0802.1189 hep-ph.

[50] J. Huth *et al.*, in Proceedings of *Research Directions for the Decade, Snowmass 1990*, Editor E. L. Berger, (World Scientific, Singapore, 1992).

[51] S. Catani, Yu. L. Dokshitzer, M. H. Seymour, B. R. Webber, *Longitudinally-Invariant $k_\perp$-Clustering Algorithms for Hadron-Hadron Collisions*, Nucl. Phys. B406, 187 (1993).

[52] W. B. Kilgore, W. T. Giele, *Next-to-leading order gluonic three-jet production at hadron colliders*, Phys. Rev. D 55, 7183 (1997).

[53] C. Amsler, *et al.* (Particle Data Group), *2008 Review of Particle Physics*, Phys. Lett. B667, 1 (2008).

[54] T. Andeen, *et. al.*, *The DØ Experiment's Integrated Luminosity for Tevatron Run IIa*, DØ Note 5398 (2007).

[55] R. Brun, F. Rademakers, *ROOT - An Object Oriented Data Analysis Framework*, Proceedings AIHENP'96 Workshop, Lausanne, Nucl. Inst. and Meth. in Phys. Res. A 389 (1997) 81-86. http://root.cern.ch/ (1997).

[56] F. Borcherding, S. Grünendahl, *DØ Central Fiber Tracker CFT Description Page*, http://d0server1.fnal.gov/projects/SciFi/cft_description.html, 2005 (accessed Mar 24, 2009).

[57] S. Snyder, *Measurement of the Top Quark Mass at DØ* , PhD. Thesis, 1995, http://www-d0.fnal.gov/results/publications_talks/thesis/snyder/thesis.html, (accessed Apr 20, 2007).

[58] E. Malamud, http://www-bd.fnal.gov/public/chain.html, (accessed Apr 11, 2007).

[59] E. Malamud, http://www-bd.fnal.gov/public/synchrotrons.html, (accessed Apr 12, 2007).

[60] *Software and Documentations: Computing and Core Software: D0*,

http://www-d0.fnal.gov/computing/documentation.html (accessed Jul 11, 2008).

[61] U. Bassler, G. Bernardi, *Towards a Coherent Treatment of Calorimetric Energies: Missing Transverse Energy, Jets, E. M. Objects and the T42 Algorithm*, DØ Note 4124 (2003); J.-R. Vlimant, U. Bassler, G. Bernardi, S. Trincaz-Duvoid, *Technical description of the T42 algorithm for the calorimeter noise suppression*, DØ Note 4146 (2003); G. Bernardi, E. Busato, J.-R. Vlimant, *Improvements from the T42 Algorithm on Calorimeter Objects Reconstruction*, DØ Note 4335 (2004).

[62] S. Geer, T. Asakawa, *Analysis of multijet events produced at high energy hadron colliders*, Phys. Rev. D 53, 4793 (1996).

[63] Z. Hubacek, M. Wobisch, *Measurement of the Three-jet Cross Section at DØ* , DØ Note 6013 (2010).

[64] M. Voutilainen, A. Kupco, Ch. Royon, *Measurement of inclusive jet p_T spectra in $p\bar{p}$ collision at $\sqrt{s} = 1.96\,\text{TeV}$*, DØ Note 5551 (2008).

[65] M. Voutilainen, *Jet trigger efficiencies for Run IIa*, DØ Note 5549 (2008).

[66] H. Schellman, *The longitudinal shape of the luminous region at DØ* , DØ Note 5142 (2006).

[67] M. Voutilainen, *Measurement of the Inclusive Jet Cross Section in $p\bar{p}$ Collisions at $\sqrt{s}$ = 1.96 TeV*, PhD. Thesis, Helsinki University of Technology, 2008.

[68] A. Harel, H. Nogima, M. Rangel, M. Voutilainen, *Combined JetID efficiency for p17*, DØ Note 5218 (2006).

[69] M. Wobisch, et al., *D0JetSim - A Parameterized Detector Simulation for Jet Physics*, DØ Note 5703.

[70] N. Parua, M. Wobisch, *First Measurement of Dijet Angular Distributions in the TeV Regime*, DØ Note5616.

[71] M. Rominsky, M. Strauss, M. Wobisch, D. Lincoln, *Measurement of the Double Differential Dijet Mass Spectrum at the DØ Experiment*, DØ Note 5701.

[72] Z. Hubacek, *Threejet update*, QCD Jets Internal Meeting, July 1, 2008.

[73] M. Voutilainen, *Jet p_T resolution for Run IIa final JES (v7.2) with dijet J4S jet corrections*, DØ Note 5499 (2008).

[74] M. Rominsky, *Jet p_T resolution for Run IIa as a Function of η_{det} with Final J4S (v07-02-64)*, DØ Note 5908 (2009).

[75] Z. Hubacek, *Jet η and ϕ resolutions in p17 QCD MC sample*, DØ Internal Document (2009).

[76] A. D. Martin, W. J. Stirling, R. S. Thorne, G. Watt, *Parton Distributions for the LHC*, arXiv:0901.0002, 2009.

[77] P. M. Nadolsky, H.-L. Lai, Q. -H. Cao, J. Huston, J. Pumplin, D. Stump, W. -K. Tung, C. -P. Yuan, *Implications of CTEQ global analysis for collider observables*, Phys.Rev.D78:013004, 2008.

[78] D. Lodge, *Thinks!*, Penguin, 2002.